

# Thermo-mechanical and anisotropic response of polymers in contact

**Citation for published version (APA):**

Kershah, T. G. M. (2020). *Thermo-mechanical and anisotropic response of polymers in contact*. [Phd Thesis 1 (Research TU/e / Graduation TU/e), Mechanical Engineering]. Technische Universiteit Eindhoven.

**Document status and date:**

Published: 09/06/2020

**Document Version:**

Publisher's PDF, also known as Version of Record (includes final page, issue and volume numbers)

**Please check the document version of this publication:**

- A submitted manuscript is the version of the article upon submission and before peer-review. There can be important differences between the submitted version and the official published version of record. People interested in the research are advised to contact the author for the final version of the publication, or visit the DOI to the publisher's website.
- The final author version and the galley proof are versions of the publication after peer review.
- The final published version features the final layout of the paper including the volume, issue and page numbers.

[Link to publication](#)

**General rights**

Copyright and moral rights for the publications made accessible in the public portal are retained by the authors and/or other copyright owners and it is a condition of accessing publications that users recognise and abide by the legal requirements associated with these rights.

- Users may download and print one copy of any publication from the public portal for the purpose of private study or research.
- You may not further distribute the material or use it for any profit-making activity or commercial gain
- You may freely distribute the URL identifying the publication in the public portal.

If the publication is distributed under the terms of Article 25fa of the Dutch Copyright Act, indicated by the "Taverne" license above, please follow below link for the End User Agreement:

[www.tue.nl/taverne](http://www.tue.nl/taverne)

**Take down policy**

If you believe that this document breaches copyright please contact us at:

[openaccess@tue.nl](mailto:openaccess@tue.nl)

providing details and we will investigate your claim.

# Thermo-mechanical and anisotropic response of polymers in contact

Tarek Kershah



Thermo-mechanical and anisotropic response of polymers in contact  
by Tarek Kershah  
Technische Universiteit Eindhoven, 2020.

This thesis was prepared with L<sup>A</sup>T<sub>E</sub>X documentation system.  
Cover design: Ilse Modder | [www.ilsemodder.nl](http://www.ilsemodder.nl)  
Printed by: Gildeprint BV, Enschede, The Netherlands

A catalogue record is available from the Eindhoven University of Technology Library  
ISBN: 978-90-386-5042-5

©2020 by Tarek Kershah. All rights reserved.

This research forms part of the research programme of the Dutch Polymer Institute (DPI),  
project 783t.

# Thermo-mechanical and anisotropic response of polymers in contact

PROEFSCHRIFT

ter verkrijging van de graad van doctor aan de Technische Universiteit  
Eindhoven, op gezag van de rector magnificus, prof.dr.ir. F.P.T. Baaijens,  
voor een commissie aangewezen door het College voor Promoties, in het  
openbaar te verdedigen op woensdag 9 juni 2020 om 13:30 uur

door

Tarek Gaber Mohamed Kershah

geboren te Darmstadt, Duitsland

Dit proefschrift is goedgekeurd door de promotoren en de samenstelling van de promotiecommissie is als volgt:

voorzitter: prof.dr. L.P.H. de Goey  
1<sup>e</sup> promotor: prof.dr.ir. P.D. Anderson  
co-promotor: dr.ir. L.C.A van Breemen  
leden: prof.dr. T.J. Dingemans (University of North Carolina)  
prof.dr. H. Jiang (Southwest Jiaotong University)  
prof.dr.ir. R. Akkerman (Universiteit Twente)  
prof.dr.ir. A.S.J. Suiker  
dr.ir. J.A.W. van Dommelen

*Het onderzoek of ontwerp dat in dit proefschrift wordt beschreven is uitgevoerd in overeenstemming met de TU/e Gedragscode Wetenschapsbeoefening.*

# Contents

<b>Summary</b>	<b>ix</b>
<b>1 Introduction</b>	<b>1</b>
1.1 Motivation . . . . .	1
1.2 Tribology on different scales . . . . .	2
1.3 Single-asperity scratch test . . . . .	3
1.4 Scope of the thesis . . . . .	3
1.5 Outline of the thesis . . . . .	4
<b>2 Temperature dependent two-body abrasive wear of polycarbonate surfaces</b>	<b>5</b>
2.1 Introduction . . . . .	6
2.2 Experimental . . . . .	8
2.2.1 Materials and sample preparation . . . . .	8
2.2.2 Testing . . . . .	8
2.3 Modelling . . . . .	9
2.3.1 Constitutive model . . . . .	9
2.3.2 Intrinsic response and model parameters . . . . .	10
2.3.3 Finite element mesh and friction modelling . . . . .	11
2.4 Results and Discussion . . . . .	15
2.4.1 Scratch and frictional response . . . . .	15
2.4.2 Friction coefficient . . . . .	16
2.4.3 Crack formation . . . . .	18
2.5 Conclusions . . . . .	24

<b>3</b>	<b>Thermo-mechanically coupled modelling of a single-asperity scratch on an isotropic isotactic polypropylene surface</b>	<b>27</b>
3.1	Introduction . . . . .	29
3.2	Experimental . . . . .	31
3.2.1	Materials and sample preparation . . . . .	31
3.2.2	Sliding friction experiments . . . . .	31
3.3	Constitutive Modelling . . . . .	31
3.3.1	The EGP model for thermo-rheologically simple polymers . . . . .	31
3.3.2	Extension to thermo-rheologically complex behaviour . . . . .	33
3.3.3	Extension to thermo-mechanically coupled model . . . . .	34
3.3.4	Friction modelling and FEM mesh . . . . .	35
3.3.5	Intrinsic response and model parameters . . . . .	36
3.4	Results and Discussion . . . . .	40
3.4.1	Influence of the thermo-mechanical model . . . . .	40
3.4.2	Effect of friction on heat generation . . . . .	42
3.4.3	Analysis of heat generation at various scratch velocities . . . . .	44
3.4.4	Scratch and frictional response of $\alpha$ -iPP and $\beta$ -iPP . . . . .	46
3.4.5	Damage formation . . . . .	48
3.5	Conclusions . . . . .	54
<b>4</b>	<b>Uniaxial and biaxial response of anisotropic polypropylene</b>	<b>57</b>
4.1	Introduction . . . . .	58
4.2	Materials and Methods . . . . .	59
4.3	Constitutive Modelling . . . . .	60
4.3.1	Kinematics . . . . .	60
4.3.2	Stress calculation . . . . .	60
4.3.3	Extension to thermo-rheologically complex behaviour . . . . .	61
4.3.4	Hill's yield function . . . . .	61
4.3.5	Viscoplastic flow . . . . .	63
4.3.6	Implementation . . . . .	64
4.4	Simulations and model characterization . . . . .	65

---

4.4.1	Uniaxial loading . . . . .	65
4.4.2	Biaxial loading . . . . .	69
4.5	Results and Discussion . . . . .	69
4.5.1	Uniaxial tension and simple shear . . . . .	69
4.5.2	Biaxial simulations . . . . .	73
4.6	Conclusions . . . . .	76
<b>5</b>	<b>Finite element modelling of a single-asperity scratch on an anisotropic polypropylene surface</b>	<b>77</b>
5.1	Introduction . . . . .	79
5.2	Constitutive Modelling . . . . .	80
5.2.1	Stress calculation . . . . .	80
5.2.2	Extension to thermo-rheologically complex behaviour . . . . .	82
5.2.3	Extension to thermo-mechanically coupled model . . . . .	83
5.2.4	Extension to an anisotropic yield function . . . . .	83
5.2.5	Extension to an anisotropic viscoplastic flow rule . . . . .	88
5.2.6	FEM mesh friction modelling . . . . .	88
5.3	Results and Discussion . . . . .	89
5.4	Conclusions . . . . .	99
<b>6</b>	<b>Conclusions and Recommendations</b>	<b>101</b>
6.1	Conclusions . . . . .	101
6.2	Recommendations . . . . .	104
	<b>References</b>	<b>113</b>
	<b>Acknowledgments</b>	<b>115</b>
	<b>Curriculum Vitae</b>	<b>117</b>
	<b>List of publications</b>	<b>119</b>



# Summary

During the lifetime of polymer surfaces, which for example are used in many applications such as protective eye visors or bearings, friction and abrasive wear may result from scratching and/or sliding cycles. Previous research showed that it is essential to understand the intrinsic mechanical response of the polymer in order to further investigate its frictional and wear response. The Eindhoven Glassy Polymer (EGP) model is a 3D elasto-viscoplastic constitutive model, developed to describe the intrinsic mechanical response of polymer glasses. In the model, the non-linear viscoplastic and thermo-rheological complex response are considered. The main objective of this dissertation is to use and extend this model to study the effect of temperature and anisotropy on the friction and wear response of polycarbonate (PC) and isotactic polypropylene (iPP). This is done via implementing the developed constitutive model in a finite element modelling (FEM) framework and by using a hybrid experimental-numerical approach to compare simulations with experimental results.

Polycarbonate is used in various applications such as face shields, protective glasses, facades or security windows in addition to many other automotive and consumer products. Here the polymer surface is subjected to a large number of scratching and/or sliding cycles which, over time, lead to abrasive wear, degradation and product failure. We investigate the influence of temperature on two-body abrasive wear of polycarbonate surfaces. At elevated temperatures cracks appear on the polycarbonate surface during a single-asperity scratch test. From the intrinsic response it is known that temperature has a detrimental effect on certain key features, i.e. a drop in yield stress, an altered strain-hardening and strain-softening response. A critical positive hydrostatic stress value is selected as a criterion for crack formation. At elevated temperatures the value of the maximum positive hydrostatic stress increases due to the altered intrinsic response of the material on one hand, and the increased adhesive interaction between the diamond scratch tip and the polymer on the other hand.

Polypropylene displays a wide variety in properties and is, therefore, used in many



applications. Many of these applications require enhanced wear resistance to prolong the lifetime of the product. At high plastic deformation-rates, polypropylene starts to soften as a result of heat dissipation. For the first time a thermo-mechanical EGP model is implemented in a FEM-framework. The model is capable of accurately describing the intrinsic response of the material, which opens the door to qualitatively and quantitatively describe its frictional response and understand the damage formation mechanism. We show that the difference in the intrinsic response has a significant influence on the friction and wear response. High strain-rate dependence enhances wear resistance at high scratch speeds. In addition, a high strain hardening counteracts damage formation and thus enhances wear resistance. Moreover, a stick-slip phenomenon is proven to be the main responsible for the observed damage mechanism. The periodic “fish-scale” damage pattern results from periodic changes in resistance during the tip movement. A relation between the intrinsic response of the polymer and the damage formation mechanism is established. Furthermore, the influence of the applied load and scratch speed on damage formation is investigated as well.

Any pre-oriented polymer exhibits mechanical anisotropy. This has a major effect on the contact mechanics. In semi-crystalline polymers it is necessary to include the effect of anisotropy since the crystalline structure can be oriented in a certain direction during processing, e.g. its extrusion direction. The model is further developed by combining Hill’s anisotropic yield criterion with Eyring’s flow rule. An associated viscoplastic flow rule that describes the magnitude and the direction of the viscoplastic flow is incorporated in the model to simulate complex loading conditions such as indentation or scratching. The simulations accurately capture the yield values of iPP in uniaxial loading at a given anisotropic state and material orientation. In addition, the results of the biaxial simulations demonstrate that the constitutive model qualitatively describes the material deformation during both isotropic and anisotropic loading conditions. The model is then used to investigate the effect of pre-stretch on the friction and scratch response of iPP. Results reveal that scratching a polymer surface along the orientation direction results in significant decrease in the resulting penetration and friction force as the material resists deformation along the pre-stretch direction and is mostly deformed perpendicular to the scratching direction. Sliding in transverse direction would result in a similar scratch. However, contrary to machine direction sliding, material is easily deformed along the sliding direction forming a bow wave while the semi-crystalline network obstructs sideways deformation of the bow-wave resulting in a higher contact area with the indenter and as a result a higher friction force than in machine direction. Bottom line, scratching a polymer surface along the pre-stretched direction results in best scratch-resistant response.

Important aspects of contact mechanics such as temperature, thermo-mechanical behaviour and mechanical anisotropy have a significant influence on deformation, adhesion, friction and wear. The developed modelling framework is used as a tool to enable us to better understand such aspects and their influences. Combining the developed macro model with a micromechanical model is the most plausible future work to further study contact mechanics of semi-crystalline and filled-systems polymers.



# Chapter 1

## Introduction

### 1.1 Motivation

The motivation of this work is to study the tribological response, i.e. friction and wear, of polymers in contact. Polymer products are used in various medical and industrial applications such as artificial joints, gears, bearings and protective glasses. Such products are subjected to a large number of sliding cycles which, over time, can lead to abrasive wear, damage formation and/or failure.

Previous studies have investigated the tribological properties of unfilled and filled polycarbonate quantitatively via Finite Element Method (FEM) simulations by implementing a proper material constitutive model [1,2], i.e. a model that captures the polymers intrinsic mechanical response, and using a rate-independent friction (stick-slip) model.

Certain applications, such as gears, are subjected to high temperatures that affect their intrinsic response and can influence their frictional response. In addition, applications such as bearings are subjected to large sliding speeds in which heat can be generated due to large plastic deformation rates. Moreover, semi-crystalline polymers, such as polyolefins, are usually anisotropic due to their processing conditions. This creates the need to study the effect of temperature, thermo-mechanical behaviour and mechanical anisotropy on deformation, adhesion, friction and wear.

## 1.2 Tribology on different scales

The word tribology is derived from the root “tribo” meaning rubbing and the suffix “logy” meaning the study of. Tribological interactions have a significant impact on various areas of engineering and everyday life, it has progressively moved down the length scales with time. Tribological scale levels as presented by Holmberg [3] are shown in Figure 1.1. Studying friction gained popularity starting from the Industrial Revolution in the early 1800’s where sliding and rotary machinery such as the spinning wheel and steam engine were required to operate efficiently. At that era, the classical work of Leonardo da Vinci formed the foundation of tribology and frictional interactions [4]. Da Vinci established the two laws of friction which were later rediscovered by Guillaume Amontons [5] and extended by Charles-Augustin de Coulomb [6].

In the early 20<sup>th</sup> century, the attention started to focus on the surface interaction between single components on smaller scales. The early work of Archard [7] and Bowden et al. [8] aimed towards defining the true area of contact on a micro-scale level. The work of Greenwood and Williamson [9] forms the basis for a number of multi-asperity models introducing the multiple-asperity contact. Greenwood’s recent work shows that the summation of all small contact areas along the asperities is the same to that of a smooth asperity of the same general shape [10]. In this respect, microtribology relates to aspects such as asperity interactions, elastic and plastic deformations, abrasive wear and fracture. The Finite Element Method (FEM) emerged in the early 70’s of the last century and has gained popularity over the years due to the increased computational power. The application of FEM to tribological problems involves the discretization of the volumes of contacting bodies. It also involves the implementation of a proper constitutive material model that properly describes the intrinsic response of the material. Moreover, an appropriate treatment of the contact interaction between the contacting bodies and a proper definition of the real contact area in the case of single-asperity sliding is essential for an accurate description of the macroscopic scratch response.

Recently, research started to focus on the molecular and atomic levels in order to better clarify the tribological effects observed on larger scales, i.e. micro- and macro scales. Nanotribology or molecular tribology includes phenomena related to the interaction between molecules and atoms, such as the effects of van der Waal’s forces and related interatomic phenomena. Nowadays, it is possible to study friction and wear on a molecular scale thanks to techniques such as atomic force microscopy and other surface analysis methods [11]. From a modelling perspective, friction and associated phenomena are accessible via molecular dynamic simulations (MD) of sliding surfaces in order to

investigate the atomic scale contact mechanisms [12].

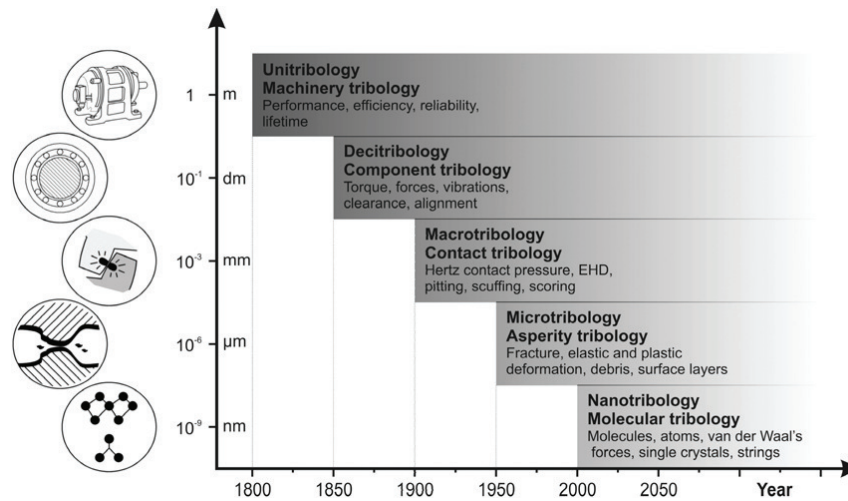


**Figure 1.1:** Timeline illustrating the scales of tribology from unitribology to nanotribology, the plot is copied from Matthews et al. [13].

### 1.3 Single-asperity scratch test

One common way of studying surface damage, abrasion and wear is scratch testing. Single-asperity scratch test allows the mechanisms behind ductile damage and wear of samples under investigation. The test is a micro-scale level test where a micro-scale rigid indenter penetrates into the surface of a material, then it starts sliding along that surface and plastically deforms it, forming a bow wave in front of the tip. The resulting frictional response is decomposed into an adhesive component, which originates from nano-scale processes, and a deformation component, which is a macro-scale process. This test forms the foundation of this thesis.

### 1.4 Scope of the thesis

Three main aspects are investigated in this dissertation. First, studying the effects of temperature on the tribological properties of polycarbonate and predict crack initiation upon scratching, i.e. the initial stage of wear. Second, establish a relation between the intrinsic response of polypropylene and the damage formation mechanism during single-asperity scratching. This is done via implementing a thermo-mechanically coupled model to account for the dissipative mechanical work upon plastically deforming

polymers. Finally, giving insights on the deformation mechanics associated with scratching anisotropic polypropylene surfaces and an indication on how anisotropy can alter the frictional response of these surfaces upon scratching.

## **1.5 Outline of the thesis**

The effects of temperature on the abrasive wear of polycarbonate surfaces is discussed in **Chapter 2**. In **Chapter 3**, contact mechanics of isotropic polypropylene is investigated using a hybrid experimental/numerical approach considering the thermo-mechanical effects. **Chapter 4** and **Chapter 5** deal with developing and validating the constitutive model to account for material anisotropy and implementing it in FEM-framework to study the contact mechanics of anisotropic polypropylene using a numerical approach. Finally, the main conclusions and recommendations for future research are summarized in **Chapter 6**.

## Chapter 2

# Temperature dependent two-body abrasive wear of polycarbonate surfaces

### Abstract

During the lifetime of polycarbonate surfaces, which for example are used as helmets or protective eye visors, friction and abrasive wear may result from scratching or sliding cycles. Previous research showed that it is essential to understand the intrinsic mechanical response of the polymer in order to further investigate its frictional and wear response. The Eindhoven Glassy Polymer (EGP) model is a 3D elasto-viscoplastic constitutive model, developed to describe the intrinsic mechanical response of polymer glasses. Temperature is a crucial player in the intrinsic response and also plays a pivotal role in the resulting frictional response as tested via a single-asperity scratch test. In the current study, a finite element model is used to investigate the effect of temperature on the frictional response of polycarbonate and detect the onset of crack formation and wear initiation. The results show that temperature has a strong effect on the intrinsic response of the polymer, i.e. drop in yield stress and altered strain-hardening and strain-softening response. However, it has a minute effect on its frictional response, the simulation model is able to capture this response quantitatively. In addition, cracks are observed experimentally at elevated temperature. A critical positive hydrostatic stress value is selected as a criterion for crack formation. It has been shown that at elevated temperatures the value of the maximum positive hydrostatic stress increases due to the altered intrinsic response of the material on one hand, and the increased adhesion between the tip and the polymer on the other hand.

---

Reproduced from: Tarek Kershah, Stan F.S.P. Looijmans, Patrick D. Anderson, Lambert C.A. van Breemen. Temperature dependent two-body abrasive wear of polycarbonate surfaces. *Wear*, 440–441, 203089 (2019)



## 2.1 Introduction

Polymers display excellent tribological properties, they are often favoured above their metal counterparts in applications where friction and wear resistance are important. Polycarbonate (PC) is used in various applications such as face shields, protective glasses, facades or security windows in addition to many other automotive and consumer products. Here the polymer surface is subjected to a large number of scratching or sliding cycles which, over time, lead to abrasive wear, degradation and failure. This makes it necessary to study the frictional behaviour of the polymers. Many studies aimed to investigate the tribology of polymers, however, due to complex contact conditions [14–17], and many experimental variables, the problem needs to be simplified. In order to do so, the single-asperity sliding test, known as scratch test, is used. It resembles the actual contact situation of the polymer product using a well-defined contact situation. The pioneering work of Bowden and Tabor [18] was the first to study the frictional response in which they presumed that the friction force can be additively decomposed into an adhesion and a deformation-related component.

Boyce et al. [19] developed a constitutive model describing the large inelastic deformation of glassy polymers in which the effects of strain rate, pressure, temperature, true strain softening, and strain hardening have been accounted for. As the Finite Element Method (FEM) started to emerge, benefiting from ongoing increase in computational power, new possibilities are now available to study non-linear contact problems. Larsson's group implemented a finite-strain constitutive material model in a FEM-framework to study the Vickers and Berkovic indentation of elasto-plastic materials [20, 21]. However, contact analysis for polymers is more complex due to their non-linear visco-elastic behaviour. Anand et al. [22] developed a continuum model for the elasto-viscoplastic deformation of an amorphous polymeric solid during micro-indentation, in which the FEM simulation reproduces the experimentally measured indentation on PMMA with reasonable accuracy. Van Breemen et al. [23] captured the rate and history dependence of polycarbonate and PMMA on both macroscopic and microscopic scale using flat-tip micro-indentation. The next step after indentation was to model the single-asperity scratching. Leroch et. al. [24] and Varga et. al. [25] used mesh-free numerical simulations such as Smoothed particle hydrodynamics (SPH) and Material Point Method (MPM) to simulate scratch-induced surface damage on an elasto-viscoplastic materials. These methods tackle the problem of severe deformations which is usually encountered in FEM simulations, however, they are computationally more expensive to use. Many studies aimed to analyse complex responses in sliding friction via experimental and numerical techniques [26–35]. Most provide a valuable description of the frictional response, but only on the qualitative

level. The reason is that these studies imply that there is no dependence on strain rate of sliding velocity, and hence it does not correctly capture the visco-elastic pre-yield behaviour of polymer glasses. The Eindhoven Glassy Polymer (EGP) model, which is a 3D elasto-viscoplastic model, was developed to describe the intrinsic mechanical response of polymer glasses [36–39]. Recently this model has been extended to capture the intrinsic response of polymer glasses with multiple relaxation times [40]. The work of Van Breemen et al. [1] and Krop et al. [2] used the EGP model to couple intrinsic material properties to the observed frictional response and investigate the effect of applied load and scratch velocity on the penetration and friction force on polycarbonate. The effect of temperature however, is still poorly understood when it comes to single-asperity scratching. It is expected that temperature has an influence on penetration and friction force during scratching due to the altered pre- and post-yield responses [41,42].

The main objective of this study is using a hybrid experimental-numerical approach to investigate the effect of temperature during single-asperity scratching on the tribological properties of polycarbonate in order to create polymers with superior properties and prolong its wear resistance and lifetime. Polycarbonate is selected as model material because of its well-defined mechanical properties and intrinsic response. The sample preparation and the scratch set-up and testing procedures are discussed in Section 2.2. We use the extended version of the EGP model [40], where the characterization of the intrinsic material properties is discussed in Section 2.3. Physical ageing and mechanical rejuvenation have a profound influence on the scratch response which is taken care of in the model [43]. In the results section we compare numerical simulations with the experimental results to quantitatively describe the temperature effect on the frictional response of the polymer surface and predict the onset of crack formation.

## 2.2 Experimental

### 2.2.1 Materials and sample preparation

The material used in this study is Lexan 141R, a high molecular weight injection moulding grade polycarbonate (Sabic Innovative Plastics, Bergen op Zoom, The Netherlands). Samples of dimensions  $20 \times 20 \times 1 \text{ mm}^3$  were cut from the centre of injection moulded plates, produced in a mould of  $90 \text{ }^\circ\text{C}$ . The experimental protocol used to prepare these plates is given in more detail elsewhere [44]. After being stored at room temperature for over a year, the samples are dried for three days in a vacuum oven at  $80 \text{ }^\circ\text{C}$  before being annealed for two weeks at a temperature of  $120 \text{ }^\circ\text{C}$ . Subsequently the samples are air-cooled to room temperature under ambient conditions. The thermo-mechanical history as described above is needed to bring the material as close to equilibrium as possible, in order not to influence the thermodynamic state during scratch testing at elevated temperatures. The surface roughness of the samples is well below the threshold value of 1% of the in-situ surface penetration upon scratching, because of the polished interior of the mould. Optical profilometry as discussed in the next paragraph is used to validate that the surface roughness is considerably low and hence will not influence the lateral force measurement upon scratch testing.

### 2.2.2 Testing

Single-asperity sliding friction experiments are performed using a CSM Micro Indenter (CSM Instruments SA, Peseux, Switzerland) extended with an in-house developed temperature control stage. After setting the temperature to a specific value ( $23$ ,  $60$  or  $80 \text{ }^\circ\text{C}$ ), the system is equilibrated for one hour before starting the actual tribology measurements. Normal loads, ranging from  $100$ - $500 \text{ mN}$ , are applied to the sample via a conical diamond indenter tip, with a cone angle of  $90^\circ$  and a top radius of  $50 \text{ }\mu\text{m}$ . A diamond indenter induces high contact-stress which resembles an extreme loading condition that a polycarbonate surface may be subjected to. The intention is to reach a contact stress above which cracks start to form and wear starts to initiate. After load application, a constant sliding velocity is applied, values of  $1 \text{ }\mu\text{m/s}$ ,  $10 \text{ }\mu\text{m/s}$ , and  $100 \text{ }\mu\text{m/s}$  are used. The surface penetration and lateral friction force are measured as a function of scratch distance. Each combination of normal load and lateral sliding velocity is applied at least three times to check for reproducibility. All experimental results presented in the next section are averages of three scratches. Surface topologies before and after scratch experiments are measured using a Sensofar Pl $\mu$ 2300 optical profilometer (Sensofar Group, Barcelona, Spain). By using a setup of confocal lenses the sample is aligned horizontally,

whereafter the system is moved over a distance of 20-40  $\mu\text{m}$  in the out-of-plane direction. A Nikon Plan Fluor 50x/0.80 EPI lens is then used to construct three-dimensional patterns of the sample topology. Before the scratch tests are performed, a surface roughness in the order of 20 nm is measured. Post-mortem, the residual scratch profiles are measured by means of this technique.

## 2.3 Modelling

### 2.3.1 Constitutive model

The 3D elasto-viscoplastic constitutive model employed in this work consists of multiple Maxwell elements connected in parallel to a neo-Hookean spring. The model, see Van Breemen et al. [40] for more details, is based on an additive decomposition of the total stress  $\boldsymbol{\sigma}$  into a driving stress  $\boldsymbol{\sigma}_s$  and a hardening stress  $\boldsymbol{\sigma}_r$ :

$$\boldsymbol{\sigma} = \boldsymbol{\sigma}_s + \boldsymbol{\sigma}_r. \quad (2.1)$$

The hardening stress is modelled with a neo-Hookean spring and accounts for the stress contribution of the entangled molecular network:

$$\boldsymbol{\sigma}_r = \frac{G_r}{J} \tilde{\mathbf{B}}^d, \quad (2.2)$$

herein,  $G_r$  denotes the hardening modulus,  $\tilde{\mathbf{B}}^d$  is the deviatoric part of the isochoric left Cauchy-Green strain tensor, and  $J$  is the volume change ratio. The driving stress is additively decomposed into a hydrostatic and deviatoric part:

$$\boldsymbol{\sigma}_s = \boldsymbol{\sigma}_s^h + \boldsymbol{\sigma}_s^d = \kappa(J - 1)\mathbf{I} + \sum_{i=1}^n G_i \tilde{\mathbf{B}}_{e,i}^d, \quad (2.3)$$

where,  $\kappa$  is the bulk modulus,  $G$  is the shear modulus,  $\tilde{\mathbf{B}}_e^d$  is the elastic deviatoric part of the isochoric left Cauchy-Green strain tensor, subscript  $i$  refers to a specific mode, and  $n$  denotes the number of modes. The deviatoric part  $\boldsymbol{\sigma}_s^d$  is coupled to the plastic deformation rate tensor  $\mathbf{D}_p$  via a non-Newtonian flow rule:

$$\mathbf{D}_{p,i} = \frac{\boldsymbol{\sigma}_{s,i}^d}{2\eta_i}, \quad (2.4)$$

where  $\eta_i$  are the viscosities of each Maxwell element which are described by the extended Eyring flow rule. This flow rule takes the pressure dependence and strain softening into

account:

$$\eta_i = \eta_{0,\text{ref},i} \frac{\bar{\tau}/\tau_0}{\sinh(\bar{\tau}/\tau_0)} \exp\left[\frac{\mu p}{\tau_0}\right] \exp[S_a R_x(\bar{\gamma}_p)], \quad (2.5)$$

where  $\eta_{0,\text{ref},i}$  are the reference viscosities of each Maxwell element,  $\bar{\tau}$  is the total equivalent stress,  $\tau_0$  defines the characteristic shear stress,  $p$  is the hydrostatic pressure, the pressure dependency is governed by the parameter  $\mu$ , the physical ageing is contained in the state parameter  $S_a$ . The function  $R_x(\bar{\gamma}_p)$  describes the strain softening process using modified Carreau-Yasuda relation:

$$R_x(\bar{\gamma}_p) = \left[ \frac{1 + (r_0 \cdot \exp(\bar{\gamma}_p))^{r_1}}{1 + r_0^{r_1}} \right]^{(r_2-1)/r_1}, \quad (2.6)$$

where  $\bar{\gamma}_p$  is the equivalent plastic strain, and  $r_0$ ,  $r_1$ , and  $r_2$  are the fitting parameters. When temperature is considered,  $\tau_0$  is determined using the following equation:

$$\tau_0 = \frac{k_b T}{V^*}, \quad (2.7)$$

where  $k_b$  is the Boltzmann's constant,  $V^*$  is the activation volume, and  $T$  represents the temperature. In addition, a temperature-dependent pre-exponential factor is added to the Eyring equation:

$$\eta_i = \eta_{0,\text{ref},i} \frac{\bar{\tau}/\tau_0}{\sinh(\bar{\tau}/\tau_0)} \exp\left[\frac{\mu p}{\tau_0}\right] \exp[S_a R_x(\bar{\gamma}_p)] \exp\left[-\frac{\Delta U}{RT} \left(\frac{T - T_{\text{ref}}}{T_{\text{ref}}}\right)\right], \quad (2.8)$$

where  $\Delta U$  is the activation energy,  $R$  is the universal gas constant, and  $T_{\text{ref}}$  is the room temperature.

### 2.3.2 Intrinsic response and model parameters

In order to obtain the model parameters of PC, the intrinsic response of the polymer is investigated. Single-element FEM compression simulations are performed and fitted to experiments. Figure 2.1a presents the strain-rate dependence of compressive stress-strain curves of PC. Upon an increase in strain rate the yield stress increases, and the post-yield response shifts accordingly. The polymer strain-rate dependency is relevant since the single-asperity scratch tests are performed at different scratch velocities, and the strain rate is not constant throughout the material. Consequently, the frictional response is dependent on the scratch velocity. Figure 2.1b shows the drop in yield stress which is observed at higher temperatures due to the softening of the polymer. As mentioned in the introduction, due to the drop in yield stress at elevated temperatures, more penetration

and a higher friction force are expected in the scratch simulation. Moreover, the post-yield response changes as well; less strain softening and less strain hardening is observed at elevated temperatures. This post-yield response plays a determining role in strain localization [45, 46]. If the strain hardening is strong enough it stabilizes the deformation zones and resist the formation of localized plastic deformation zones caused by strain softening. Therefore, it is expected that such behaviour will contribute to localized strain accumulation during scratching and will increase the chance of crack formation especially at high normal loads. Figure 2.2 shows simulations and experimental yield stress values at different strain rates and temperatures. The experimental values are adopted from [47]. The slopes for different temperatures are similar, because PC is a thermo-rheologically simple material. This observation indicates that the dependence of the yield stress on strain rate and temperature can be separated and that there is no coupling effect between them. It is important to mention that PC has a secondary relaxation mechanism, however, this mechanism plays no role of importance at temperatures equal to, or above, room temperature provided that the deformation rates are moderate [48]. The thermodynamic state parameter  $S_a$  of the material is determined by using indentation simulations and fitting them to the experiments, analogous to [40]. Since our samples have been annealed at 120 °C for two weeks, the thermodynamic state parameter is relatively high;  $S_a = 50$  as opposed to  $S_a = 29$  for the compression samples. The high value of  $S_a$  results in a higher yield strength and larger yield drop. The reflection of this in the single-asperity scratch tests is a decrease in the penetration due to this higher yield, and as a result, the friction force decreases. The obtained material parameters for PC are tabulated in Table 2.1, the relaxation spectra in Table 2.2, and the strain-hardening modulus and strain-softening fitting parameters are presented in Table 2.3. The constitutive model is implemented in the FEM package MSC.Marc in order to simulate the single-asperity scratch test.

**Table 2.1:** Material parameters of PC.

$\kappa$ [MPa]	$S_a$ [-]	$\mu$ [-]	$V^*$ [nm <sup>3</sup> ]	$\Delta U$ [kJ/mole]
3750	50	0.08	5.8	291

### 2.3.3 Finite element mesh and friction modelling

The single-asperity scratch simulation is symmetric (Figure 2.3), therefore, only half of the polymer surface is meshed. The meshed volume is  $0.2 \times 0.2 \times 0.8$  mm<sup>3</sup>. Although quadratic elements are often used to prevent shear locking we use linear elements which

**Table 2.2:** Reference spectrum of PC, adopted from Van Breemen et al. [40].

Mode	$\eta_{0,\text{ref},i}$ [MPa.s]	$G_i$ [MPa]
1	$2.10 \times 10^{11}$	$3.52 \times 10^2$
2	$3.48 \times 10^9$	$5.55 \times 10^1$
3	$2.95 \times 10^8$	$4.48 \times 10^1$
4	$2.84 \times 10^7$	$4.12 \times 10^1$
5	$2.54 \times 10^6$	$3.50 \times 10^1$
6	$2.44 \times 10^5$	$3.20 \times 10^1$
7	$2.20 \times 10^4$	$2.75 \times 10^1$
8	$2.04 \times 10^3$	$2.43 \times 10^1$
9	$1.83 \times 10^2$	$2.07 \times 10^1$
10	$1.68 \times 10^1$	$1.81 \times 10^1$

**Table 2.3:** Strain-hardening modulus and strain-softening fitting parameters of PC as function of temperature.

	23 °C	60 °C	80 °C
$G_r$ [MPa]	27	24	23
$r_0$ [-]	0.95	1	1
$r_1$ [-]	50	50	50
$r_2$ [-]	-3	-1.85	-1.6

are preferred in contact analysis [49]. The surface of the polymer has greatest interest, and is subjected to the highest stresses, so, mesh refinement is applied to this area. The symmetry plane is fixed in y-direction and the sides are restrained in x- and z-direction. A fixed uniform temperature distribution boundary condition is applied to the mesh; 23 °C, 60 °C, and 80 °C are applied to test the frictional response at these temperatures. The indenter tip radius is 50  $\mu\text{m}$ , and is modelled as a rigid surface. The simulation is split in two parts, first indentation with constant normal load for 25 s, then sliding with constant velocity and normal load.

The Coulomb friction model is used, and to avoid numerical singularities, the step

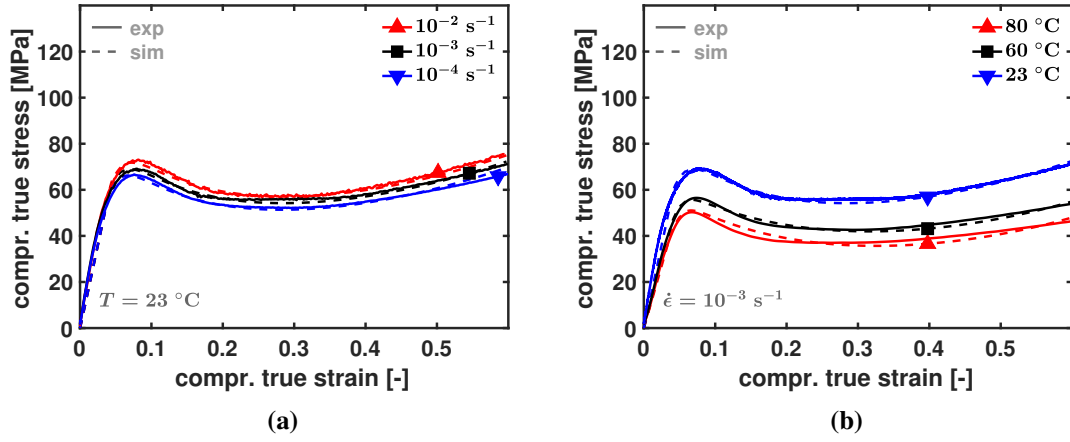


**Figure 2.1:** Uniaxial compression simulations results of PC (a) at different strain rates, (b) at different temperatures.

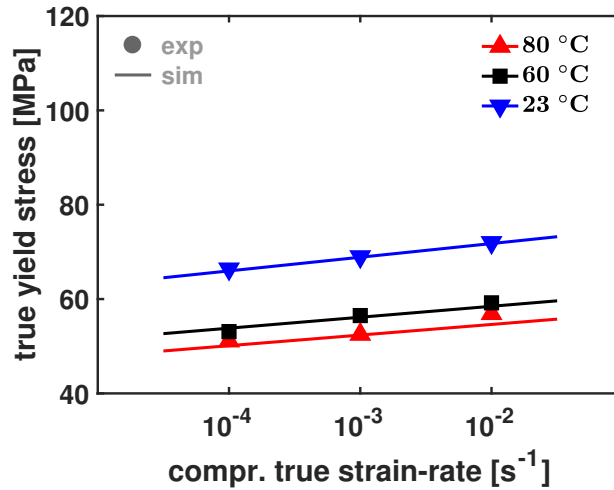


**Figure 2.2:** Yield stress of PC at various strain rates and temperatures. No coupling effect between rate dependency and temperature dependency.

function is approximated with an arctangent model:

$$\mathbf{f}_t = -\mu_f f_n \frac{2}{\pi} \arctan \left[ \frac{\|\mathbf{v}_r\|}{\delta} \right] \mathbf{t}, \quad (2.9)$$

where  $\mathbf{f}_t$  and  $f_n$  are the friction and normal forces respectively,  $\mu_f$  the local friction coefficient,  $\mathbf{v}_r$  is the relative sliding velocity, and  $\mathbf{t}$  is the tangential vector. The value of  $\delta$  dictates the value of the relative velocity below which sticking occurs. The smaller the



value of  $\delta$  the better the estimation of the friction force, however, it becomes more difficult to reach convergence. Van Breemen et al. [1] showed that the friction force strongly depends on the friction coefficient. A high friction coefficient results in more indenter-polymer sticking, which leads to the formation of a bow wave in front of the sliding tip. This bow wave causes the tip to be pushed out of the surface and drastically changes the deformation zone. Van Breemen et al. [1] used a friction coefficient value of  $\mu_f = 0.20$  for PC which gives a best representation of the experimental data, while Krop et al. [2] used a value of  $\mu_f = 0.25$ , the difference solely comes from the differences in surface roughness of the tips used. In our case, a local friction coefficient value of  $\mu_f = 0.25$  is found to give the best description of the experimental scratching of polycarbonate at room temperature, and is kept constant at different scratch velocities and normal loads. At elevated temperatures however, we test the possibility of increasing the friction coefficient due to the expected increased adhesion at these temperatures.

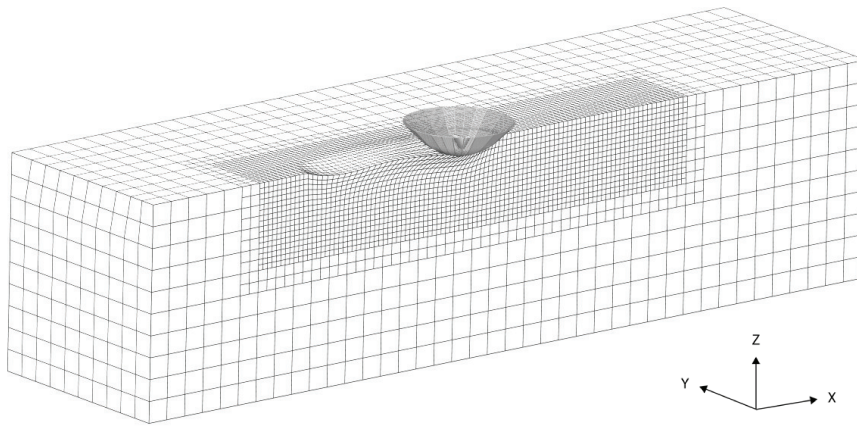


**Figure 2.3:** FEM mesh of single-asperity scratch simulation.

## 2.4 Results and Discussion

### 2.4.1 Scratch and frictional response

Scratch tests are performed at room temperature and two elevated temperatures; 60 °C and 80 °C, and at three different normal loads; 100 mN, 300 mN, and 500 mN, and three different scratch velocities; 1  $\mu\text{m/s}$ , 10  $\mu\text{m/s}$ , and 100  $\mu\text{m/s}$ . The typical single-asperity scratch response is shown in Figure 2.4. Figure 2.4a presents the value of tip penetration into the polymer after indentation till it reaches the steady state. Figure 2.4b displays the corresponding frictional response. During simulation, the friction force takes longer time to reach steady state compared to experiments. The reason is the use of the approximated arctangent model to smoothen the stick-slip transition. In this model the parameter  $\delta$  dictates the value below which sticking occurs, this value is around 10% of the relative velocity. In reality however, the stick-slip transition happens more abruptly leading to friction force build-up more rapidly. Simulations accurately capture the experimental response at room temperature, however, at elevated temperatures the penetration is overestimated, and the friction force is underestimated. This observation suggests that the local friction coefficient value of  $\mu_f = 0.25$  is accurate at room temperature, however, at high temperatures it seems that there is more adhesion which leads to more friction between the tip and the polymer resulting in more material accumulation in front of the tip (bow wave). This pile-up of material in front of the tip increases the friction force and pushes the tip upwards. Figure 2.5 shows the experimental (a) and simulation data (b) of the indenter penetration into the surface of the polymer at various normal loads and scratch velocities with the resulting frictional response illustrated in Figures 2.5c and 2.5d. Generally speaking, higher loads, lower scratch velocities, and higher temperatures introduce more mesh deformation and convergence becomes challenging. For this reason, when convergence cannot be reached, the fitting lines of simulations are extrapolated and the values are plotted using open markers. At higher applied loads we observe more penetration and friction force. The same happens at lower scratch velocity due to the strain-rate dependency that results from the visco-elastic nature of the polymer. In other words, at low scratch velocity there is less material resistance to the indenter motion, so, it penetrates more into the surface, and more polymer gets in contact with the indenter resulting in an increased friction force. Higher temperatures lower the yield stress of the material and the post-yield response changes as well, i.e. less strain softening and less strain hardening, leading to more penetration and friction force. The observation of underestimation of friction force with overestimation of penetration depth at elevated temperatures is observed in almost all cases making the need for friction coefficient adjustment at elevated temperatures plausible.

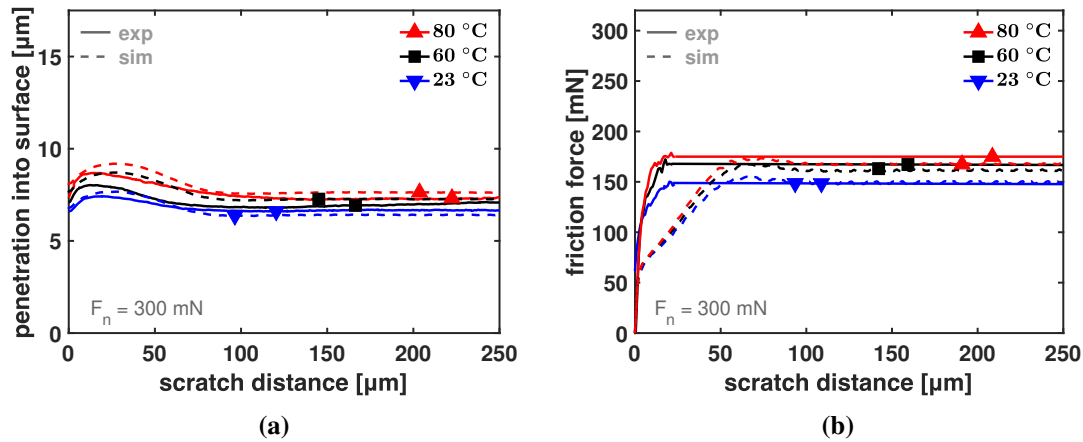


**Figure 2.4:** Single-asperity scratch results of PC at 100  $\mu\text{m/s}$  scratch velocity; (a) penetration into the surface versus sliding distance, (b) friction force versus sliding distance. Simulations accurately capture the experimental response at room temperature, however, at elevated temperatures the penetration is overestimated, and the friction force is underestimated.

## 2.4.2 Friction coefficient

It has been reported that friction coefficient is temperature dependent for some materials [50]. A rationale based on the fact that high temperatures lead to more adhesion between the polymer and the tip, resulting in more friction. From the previous results in Figures 2.4a and 2.4b it has been shown that our simulation underestimates the friction force at elevated temperatures. Instead of using a friction coefficient value of  $\mu_f = 0.25$  at 60 °C and 80 °C degrees, values of  $\mu_f = 0.27$  and  $\mu_f = 0.28$  are used respectively. The scratch response at these values shows a better estimation of the penetration depth Figure 2.6a, this results from the bigger bow wave formed in front of the material due to increased adhesion, therefore, pushing the indenter up. As a result of the material pile-up, more material gets in contact with the tip increasing the friction force. The friction force values show better agreement with the experimental data, see Figure 2.6b. The entire stress field around the indenter changes as the friction coefficient increases at elevated temperatures. Figure 2.7a shows a 3D view of the mesh after single-asperity scratching at 300 mN, scratch velocity of 100  $\mu\text{m/s}$ , and a temperature of 80 °C. A higher stress is observed using higher friction coefficient resulting from an increased adhesion and resistance of smooth tip movement, see Figure 2.7b. The increase of adhesion creates more sticking and accumulates the material in front of the tip which obstructs the horizontal movement of the tip and introduces an additional friction force. With less friction and resistance force, the tip will slip, i.e. move smoother. Now that we adjusted our friction coefficient

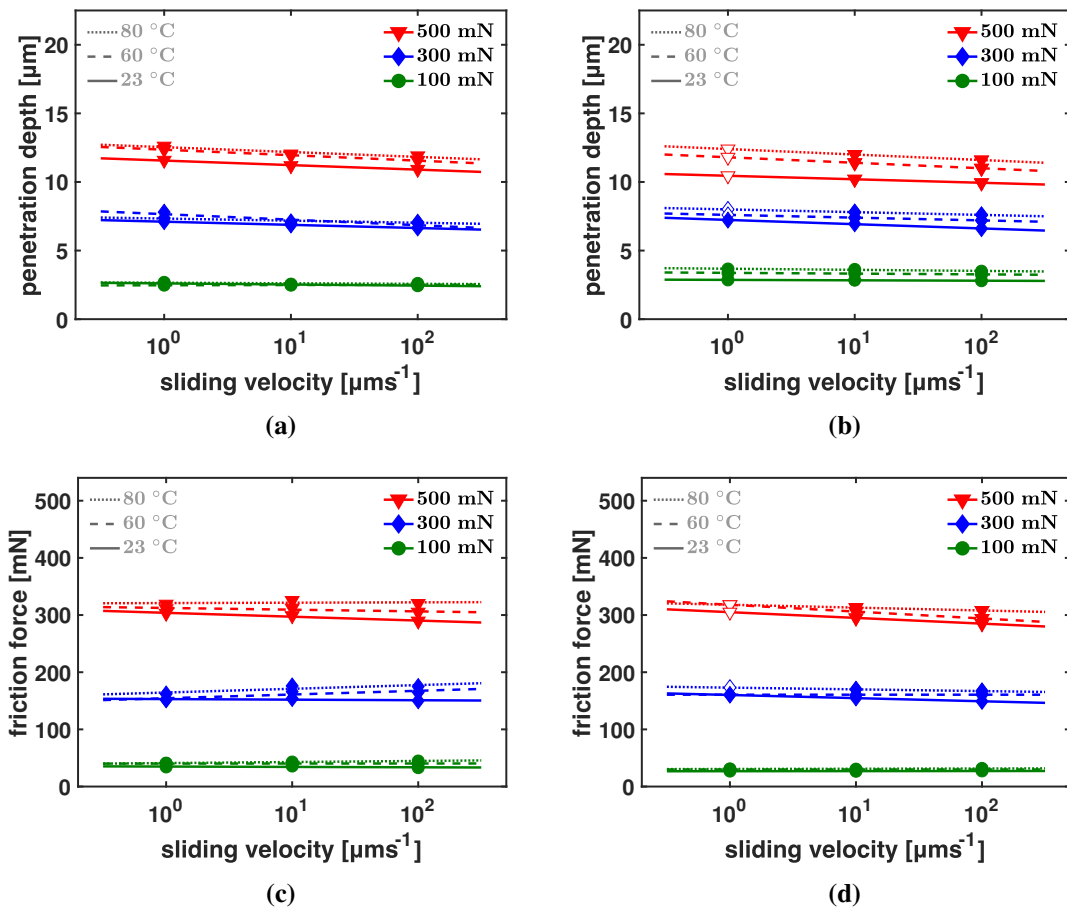


**Figure 2.5:** Penetration into the surface versus sliding distance of PC using a 50 μm tip at 100 mN, 300 mN, and 500 mN, and scratch velocities; 1 μm/s, 10 μm/s, and 100 μm/s; (a) experiments, (b) simulations. The resulting friction force; (c) experiments, (d) simulations. Lines are a guide to the eye. Open markers are extrapolated simulation values.

at elevated temperatures, the new penetration response values at 300 mN normal load are shown in Figures 2.8a and 2.8b with the resulting frictional response illustrated in Figures 2.8c and 2.8d. The new results show better agreement of both the penetration depths and friction force at elevated temperatures. Generally speaking, more friction leads to an increase in the frictional shear stress along the contact surface which pushes the tip upwards, however, the increase in lateral force results from the formation of a bow wave in front of the sliding tip. At elevated temperatures, two counteracting effects take place; material softens and friction coefficient, i.e. adhesion increases. The softening of the material leads to more surface penetration, whereas the increased adhesion leads to increased frictional shear stress along the contact surface which pushes the tip upwards.

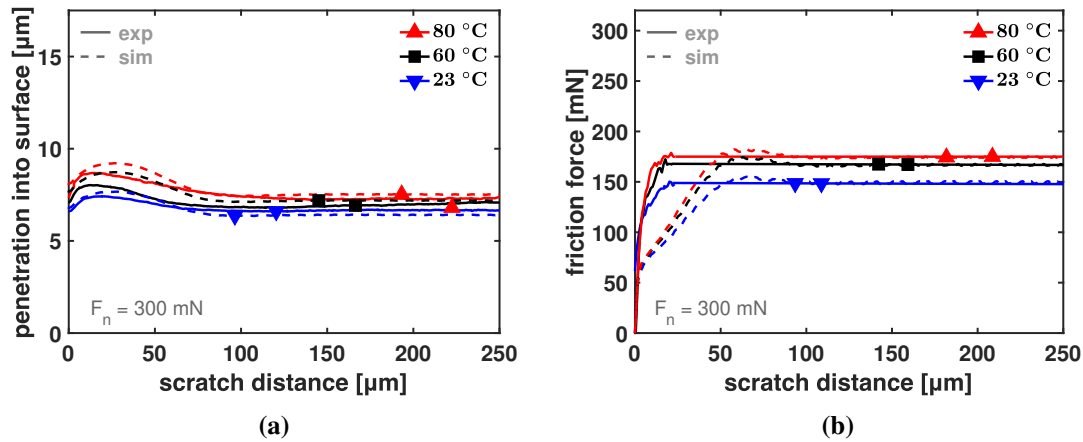
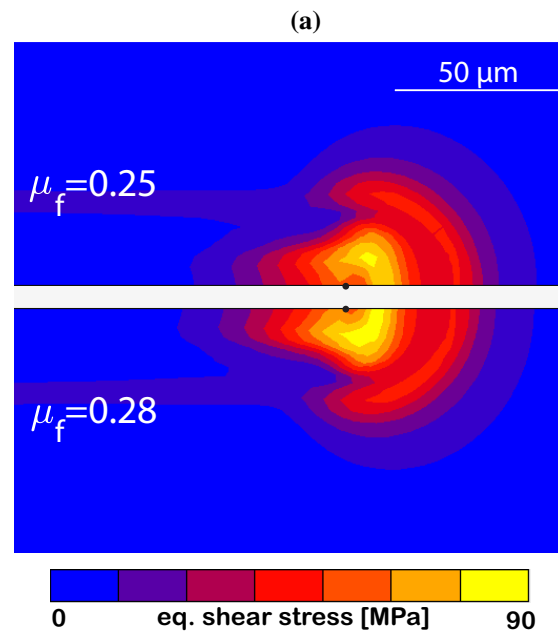
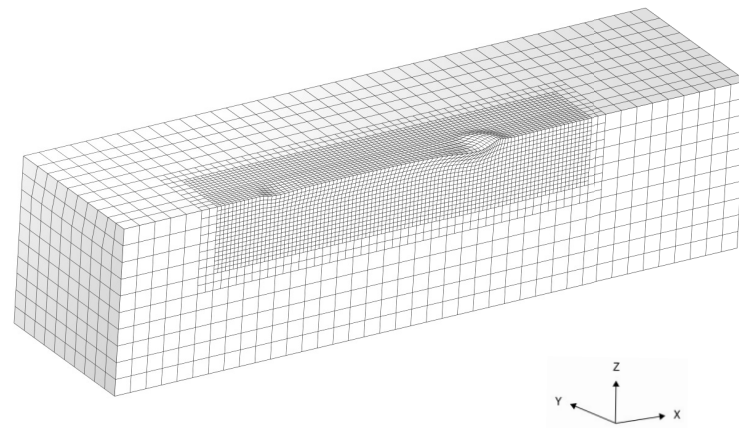


**Figure 2.6:** Simulation results of single-asperity scratch test of PC at 100 μm/s scratch velocity using a friction coefficient value of  $\mu_f = 0.25$  at room temperature and  $\mu_f = 0.27$  and  $\mu_f = 0.28$  at 60 °C and 80 °C degrees respectively; (a) penetration into the surface versus sliding distance, (b) friction force versus sliding distance.

This is why temperature has little effect on surface penetration. However, the significant increase in lateral force, despite the decrease in penetration, results from the formation of a bow wave in front of the sliding tip. This proves that the hypothesized friction coefficient dependency on temperature is valid.

### 2.4.3 Crack formation

It has been reported that failure on polycarbonate surfaces initiates when a critical positive hydrostatic stress is reached [51–53]. These critical values can be reached earlier by increasing normal load, decreasing sliding velocities, or increasing temperatures. In this work we are interested in studying the effect of temperature on the friction and crack formation on polycarbonate surfaces. Figure 2.9 shows that cracks start to appear at 80 °C. Temperature rise leads to a change in the intrinsic response of the polymers as has been shown in Figure 2.1b. A drop in yield stress is observed at elevated temperature accompanied by a change in the balance between strain softening and strain hardening. The drop in yield stress leads to materials softening, which in principle allows the indenter to go deeper into the polymer surface, creating a larger contact area between the tip and polymer, leading to higher friction force values. However, as discussed before, this effect is counterbalanced by the increase in friction coefficient at elevated temperatures, leading to minor temperature dependence of the friction force and penetration depth. On the other hand, the change of balance between the strain softening and strain hardening, i.e. less strain softening and less strain hardening, results in localized plastic deformation. In



(b)

**Figure 2.7:** (a) A 3D view of the mesh after single-asperity scratching of 300 mN normal load, scratch velocity 100  $\mu\text{m/s}$ , and temperature 80  $^{\circ}\text{C}$ . (b) The equivalent shear stress field when looking at -Z-direction using friction coefficient value of  $\mu_f = 0.25$  (top) and  $\mu_f = 0.28$  (bottom). Black dot represents the tip centre. More stress is observed using higher friction coefficient resulting from more adhesion and resistance of smooth tip movement.

single-asperity scratching this leads to localized strain accumulation during scratching,

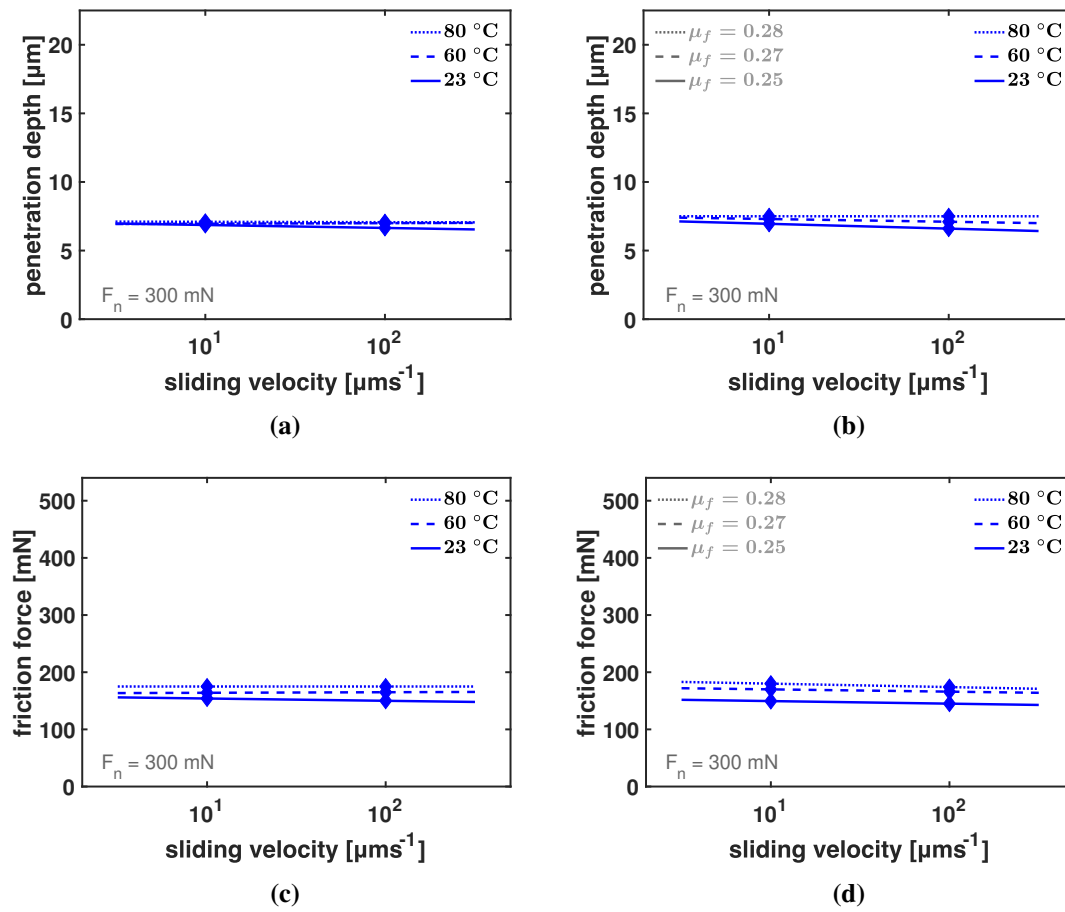


**Figure 2.8:** Penetration into the surface versus sliding distance of PC using a  $50 \mu\text{m}$  tip at 300 mN, and scratch velocities;  $10 \mu\text{m/s}$ , and  $100 \mu\text{m/s}$ , using adjusted friction coefficient values at elevated temperatures; (a) experiments, (b) simulations. The corresponding friction force; (c) experiments, (d) simulations. Lines are a guide to the eye.

and enhancing the formation of cracks. However, the change in the intrinsic response is not the only determining factor for crack formation. In the previous subsection it is proven that the friction coefficient is temperature-dependent and might have a role in the formation of cracks. This rationale is based on the fact that an increase in friction coefficient results in more adhesion enhancing the formation of bow wave, i.e. material pile-up in front of the tip, and transition between stick and slip becomes less smooth which leads to change in the entire stress field as shown earlier. This change is expected to increase the positive hydrostatic stress as the material suddenly slips under the indenter. Since cracks start to appear at the load case of 300 mN and  $10 \mu\text{m/s}$  at  $80 \text{ }^\circ\text{C}$ , this load case is selected and compared with the same situation but at room temperature. As mentioned earlier, a critical positive hydrostatic stress will be used as a criterion for crack formation.

This critical value is approximately 80 MPa for Polycarbonate [51]. It is shown that at room temperature the value of the maximum positive hydrostatic stress  $\sigma_{\max}^h = 42$  MPa, while at 80 °C the value is  $\sigma_{\max}^h = 62$  MPa, with both cases at friction coefficient value of  $\mu_f = 0.25$ , see Figure 2.10. The increase in the hydrostatic stress comes solely, in this case, from the altered intrinsic response of the material at high temperature, i.e. the drop in yield stress in addition to strain-hardening and strain-softening imbalance, which leads to strain localization during scratching resulting in more penetration and a higher friction force. Figure 2.11 shows the temperature dependence of the maximum hydrostatic stress observed in the simulations. In case the deformation is mainly elastic, i.e. at an applied load of 100 mN, the maximum hydrostatic stress is independent of temperature and sliding velocity. When the normal load is increased, due to the difference in the post-yield deformation response, the maximum value strongly increases with increasing temperature. At lower sliding velocities, the hydrostatic stress values are larger compared to high scratch speeds, as a result of the viscoelastic nature of the material.

Next, we test the hypothesis of using a higher friction coefficient value at 80 °C with a value of  $\mu_f = 0.28$ . The resulting maximum hydrostatic stress value reaches  $\sigma_{\max}^h = 69$  MPa, see Figure 2.12. This increase represents about 25% of the total increase in the hydrostatic stress and pushes the total positive hydrostatic stress to its critical value. This percentage comes only from the altered interaction between the polymer-tip surface, i.e. more sticking and adhesion and a less smooth stick-slip transition. This increase is depicted in Figure 2.11 with dashed-lines. At 80 °C, this value becomes close to the critical hydrostatic stress. Experimentally, at these test conditions failure may be initiated because of inhomogeneities in the material, leading to stress concentrations.

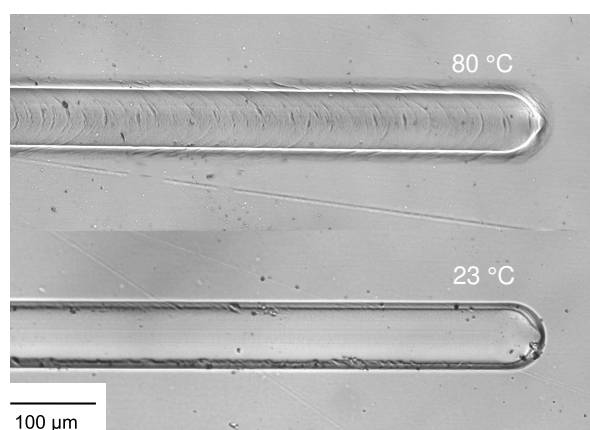


**Figure 2.9:** Scratch on PC surfaces at 300 mN and 10 μm/s at room temperature and 80 °C. Crack formation barely starts to appear at 80 °C.



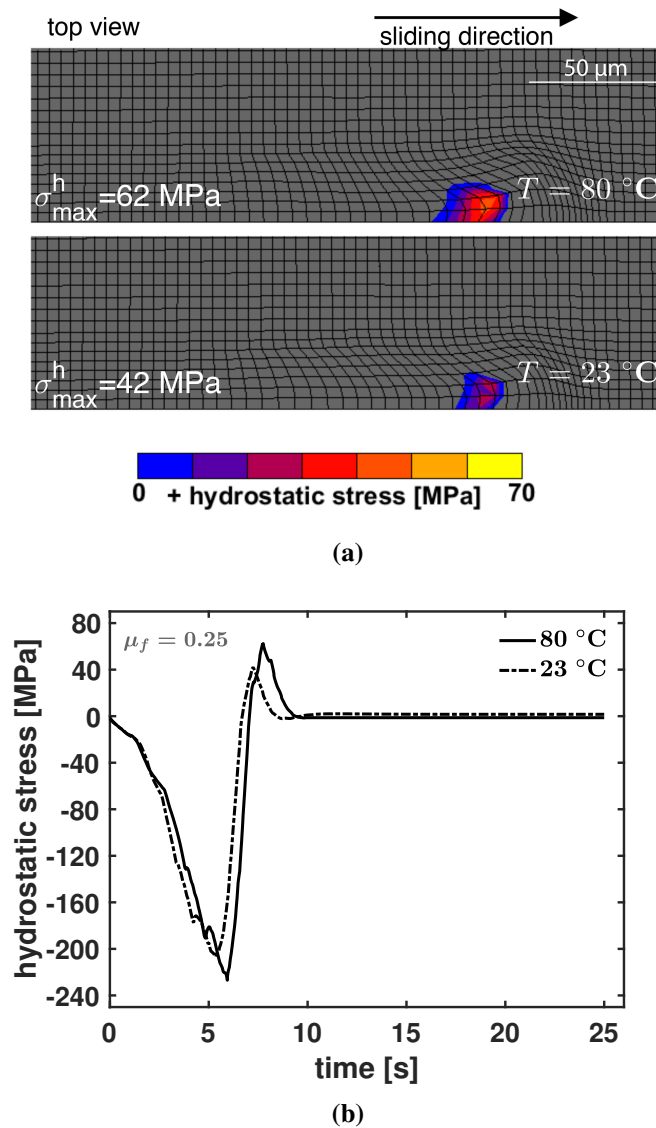


**Figure 2.10:** (a) FEM simulation showing the values of positive hydrostatic stress along the surface when looking at -Z-direction at  $80\text{ }^{\circ}\text{C}$  and  $23\text{ }^{\circ}\text{C}$  at  $300\text{ mN}$  and  $10\text{ }\mu\text{m/s}$ , (b) evolution of hydrostatic stress along a selected element in the middle of the scratch surface for both cases. Friction coefficient  $\mu_f=0.25$  is used for both cases.

It should be noted that hydrostatic stress is a local variable and is dependent on mesh refinement. Although no full convergence is reached with the current level of mesh refinement, the change in maximum hydrostatic stress is small. Further increasing the level of refinement does not add much to the critical values reached, while it substantially increases the computational time. A further study of abrasive wear has been performed

via investigating the abrasive wear factor  $f_{ab}$  first introduced by Zum Gahr [54] and used by Varga et. al. [55]. The factor is proven to give a value of  $f_{ab} = 0$  at all loads, speeds and temperatures both experimentally and numerically. This implies that our scratch tests only involve ductile ploughing and no cutting, and that the cracks appearing at elevated temperatures does not involve any material loss.

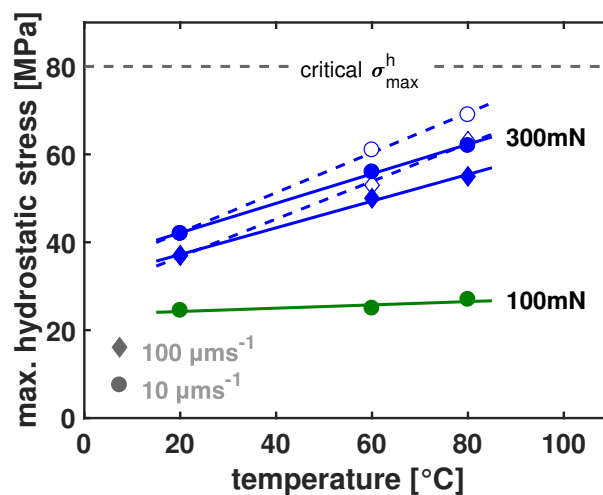


**Figure 2.11:** Maximum hydrostatic stress obtained by scratch simulations on PC at the indicated conditions. The solid lines represent the simulations performed with a friction coefficient of  $\mu = 0.25$ . The dashed lines correspond to the simulations where the friction coefficient is temperature dependent. The open symbols belonging to the dashed lines indicate the simulation conditions at 60 °C with  $\mu = 0.27$  and at 80 °C with  $\mu = 0.28$ . The experimentally obtained critical hydrostatic stress for PC is indicated at the top.

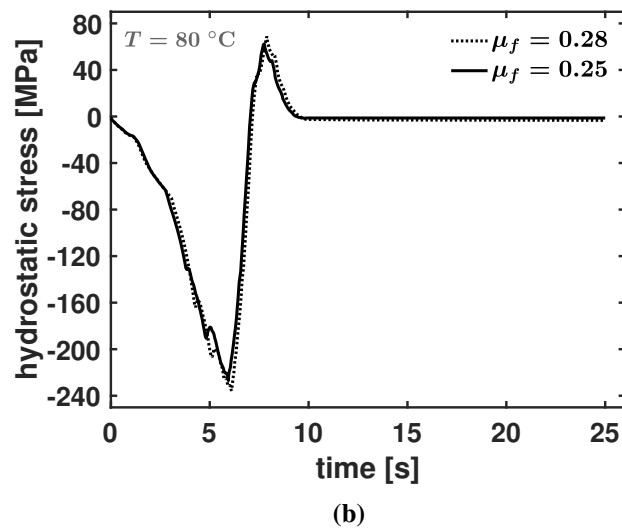
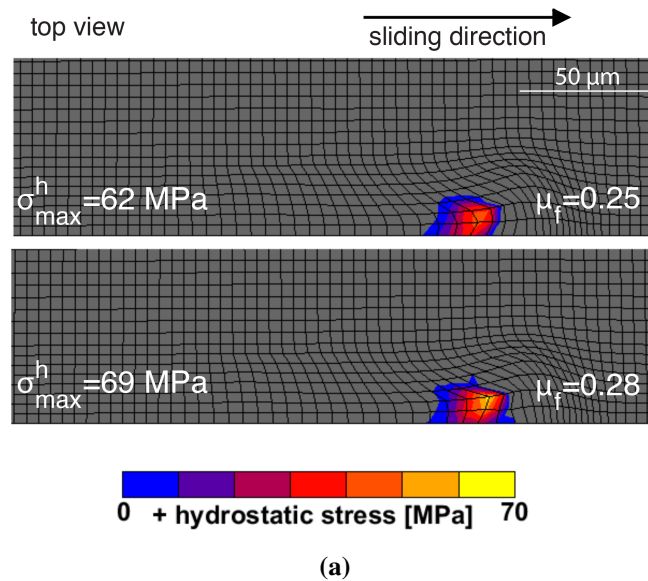


**Figure 2.12:** (a) FEM simulation showing the values of positive hydrostatic stress along the surface when looking at - Z-direction at 80 °C using friction coefficient  $\mu_f=0.25$  and  $\mu_f=0.28$ , (b) evolution of hydrostatic stress along a selected element in the middle of the scratch surface for both cases.

## 2.5 Conclusions

The hybrid experimental-numerical approach is successfully used to quantify the friction and abrasive-wear response of polycarbonate at room and elevated temperatures. The

model has been implemented in a FEM-framework to test the intrinsic response of polycarbonate at various strain rates and temperatures. Successfully, FEM simulations of the single-asperity scratch test were performed and compared to experimental results. From the results we conclude that:

1. More tip penetration is observed at elevated temperatures due to the drop in intrinsic yield stress. This leads to an increased indenter-polymer contact area resulting in higher friction force.
2. The strain-rate dependency of the polymer leads to more resistance of the material to scratch at higher scratch velocities resulting in less penetration and frictional response.
3. Higher temperatures lower the yield stress of the material and the post-yield response changes as well, i.e. less strain softening and less strain hardening. This behaviour leads to the formation of localized plastic deformation zones and localized strain accumulation during scratching, which enhances the formation of cracks.
4. At high temperatures there is more adhesion which leads to more friction between the tip and the polymer resulting in more material accumulation in front of the tip. This pile-up of the material increases the friction force and pushes the tip upwards. Adjusting the friction coefficient at elevated temperature enables the model to accurately predict the resulting friction force.
5. A critical positive hydrostatic stress value is selected as a criterion for crack formation initiation which leads to wear initiation. It has been shown that at elevated temperatures the value of the maximum positive hydrostatic stress increases solely from the altered intrinsic response of the material at these temperatures, given that the friction coefficient value is the same.
6. The hypothesized increase in the friction coefficient is tested to examine its effect on hydrostatic stress. The increased sticking and adhesion and less smooth stick-slip transition leads to higher positive hydrostatic stress values, which accounts for about 25% of the total increase observed. This means that the crack formation observed at elevated temperatures comes from the change in the intrinsic response on one hand, and the change in the polymer-tip interaction on the other hand.



## Chapter 3

# Thermo-mechanically coupled modelling of a single-asperity scratch on an isotropic isotactic polypropylene surface

### Abstract

Isotactic polypropylene (iPP) is a low cost semi-crystalline polymer that is easy to process, has a wide variety in properties and is, therefore, used in many applications. Many of these applications require enhanced wear-resistance to prolong the lifetime of the product. Essential is to first investigate the intrinsic response of the material in order to describe its friction and wear response. In this respect, a hybrid experimental-numerical approach is used to couple the intrinsic response to the single-asperity scratch response. The numerical model used is a 3D elasto-viscoplastic model based on the Eindhoven Glassy Polymer (EGP) model. For the first time a coupled thermo-mechanical EGP model is implemented in a Finite Element Method (FEM)-framework. The model is capable of accurately describing the intrinsic response of the material, which opens the door to qualitatively and quantitatively describe its frictional response and understand the damage formation mechanism (i.e. the initiation of wear). In this study,  $\alpha$ - and  $\beta$ -phase iPP are studied. We show that the difference in the intrinsic response between the two phases has a significant influence on the friction and wear response. Moreover, a stick-slip

---

Reproduced from: Tarek Kershah, Stan F.S.P. Looijmans, Patrick D. Anderson, Lambert C.A. van Breemen. Thermo-mechanically coupled modelling of a single-asperity scratch on an isotropic isotactic polypropylene surface. *Tribology International*, 141, 105946 (2020)

phenomenon is proven to be the main responsible for the damage mechanism observed. The observed periodic “fish-scale” damage pattern results from periodic changes in resistance during the tip movement. A relation between the polymer intrinsic response and the damage formation mechanism is established. The influence of the applied load and scratch speed on damage formation is investigated as well.

### 3.1 Introduction

Nowadays, semi-crystalline polymers are used in many applications where moving parts are in contact. The reason is that semi-crystalline polymers possess excellent physical properties such as a light weight and a high wear resistance. Polymers are favoured above their metal counterparts in many applications such as artificial joints, gears, and bearings.

The background of this study is the methodology developed in our group over last two decades where numerical simulations are combined with experiments in order to link the intrinsic behaviour of the polymer to its frictional response. The constitutive model framework used is the Eindhoven Glassy Polymer (EGP) model [23, 38, 39, 43, 47, 56], which, like the Boyce-Parks-Argon model [19, 57] and the Oxford Glass-Rubber (OGR) model [58–60] accurately describes the deformation kinetics of glassy polymers. The constitutive model was extended to better capture the non-linear visco-elastic response (multi-mode) [37, 40] and the thermo-rheological complex systems (multi-process) [56]. Recently, Van Breemen et al. [1] and Krop et al. [2] used the EGP model to couple intrinsic material properties to the observed frictional response on both unfilled and particle-filled polycarbonate. In practice however, for example in bearing cages and medical implants such as knee or hip replacements, semi-crystalline polymers are used [61–65]. Generally speaking, semi-crystalline polymers exhibit high strength, better wear and chemical resistance than glassy polymers.

Semi-crystalline polymers have a large variety of morphological structures. Therefore, contrary to glassy polymers, semi-crystalline systems display a large variation in mechanical properties and lifetime depending on for instance the cooling rate, applied pressure, and presence of anisotropy [66]. We chose isotactic polypropylene (iPP) as a model material since it is one of the widely used semi-crystalline polymers, in addition to its well-defined mechanical properties [67–71].

In this study we aim to link the intrinsic material behaviour to the observed friction and wear response, and obtain a comprehensive understanding of the influence of intrinsic response on macroscopic deformation, frictional energy loss, and damage mechanism using single-asperity scratching simulations. Single-asperity scratch simulations have been previously used to simulate the damage formation on polypropylene surface [72]. In addition, Looijmans et al. [73] experimentally investigated the effect of pre-stretch on the frictional response of iPP using single-asperity scratch with a rigid diamond indenter. However, a solid link between the intrinsic response of the polymer and its scratch and frictional response has never been established. A key aspect in this study is



the thermo-mechanically coupled modelling that is introduced into the EGP model and implemented in a Finite Element Method (FEM)-framework for the first time. The reason is, like metals, a percentage of the mechanical work of polymers has been found to be dissipative, in other words, heat is generated due to plastic deformation [74, 75]. The thermal model is analogue to the work of Boyce et al. [75] and Klompen et al. [76]. It is used to first quantitatively investigate the material intrinsic response, and help predict the material frictional response. An additional important aspect is the significant difference in strain hardening between the intrinsic response of  $\alpha$ - and  $\beta$ -iPP. It has been previously shown that strain hardening plays a determining role in strain localization [45, 46]. Strain hardening stabilizes the deformation zones and resists the formation of localized plastic deformation zones. In this respect, we expect to see a different frictional response between the two phases of iPP. In addition, we aim to understand the damage formation mechanism of iPP (i.e. the initiation of wear). It has been shown previously that a stick-slip phenomenon plays a major part in the damage formation mechanism of iPP [77]. The gradual build-up of friction force during sticking, and the sudden drop during slipping results in the so-called fish-scale damage pattern by plastically drawing the material along the scratch direction [78–80]. The intrinsic response of the polymer must have an influence on such a mechanism. Moreover, the normal load and scratching speed significantly affect the stick–slip process of the polymer, and thus, influence the damage-formation mechanism. The sample preparation and nano indentation testing procedures are discussed in Section 3.2. The detailed description of the EGP constitutive model and its extension to a thermo-mechanically coupled model is discussed in Section 3.3. In the same section the FEM scratch model is also demonstrated. In the results section we compare numerical simulations with the experimental results to study the damage formation and the parameters influencing it.

## 3.2 Experimental

### 3.2.1 Materials and sample preparation

An injection moulding grade iPP homopolymer with weight-averaged molar mass  $M_w$  of 320 kg/mol and polydispersity  $M_w / M_n$  of 5.4 is kindly provided by SABIC (Riyad, Saudi Arabia). This particular grade was selected because the intrinsic deformation kinetics of its main crystal phases are well-characterized by Caelers et al. [71]. Compression response data is adopted from this work. Experimental data regarding the scratch response of  $\alpha$ -phase iPP is adopted from a previous work [73]. Polymer granules are molten at 230 °C and manually compressed between glass slides to ensure a smooth surface with respect to the indenter geometry. Polymer films of approximately 500  $\mu\text{m}$  in thickness, are kept isothermal in the melt for 10 minutes to erase thermo-mechanical history and subsequently cooled to room temperature. Using this procedure,  $\alpha$ -phase samples with a crystallinity of about 61% are obtained. Analogously,  $\beta$ -phase samples are prepared from granules containing 0.1 wt%  $\beta$ -nucleating agent (NJSTAR NU100 New Japan Chemical Group). The exact compounding procedure of this material can be found elsewhere [70]. Samples having a volumetric crystallinity of 64% were obtained, using the thermal protocol described above.

### 3.2.2 Sliding friction experiments

An MTS Nano Indenter XP is used to perform scratch test experiments by sliding a conical, diamond indenter tip (cone angle 90°, top radius 50  $\mu\text{m}$ ) over the smooth polymer surface. The normal load applied to indenter geometry, as well as the sliding velocity, are kept constant during a single sliding friction experiment. Normal loads are varied between 200-400 mN at sliding velocities ranging from 1 till 100  $\mu\text{m/s}$ . The penetration depth and lateral force are recorded as function of sliding distance. To ensure steady-state measurements, scratch tests of 1 mm in length are performed. At each combination of applied load and sliding velocity, the scratch response is measured three times to check for reproducibility.

## 3.3 Constitutive Modelling

### 3.3.1 The EGP model for thermo-rheologically simple polymers

The 3D elasto-viscoplastic constitutive model used, see Van Breemen et al. [40] for more details, consists of multiple Maxwell elements connected in parallel to a neo-Hookean

spring. In the model the total stress  $\boldsymbol{\sigma}$  is split into the driving stress  $\boldsymbol{\sigma}_s$  and the hardening stress  $\boldsymbol{\sigma}_r$ :

$$\boldsymbol{\sigma} = \boldsymbol{\sigma}_s + \boldsymbol{\sigma}_r. \quad (3.1)$$

Physically, the hardening stress is interpreted as a rubber elastic contribution of the entangled network. Mathematically, it is described with a simple neo-Hookean relation:

$$\boldsymbol{\sigma}_r = \frac{G_r}{J} \tilde{\mathbf{B}}^d, \quad (3.2)$$

herein,  $G_r$  denotes the hardening modulus,  $\tilde{\mathbf{B}}^d$  is the deviatoric part of the isochoric left Cauchy-Green strain tensor, and  $J$  is the volume change ratio. The driving stress is attributed to intermolecular interactions [37, 43] and is split into a hydrostatic and a deviatoric part [38]:

$$\boldsymbol{\sigma}_s = \boldsymbol{\sigma}_s^h + \boldsymbol{\sigma}_s^d = \kappa(J - 1)\mathbf{I} + \sum_{i=1}^n G_i \tilde{\mathbf{B}}_{e,i}^d, \quad (3.3)$$

where,  $\kappa$  is the bulk modulus,  $G$  is the shear modulus,  $\tilde{\mathbf{B}}_e^d$  is the elastic deviatoric part of the isochoric left Cauchy-Green strain tensor. The subscript  $i$  refers to a specific mode, and  $n$  denotes the number of modes [40]. The plastic deformation-rate tensor  $\mathbf{D}_p$  is related to the deviatoric stress  $\boldsymbol{\sigma}_s^d$  via a non-Newtonian flow rule:

$$\mathbf{D}_{p,i} = \frac{\boldsymbol{\sigma}_{s,i}^d}{2\eta_i}, \quad (3.4)$$

where  $\eta_i$  are the viscosities of each Maxwell element which are described by the extended Eyring flow rule. This flow rule was extended [39, 81–83] to take the pressure dependence and strain softening into account:

$$\eta_i = \eta_{0,\text{ref},i} \frac{\bar{\tau}/\tau_0}{\sinh(\bar{\tau}/\tau_0)} \exp\left[\frac{\mu p}{\tau_0}\right] \exp[S_a R_x(\bar{\gamma}_p)], \quad (3.5)$$

where  $\eta_{0,\text{ref},i}$  is the reference viscosity of each Maxwell element,  $\bar{\tau}$  is the total equivalent stress,  $\tau_0$  defines the characteristic shear stress,  $p$  is the hydrostatic pressure, the pressure dependency is governed by the parameter  $\mu$ , the physical ageing is contained in the state parameter  $S_a$ . The softening function  $R_x(\bar{\gamma}_p)$  describes the strain-softening process, i.e. the erasure of thermal history upon the inception of plastic deformation. Klompen et

al. [43] expressed  $R_x(\bar{\gamma}_p)$  as a function of  $\bar{\gamma}_p$  using a modified Carreau-Yasuda relation:

$$R_x(\bar{\gamma}_p) = \left[ \frac{1 + (r_0 \cdot \exp(\bar{\gamma}_p))^{r_1}}{1 + r_0^{r_1}} \right]^{(r_2-1)/r_1}, \quad (3.6)$$

where  $\bar{\gamma}_p$  is the equivalent plastic strain, and  $r_0$ ,  $r_1$ , and  $r_2$  are the fitting parameters. When temperature is considered, a temperature-dependent pre-exponential factor is added to the Eyring equation:

$$\eta_i = \eta_{0,\text{ref},i} \frac{\bar{\tau}/\tau_0}{\sinh(\bar{\tau}/\tau_0)} \exp\left[\frac{\mu p}{\tau_0}\right] \exp[S_a R_x(\bar{\gamma}_p)] \exp\left[-\frac{\Delta U}{RT} \left(\frac{T - T_{\text{ref}}}{T_{\text{ref}}}\right)\right], \quad (3.7)$$

where  $\Delta U$  is the activation energy,  $R$  is the universal gas constant,  $T$  represents the temperature, and  $T_{\text{ref}}$  is the room temperature. In addition,  $\tau_0$  is determined using the following equation:

$$\tau_0 = \frac{k_b T}{V^*}, \quad (3.8)$$

where  $k_b$  is the Boltzmann's constant and  $V^*$  is the activation volume.

### 3.3.2 Extension to thermo-rheologically complex behaviour

The experimental findings of Van Breemen et al. [56] clearly show the existence of a secondary molecular process in iPP as it has been tested over broad range of strain rates. This thermo-rheologically complex behaviour contributes to an increased strain-rate dependency of the polymer at high strain rates. To capture this complex behaviour of the polymer we use a straightforward extension of Equation 3.1 based on the Ree-Eyring equation [84]:

$$\sigma = \sigma_{s,1} + \sigma_{s,2} + \sigma_r, \quad (3.9)$$

where  $\sigma_{s,1}$  is the driving stress of the primary process ( $\sigma_s$  in Equation 3.3), and  $\sigma_{s,2}$  is the driving stress for the secondary process. Both stresses have their own temperature and rate dependencies. Therefore, each process has its own characteristic values of the activation volume  $V^*$  and activation energy  $\Delta U$ . In comparison to experimental data, Equation 3.9 has been shown to be effective in capturing the response of many polymers including iPP [85].

### 3.3.3 Extension to thermo-mechanically coupled model

A thermo-mechanically coupled model must be used if deformation converts mechanical work into heat through an irreversible process which cannot be neglected relative to other heat sources [86–88]. For metals the amount of dissipated energy is approximately 90 to 95% [75]. Adams et al. [74] showed that around 50% to 80% of the work of deformation is dissipated into heat during cold drawing of polycarbonate. Therefore, in case of applying relatively high deformation rates, it becomes a necessity to use a thermo-mechanically coupled model in order to capture the intrinsic response of the polymer. The model is formulated analogous to Boyce et al. [75]. The general energy balance equation of a 3D system is given by:

$$\rho c_p \dot{T} = -\nabla \cdot \mathbf{q} + \dot{Q}_d, \quad (3.10)$$

where the left hand side represents the rate of change in the internal heat energy per unit volume in the material with  $\rho$  being the material density and  $c_p$  the specific heat capacity. In the first part of the right hand side, the Operator  $\nabla$  acts as the divergence operator, and the vector  $\mathbf{q} = \mathbf{q}(\mathbf{x}, t)$  is a vector field that represents the magnitude and the direction of the heat flow at the point  $\mathbf{x}$  of space and time  $t$ . This vector is given by Fourier's law for an isotropic homogeneous medium where the rate of flow of heat energy per unit volume through a surface is proportional to the negative temperature gradient across it:

$$\mathbf{q} = -k_p \nabla T, \quad (3.11)$$

where  $k_p$  is the proportionality coefficient which represents the polymer thermal conductivity. The second part of the right hand side,  $\dot{Q}_d$ , is the rate of change in the dissipative work done by the driving stress given by:

$$\dot{Q}_d = \Gamma(\boldsymbol{\sigma}_s : \mathbf{D}_{p,i}), \quad (3.12)$$

where  $\Gamma$  is the percentage of mechanical work dissipated into heat. This percentage gradually decreases as the material continues to be strained due to extensive molecular orientation [75].

Next, the boundary conditions should be considered. In compression experiments, steel compression plates are used to compress the sample, while in scratch experiments, the indenter comes in contact with the polymer. In that respect, the change in the heat flux due to the conduction boundary condition is given by:

$$\dot{Q}_a = A_a(k_a/t_a)(T - T_{\text{ref}}), \quad (3.13)$$

where  $A_a$  is the contact area between the sample and the steel compression plates in the compression test or the indenter in the scratch test,  $k_a$  and  $t_a$  are the thermal conductivity and the thickness of the body in contact with the polymer. Similarly heat convection to the surrounding air must be considered, it is given by the following relation:

$$\dot{Q}_c = A_c h_c (T - T_{\text{ref}}), \quad (3.14)$$

where  $A_c$  is the contact area between the sample and the air,  $h_c$  is the heat transfer coefficient of the air. Radiation effects are very small and, therefore, neglected. Since the thermal conductivity of polymers  $k_p$  is relatively small and the volume of the surrounding contact bodies are relatively large with respect to the sample, the surrounding mediums are considered as heat sinks. Therefore, the heat transfer within the polymer will be neglected. Similar to [76], the boundary conditions parts are added to Equation 3.10. The equation of evolution can be written as follows:

$$\dot{T} = \frac{1}{\rho c_p} \left[ \Gamma(\boldsymbol{\sigma}_s : \mathbf{D}_{p,i}) - [(A_c h_c) + A_a (k_a/t_a)](T - T_{\text{ref}}) \right]. \quad (3.15)$$

It is difficult to quantitatively determine the boundary conditions parameters, they are also different for different tests, i.e. compression or scratch. In that respect, a boundary condition parameter  $k$  is used instead and is determined by fitting the simulation results to the experimental compression data. For simplicity the same value of  $k$  will be used in the scratch simulations. This parameter encompasses all the boundary condition parameters in addition to the thermal conductivity and heat transfer coefficient of the mediums which are in contact with the polymer. The final evolution equation is given by:

$$\dot{T} = \frac{1}{\rho c_p} \left[ \Gamma(\boldsymbol{\sigma}_s : \mathbf{D}_{p,i}) - k(T - T_{\text{ref}}) \right]. \quad (3.16)$$

The evolution equation is then solved using the forward Euler method:

$$T_c = T_b + \Delta t \dot{T}, \quad (3.17)$$

where  $T_c$  is the nodal temperature of the current increment,  $T_b$  is the temperature of the previous increment, and  $\Delta t$  is the incremental time step.

### 3.3.4 Friction modelling and FEM mesh

The constitutive model is implemented in the FEM package MSC.Marc in order to simulate the single-asperity scratch test. The Coulomb model is adopted as a friction model. The arctangent model is used to avoid the numerical singularities by smoothing

the stick-slip transition, similar to [1, 2]:

$$\mathbf{f}_t = -\mu_f f_n \frac{2}{\pi} \arctan \left[ \frac{\|\mathbf{v}_r\|}{\delta} \right] \mathbf{t}, \quad (3.18)$$

where  $\mathbf{f}_t$  and  $f_n$  are the friction and normal forces respectively,  $\mu_f$  the local friction coefficient,  $\mathbf{v}_r$  is the relative sliding velocity, and  $\mathbf{t}$  is the tangential vector. The value of  $\delta$  determines the value of the relative velocity below which sticking occurs. A large value of  $\delta$  will guarantee quick convergence but poor estimation of the friction force. A small value will result in better estimation of the friction force at the cost of more computational power, and, if too small, it will be impossible to reach convergence. Many simulations have been used to optimize this parameter. The friction coefficient  $\mu_f$  is determined by fitting the simulations frictional response to experimental data in a fashion similar to Van Breemen et al. [1]. A local friction coefficient value of  $\mu_f = 0.28$  is found to give the best description of the experimental scratching data of both iPP phases.

The single-asperity scratch mesh is shown in Figure 3.1a. Only half of the polymer surface is meshed since the simulation is symmetric. The meshed volume is  $0.2 \times 0.2 \times 0.8 \text{ mm}^3$ . The symmetry plane is fixed in y-direction and the sides are restrained in x- and z-direction. Room temperature is used as an initial condition at each node. An indenter with a tip radius  $50 \text{ }\mu\text{m}$  is used, and is modelled as a rigid body. Mesh refinement is applied to the area of greatest interest, i.e. largest deformation. Figure 3.1b shows the FEM mesh during scratching. First, a normal force  $F_n$  is gradually applied to the indenter for 25 s, then, the scratch cycle takes place at constant scratch speed  $v_s$ .

### 3.3.5 Intrinsic response and model parameters

To investigate the intrinsic response of the polymer, single-element FEM compression simulations are performed and fitted to experimental data, obtained from [71]. The resulting reference spectra of  $\alpha$ - and  $\beta$ -iPP are shown in Tables 3.1 and 3.2. The thermodynamic state parameter of the material,  $S_a$ , is determined by using indentation simulations and fitting them to the experiments, similar to [1]. The material parameters for  $\alpha$ - and  $\beta$ -iPP are obtained from [56] and tabulated in Tables 3.3 and 3.4 respectively. The pressure dependency parameter  $\mu$  is determined from the compressive and tensile data obtained from [70, 71]. The thermal parameters are adopted from [76], and presented in Table 3.5. It should be noted that  $V_1^*$  and  $V_2^*$  are the activation volumes for the primary and secondary molecular processes respectively, the same holds for the activation energies;  $\Delta U_1$  and  $\Delta U_2$ .

The experimental intrinsic response of iPP is plotted in Figure 3.2 by solid lines. The data shows the response of  $\alpha$ -iPP, Figure 3.2a, and  $\beta$ -iPP, Figure 3.2b. Due to the strain-

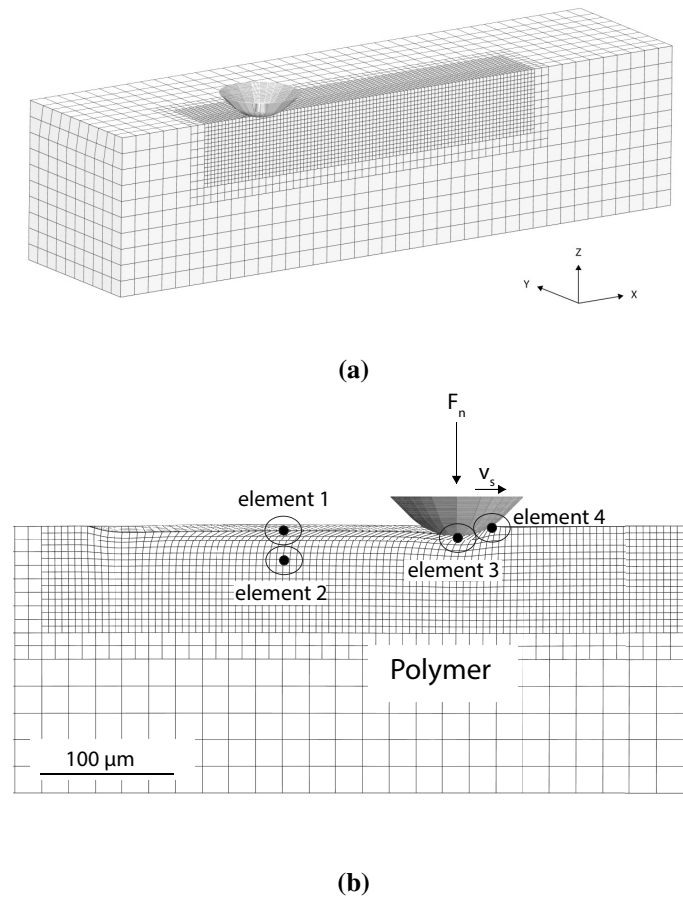


**Figure 3.1:** FEM mesh of single-asperity scratch simulation; (a) 3D view before indentation, (b) side view during scratching showing directions of applied normal force  $F_n$  and scratch velocity  $v_s$  on polymer surface. It also shows the location of the four elements considered to investigate the effect of the thermo-mechanical model, friction coefficient, and scratch speed on deformation kinetics.

rate dependence of the polymer, a higher yield stress is observed at higher strain rates for both phases. Figure 3.3 shows the upper- and lower-yield stress for each phase versus the applied strain rate. The upper-yield stress displays a higher strain-rate dependence than the lower-yield stress. This implies that the upper-yield stress is controlled by a secondary molecular process in addition to the primary one, while only the primary process contributes to the kinetics of the lower-yield stress [56]. The simulation results are fitted to experimental data in order to obtain the model parameters as can be seen in Figure 3.2. The first set of simulations “sim1” plotted by dotted lines clearly shows, at high strain rates, that the post-yield response is not captured by the model. This is due to the internal heat generation at these high rates. Due to high plastic deformation-rates, the material starts to soften as a result of heat dissipation. In addition, there is less



**Table 3.1:** Reference spectrum of  $\alpha$ -iPP.

Process 1	Mode	$\eta_{0,i,ref}$ [MPa.s]	$G_i$ [MPa]
	1	$1.6 \times 10^8$	110
	2	$3.5 \times 10^7$	90
	3	$2.3 \times 10^6$	70
	4	$3.3 \times 10^5$	60
	5	$3.3 \times 10^4$	40
	6	$6.7 \times 10^3$	30
Process 2	Mode	$\eta_{0,i,ref}$ [MPa.s]	$G_i$ [MPa]
	1	$2.4 \times 10^{-2}$	80

**Table 3.2:** Reference spectrum  $\beta$ -iPP.

Process 1	Mode	$\eta_{0,i,ref}$ [MPa.s]	$G_i$ [MPa]
	1	$1.6 \times 10^7$	110
	2	$3.5 \times 10^6$	90
	3	$2.3 \times 10^5$	70
	4	$3.3 \times 10^4$	60
	5	$3.3 \times 10^3$	40
	6	$6.7 \times 10^2$	30
Process 2	Mode	$\eta_{0,i,ref}$ [MPa.s]	$G_i$ [MPa]
	1	$2.4 \times 10^{-2}$	80

time for conduction and convection of the generated heat. This leads to a significant effect on the post-yield response [56, 75]. It should be noted that the existence of a secondary process controlling the upper-yield stress only manifests itself in a higher yield drop as the deformation rates increase within the assessed range of strain rates. The heat generation due to plastic deformation only appears at relatively high strain rates and alters the entire post-yield response. This explains the decrease in slope of the lower-yield stress at the highest strain rate, see Figure 3.3. In this respect it is necessary to

**Table 3.3:** Material parameters of  $\alpha$ -iPP, adopted from [56].

$G_r$ [MPa]	$\kappa$ [MPa]	$S_a$ [-]	$\mu$ [-]	$V_1^*$ [nm <sup>3</sup> ]
1.6	1650	5.0	0.12	3.10
$V_2^*$ [nm <sup>3</sup> ]	$\rho$ [gm/cm <sup>3</sup> ]	$r_0$ [-]	$r_1$ [-]	$r_2$ [-]
3.0	0.90	0.95	2.0	-0.5

**Table 3.4:** Material parameters of  $\beta$ -iPP, adopted from [56].

$G_r$ [MPa]	$\kappa$ [MPa]	$S_a$ [-]	$\mu$ [-]	$V_1^*$ [nm <sup>3</sup> ]
5.0	1650	5.0	0.18	2.90
$V_2^*$ [nm <sup>3</sup> ]	$\rho$ [gm/cm <sup>3</sup> ]	$r_0$ [-]	$r_1$ [-]	$r_2$ [-]
3.0	0.90	0.95	2.0	-0.2

**Table 3.5:** Thermal parameters of  $\alpha$ - and  $\beta$ -iPP, activation energy and specific heat capacity obtained from [76].

$\Gamma$ [-]	$k$ [MPa/K s]	$\Delta U_1$ [kJ/mole]	$\Delta U_2$ [kJ/mole]	$c_p$ (kJ/kg K)
0.6	0.10	274	251	1.92

use a thermo-mechanically coupled model to accurately predict the post-yield response of the polymer. The other set of simulations “sim2” plotted by dashed lines shows the simulation results fitted to the experimental data after implementing the thermo-mechanically coupled model, Equation 3.16 and 3.17, and fitting the parameters  $\Gamma$  and  $k$ . Figure 3.4 shows the temperature evolution due to plasticity-induced heating during the intrinsic simulations of iPP at different strain rates. The results reveal that the model is qualitatively able of determining the temperature evolution due to heat generation resulting from plastic deformation. Higher deformation rates result in more mechanical work dissipated into heat, and less time for cooling and temperature rises. The slight difference in the maximum temperatures between  $\alpha$ -iPP and  $\beta$ -iPP can be related to the slightly higher yield stress of  $\beta$ -iPP at high strain rates.

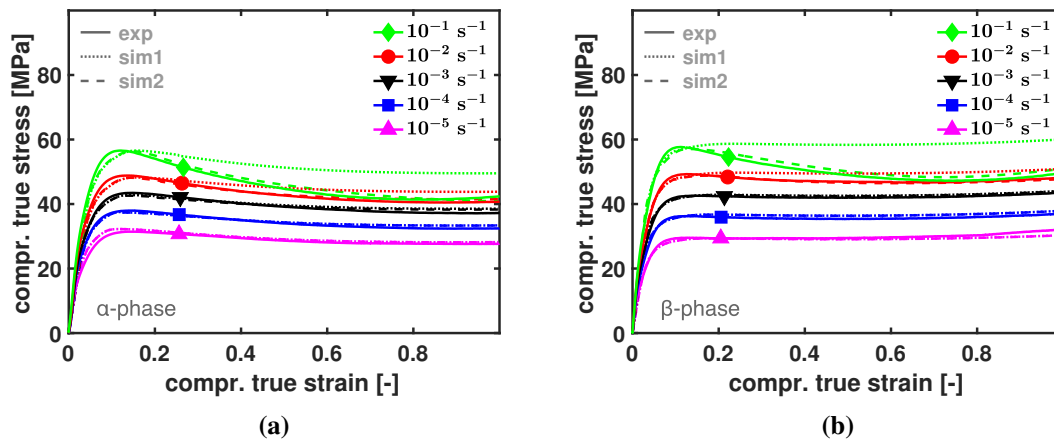


**Figure 3.2:** Fitting uniaxial single-element compression simulation results to experimental data. Sim1 without considering heat generated due to plastic deformation. Sim2 using the thermo-mechanical coupled model. (a)  $\alpha$ -iPP, (b)  $\beta$ -iPP.

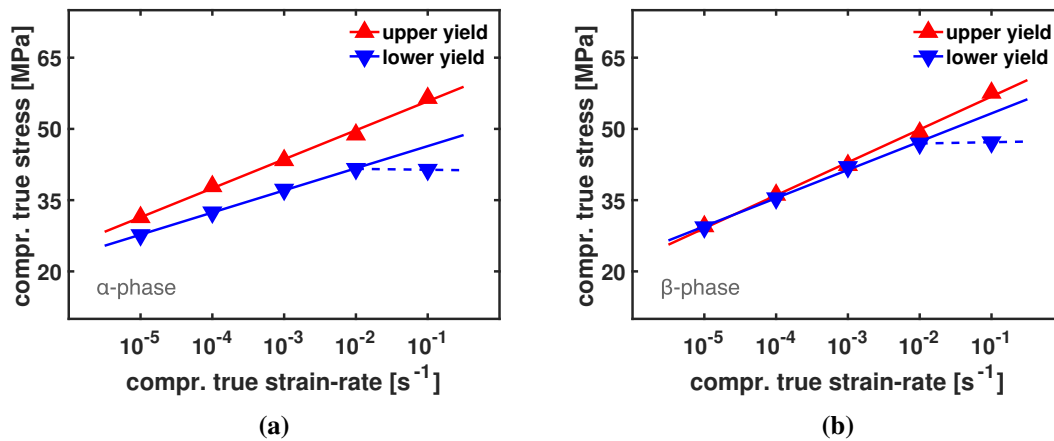


**Figure 3.3:** Upper- and lower-yield stress values of iPP at different strain rates; (a)  $\alpha$ -iPP, (b)  $\beta$ -iPP. Markers are data points, lines are data points fitting. The plastic heat generation leads to a decreased lower-yield slope at higher strain rates (dotted line).

## 3.4 Results and Discussion

### 3.4.1 Influence of the thermo-mechanical model

The use of the thermo-mechanical model is proven to be necessary to capture the intrinsic response of the polymer at high strain rates. The model is expected to have a significant influence on the deformation kinetics during scratch. In order to show this influence, two

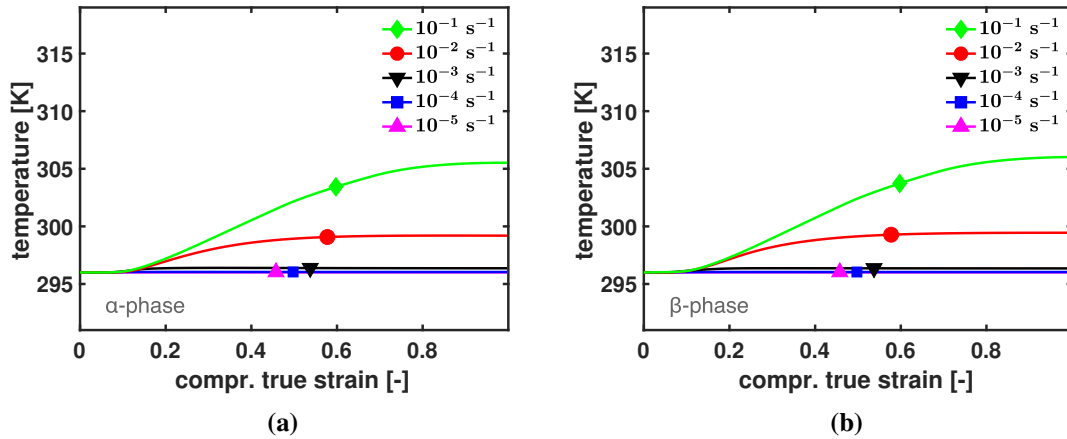


**Figure 3.4:** Uniaxial single-element compression simulation results of temperature evolution due to heat generation resulting from plastic deformation of iPP at different strain rates; (a)  $\alpha$ -iPP, (b)  $\beta$ -iPP.

single-asperity scratch simulations are performed using a mechanical model and a thermo-mechanical model respectively. In these simulations, indentation is first performed for 25 s where a normal load of  $F_n = 200$  mN is gradually built-up, followed by constant-speed scratching of  $v_s = 100$   $\mu\text{m/s}$  for 250  $\mu\text{m}$ . During this study, several elements are considered, see Figure 3.1b. First, element 1 is an element on the surface of the polymer that is chosen to analyse the influence of the thermo-mechanical model on deformation kinetics. Steady-state response is already present when element 1 is reached. The analysis of element 1 only considers the scratch part which takes 2.5 s, while the indentation part which lasts for 25 s is not included. By definition, no mechanical work is dissipated into heat using the mechanical model, and therefore, no change in temperature can be observed, see Figures 3.5a and 3.5b. Due to plastic heat generation using the thermo-mechanical model, material softens and deformation becomes slightly faster, see Figure 3.5c. The equivalent stress is dependent on both deformation rate and temperature. Lower deformation rates and higher temperatures result in lower stresses. The values of deformation rate are almost the same in both cases. However, temperature is significantly higher when using the thermo-mechanical model. This leads to lower value of equivalent stress due to thermal softening, see Figure 3.5d.

Heat is generated within each element of the FEM mesh according to plastic deformation-rates applied to this element. In order to show the temperature evolution along the mesh, next to element 1, three more elements located in different regions within the mesh, as shown in Figure 3.1b, are considered. As these elements start to deform plastically, heat is generated within each element and the temperature rises, see Figure 3.6. When the amount of heat conduction and convection become larger than heat generation, the temperature

starts to slowly decrease. Element 2 experiences relatively small plastic deformation resulting in only a slight rise in temperature. It is clear from Figure 3.6 that the trend of temperature evolution is proportional to that of the plastic strain  $\bar{\gamma}_p$  evolution.

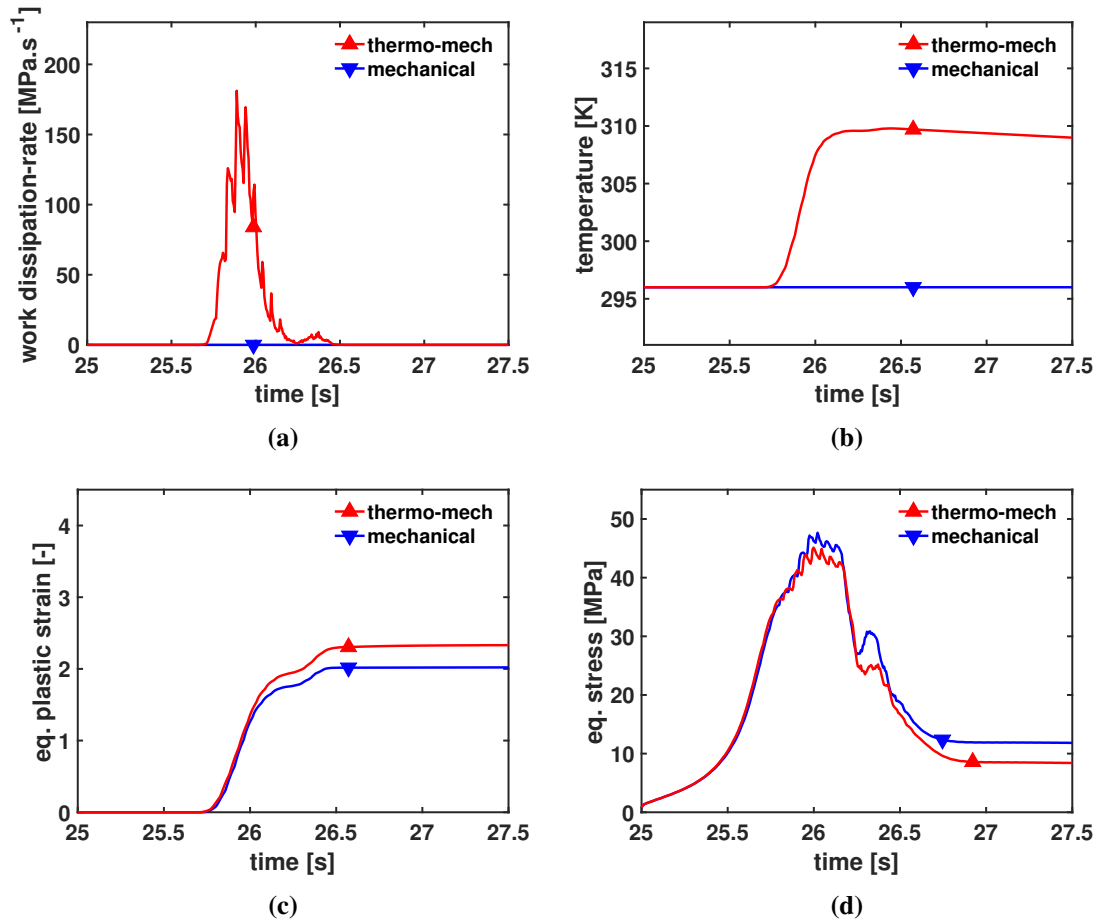


**Figure 3.5:** The effect of using a thermo-mechanical model for scratch simulation and its influence on the deformation kinetics of element 1; (a) rate of mechanical work dissipated into heat, (b) the resulting rise in temperature, (c) the equivalent plastic strain, (d) the equivalent stress.

### 3.4.2 Effect of friction on heat generation

Friction is a crucial aspect in contact mechanics. Generally, more friction implies more adhesion between bodies in contact. This leads to more deformation in case of scratching, which is manifested in more distorted elements in simulations, compare Figures 3.7a and 3.7b. Since we use a thermo-mechanical model, more plastic deformation will lead to an

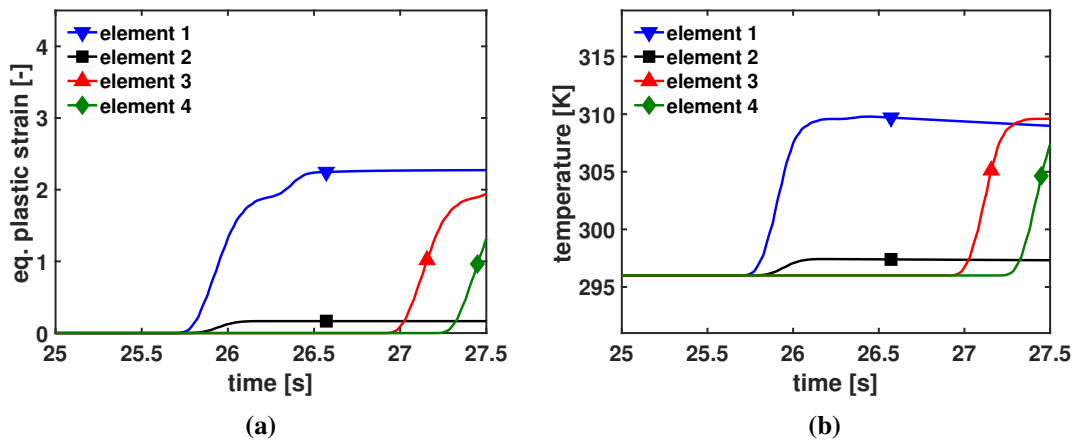


**Figure 3.6:** (a) Plastic deformation of each element, (b) the resulting rise in temperature due to plastic deformation.

increased heat generation. It should be noted however, that we investigate how friction affects heat generation via deformation, and that heat generated due to friction itself is not accounted for in the used coulomb model. In order to investigate the influence of friction quantitatively, two single-asperity scratch simulations are performed. In the first one, the frictionless case is assumed, i.e. friction coefficient  $\mu_f = 0.0$ . In the second simulation a friction coefficient of  $\mu_f = 0.28$  is used. Both simulations are performed using the thermo-mechanical model,  $F_n = 200$  mN, and  $v_s = 100$   $\mu\text{m/s}$ . Element 1 in Figure 3.1b is chosen for this analysis. Frictional scratch leads to polymer-tip sticking, leading to more deformation and a higher deformation rate, see Figure 3.8c. Therefore, more mechanical work is dissipated into heat, increasing the temperature of the polymer, see Figures 3.8a and 3.8b. Figure 3.8d shows the value of the equivalent stress. As mentioned earlier, the equivalent stress is dependent on both deformation rate and temperature. Before any plastic deformation of element 1,  $t = 25$  s till  $t = 25.7$  s, there is no heat generation, and thus, stress is only dependent on deformation rate (elastic) which is lower in the frictionless case, leading to a lower stress level. As plastic deformation takes place,  $t = 25.7$  s till  $t = 26.5$  s, and temperature starts to rise, the stress becomes dependent on both deformation rate and temperature. Finally, when the indenter continues scratching the surface and element 1 stops being deformed,  $t = 26.5$  s till  $t = 27.5$  s, stress becomes only dependent on temperature which is higher when friction is accounted for. Therefore, during this period the resulting equivalent stress from frictional scratch becomes lower than the frictionless case and reaches steady state value as the temperature reaches its steady state value. From Figure 3.8 it is observed that the value of mechanical work dissipated into heat is equal to the product of the equivalent stress and the equivalent

plastic strain-rate multiplied by the percentage of mechanical work dissipated into heat parameter,  $\Gamma$ . This agrees with Equation 3.16.

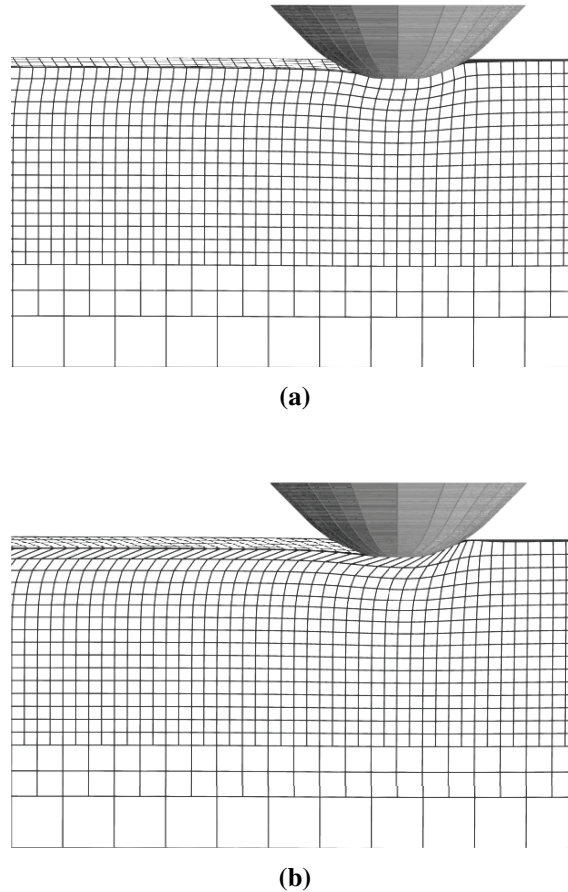


**Figure 3.7:** Single-asperity scratch; (a) using friction coefficient  $\mu_f = 0$ , (b) using friction coefficient  $\mu_f = 0.28$ . Friction implies more polymer-tip adhesion, and thus, elements are more deformed.

### 3.4.3 Analysis of heat generation at various scratch velocities

As shown before, the equivalent plastic strain  $\bar{\gamma}_p$  dictates the trend of temperature evolution. However, the time span in which this plastic strain takes place is critical. In another words, the faster the plastic deformation the higher the amount of mechanical work dissipated into heat according to Equation 3.16. In this respect, we test the influence of scratch velocities on heat generation. Three simulations are performed at  $v_s = 1 \mu\text{m/s}$ ,  $10 \mu\text{m/s}$ , and  $100 \mu\text{m/s}$ . The applied load is  $F_n = 200 \text{ mN}$  and the friction coefficient is  $\mu_f =$

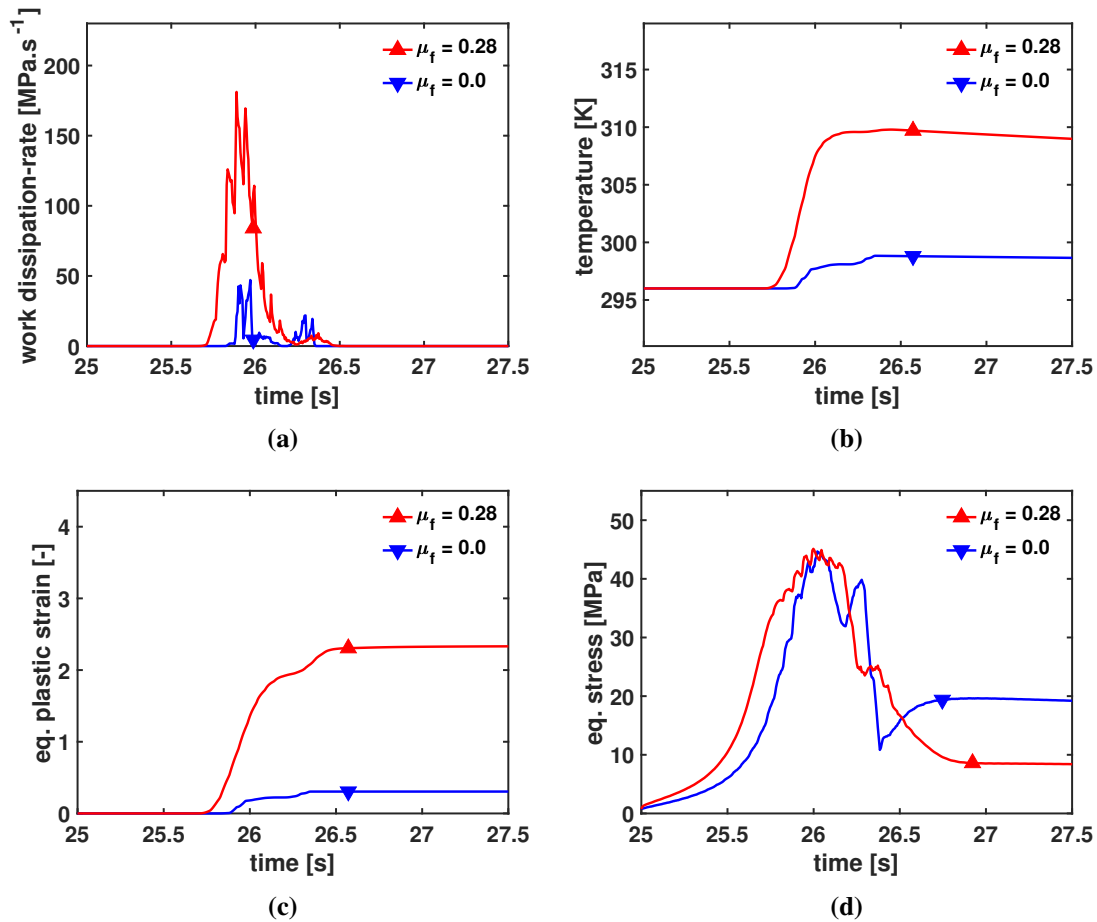


**Figure 3.8:** The effect of friction during scratch simulation and its influence on the deformation kinetics of element 1; (a) rate of mechanical work dissipated into heat, (b) the resulting rise in temperature, (c) the equivalent plastic strain, (d) the equivalent stress.

0.28. The scratch distance is  $250 \mu\text{m}$  for all three simulations. Element 1 from Figure 3.1b is again analysed for the three cases. Figure 3.9a shows the evolution of the equivalent plastic strain along the entire scratch distance. Higher equivalent plastic strain is observed at lower scratch speeds due to the viscoelasticity of the polymer. However, at this lower speed, the time span to complete the entire scratch cycle is one order of magnitude lower than at  $v_s = 10 \mu\text{m/s}$ , and two orders of magnitude lower than at  $v_s = 100 \mu\text{m/s}$ . Thus, the plastic strain-rate is the lowest at this speed, leading to the lowest temperature increase observed, see Figure 3.9b. Since there is enough time for conduction and convection of the generated heat, the temperature goes back to room temperature before the scratch cycle ends. As the scratch speed increases, plastic strain-rate also increases leading to higher maximum temperature generated, as seen in Figure 3.9. It is clear how increasing



the scratch speed by one order of magnitude has a significant effect on the temperature profile along the polymer surface, see Figure 3.10.

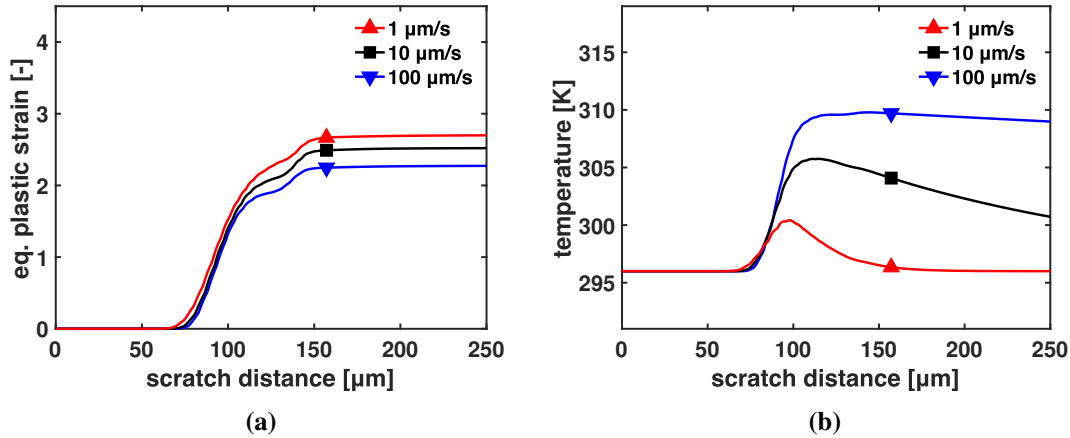


**Figure 3.9:** (a) Plastic deformation of element 1 at  $v_s = 1, 10,$  and  $100 \mu\text{m/s}$  (b) the resulting rise in temperature due to plastic deformation. More plastic deformation at the lowest speed due to the viscoelasticity of the polymer, however, more temperature rise at the highest speed due to higher plastic deformation-rates.

### 3.4.4 Scratch and frictional response of $\alpha$ -iPP and $\beta$ -iPP

Scratch tests are performed at three different scratch velocities;  $v_s = 1 \mu\text{m/s}$ ,  $10 \mu\text{m/s}$ , and  $100 \mu\text{m/s}$ , and at applied normal load  $F_n = 200 \text{ mN}$  on both  $\alpha$ -iPP and  $\beta$ -iPP. Indentation is first performed for 25 s, followed by a constant-speed scratch for 600  $\mu\text{m}$ . The single-asperity scratch response for  $\alpha$ -iPP and  $\beta$ -iPP is shown in Figure 3.11. Figures 3.11a, 3.11b show the value of indenter penetration into the polymer after indentation till it reaches the steady state for  $\alpha$ -iPP and  $\beta$ -iPP respectively. Figures 3.11c and 3.11d display the corresponding frictional response. One observation is the higher bumps in the beginning of the scratch cycle of  $\alpha$ -iPP, which comes from the relatively low strain hardening that allows the tip to initially penetrate deeper before the frictional shear stress pushes the indenter back up and as a result the friction force drops. This observation is even more pronounced at the lowest speed due to the rate dependence of the polymer which allows more initial tip penetration. A second observation is the wavy response in case of  $\alpha$ -iPP which is also related to the relatively low strain hardening that enhances the build-up of the bow wave in front of the tip, resulting in a more abrupt stick-slip cycle. Whereas in case of  $\beta$ -iPP, the higher strain hardening resists the build-up of the bow wave, resulting in a smoother stick-slip cycle. Figure 3.12a presents the values of the steady-state tip penetration into the polymer at each scratch speed. Figure 3.12b displays the

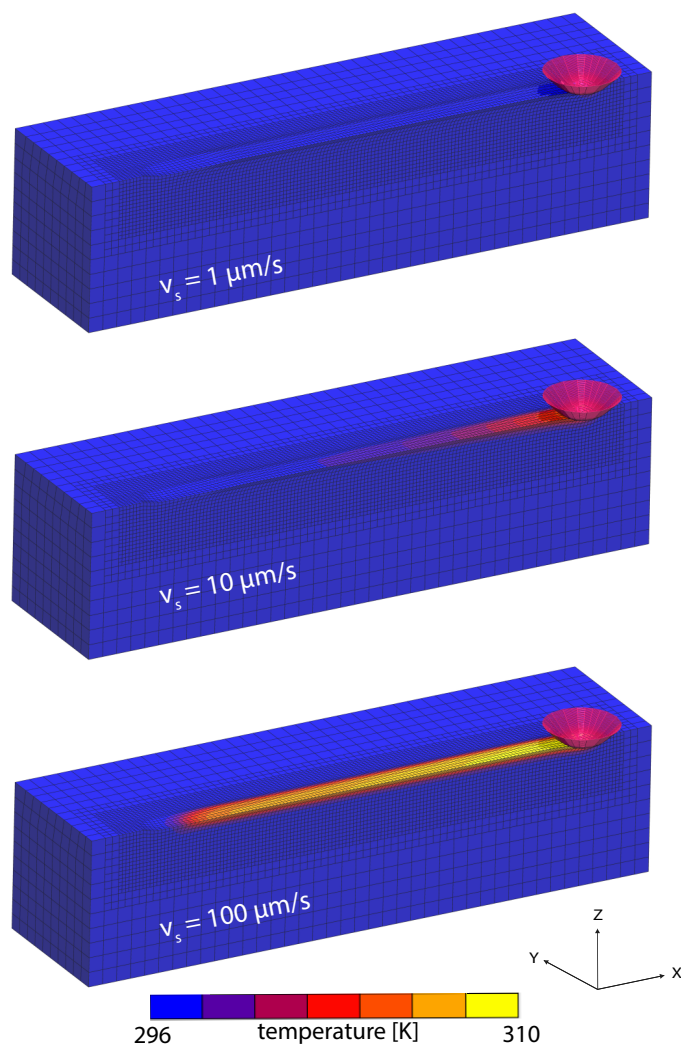


**Figure 3.10:** FEM simulations showing temperature profiles along the surface of the polymer at  $v_s = 1, 10, 100 \mu\text{m/s}$ . At the lowest speed, lower deformation rates result in less temperature rise and more time for heat conduction and convection. The highest speed results in a lot of heat generation due to high plastic deformation-rates and less time for conduction and convection.

corresponding friction force values. The plots show more deformation-rate dependence for  $\beta$ -iPP which resembles its intrinsic response. As the scratch speed increases, the penetration depth and friction force values decrease at higher rate in case of  $\beta$ -iPP. This suggests that, in terms of friction and wear resistance,  $\beta$ -iPP performs better at higher scratch speeds.

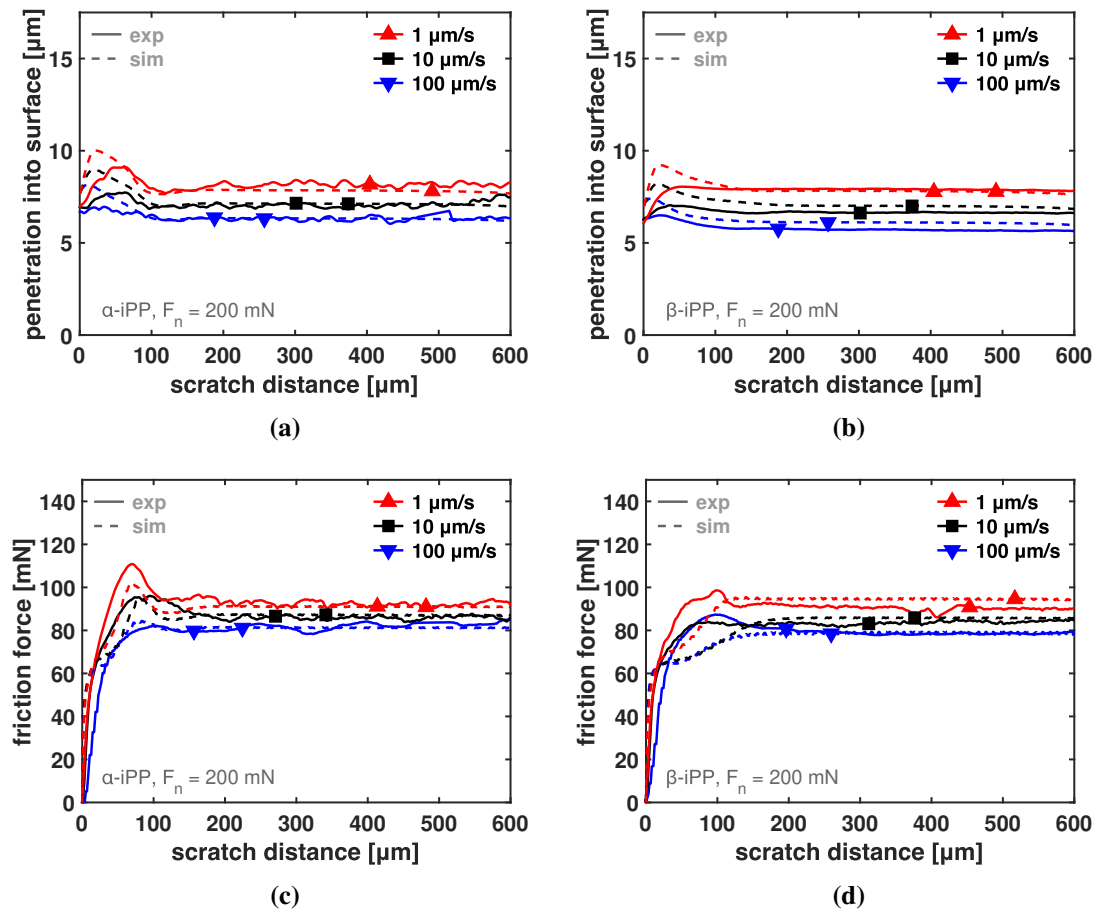


**Figure 3.11:** Single-asperity scratch results of iPP; penetration into the surface versus sliding distance (a)  $\alpha$ -iPP, (b)  $\beta$ -iPP, and friction force versus sliding distance (c)  $\alpha$ -iPP, (d)  $\beta$ -iPP.

### 3.4.5 Damage formation

The intrinsic response of the polymer has a crucial influence on its friction response. In this respect, it is necessary to quantitatively investigate and link between the intrinsic response and the resulting friction response, and come up with a criterion for damage formation (i.e. initiation of wear). It has been reported that the so-called fish-scale damage pattern is the dominant damage mechanism that appears on the surface of polypropylene when scratched. This damage mechanism is controlled by the stick-slip phenomenon which occurs when the indenter experiences periodic change in resistance. This periodic change comes from the periodic build-up of material in front of the tip, which in turn leads to the build-up of friction force to keep the constant velocity of the indenter. When the frictional shear stress is high enough, the indenter is suddenly pushed away,

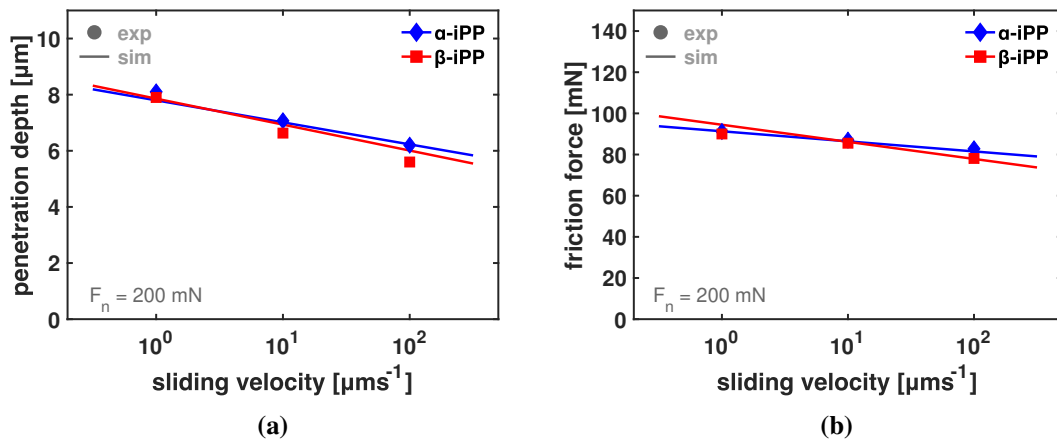


**Figure 3.12:** (a) Steady-state penetration depth values at various scratch speeds, (b) steady-state friction force values at various scratch speeds. Data points are experiments, lines are fitting of simulation data points. The plots show more deformation-rate dependency for  $\beta$ -iPP which resembles its intrinsic response.

and slipping occurs. During the sticking cycle the material is plastically drawn along the scratch direction. This damage mechanism for polypropylene has been reported by many researchers [77–80]. Based on this, we select the equivalent plastic strain  $\bar{\gamma}_p$  as a physical criterion to qualitatively assess and predict the formation of the fish-scale damage pattern. This criterion has been previously used to qualitatively assess damage formation on polymer and metal surfaces [31, 89].

First, we are interested in investigating the influence of boundary conditions, i.e. normal load and scratch speed on damage formation. Figure 3.13a shows the polymer surface of  $\alpha$ -iPP after single-asperity scratch at various normal loads. At higher applied normal load, the tip penetrates more into the surface, creating more material build-up in front of the tip, making the stick-slip more abrupt and severe. This leads to material being more plastically drawn along the scratch direction. Figure 3.13b displays the simulation results, in which the equivalent plastic strain  $\bar{\gamma}_p$  contour profile is shown. Due to the increased normal load, more material is plastically deformed giving rise to the equivalent plastic strain. This is confirmed from the values of the width of the scratch which are quantitatively comparable to the experimental values.

Due to rate dependency of the polymer, lowering scratch speed has an effect on the scratch response similar to that of a higher applied normal load. As scratch speed decreases, the indenter penetrates more into the polymer creating a more abrupt stick-slip cycles in which material experiences more plastic deformation, see Figure 3.14.

The intrinsic response of the polymer is a critical factor, and plays a decisive role in its damage formation mechanism. Figure 3.15a shows the polymer surface of  $\alpha$ -iPP

and  $\beta$ -iPP after single-asperity scratch. Fish-scale damage pattern is clearly visible in case of  $\alpha$ -iPP. Simulation results, Figure 3.15b, show that the maximum value of  $\bar{\gamma}_p$  is significantly higher in case of  $\alpha$ -iPP although penetration depth and friction force values at this speed are almost identical. However, looking at the intrinsic response of both phases, Figure 3.15c, a significant difference in strain hardening is observed. Strain hardening is believed to be the reason behind damage formation differences between the two phases. A material with low strain hardening experiences more localized plastic deformation, and more material build-up, creating a more severe stick-slip cycle, leading to higher plastic deformation and fish-scale damage pattern becoming more visible.

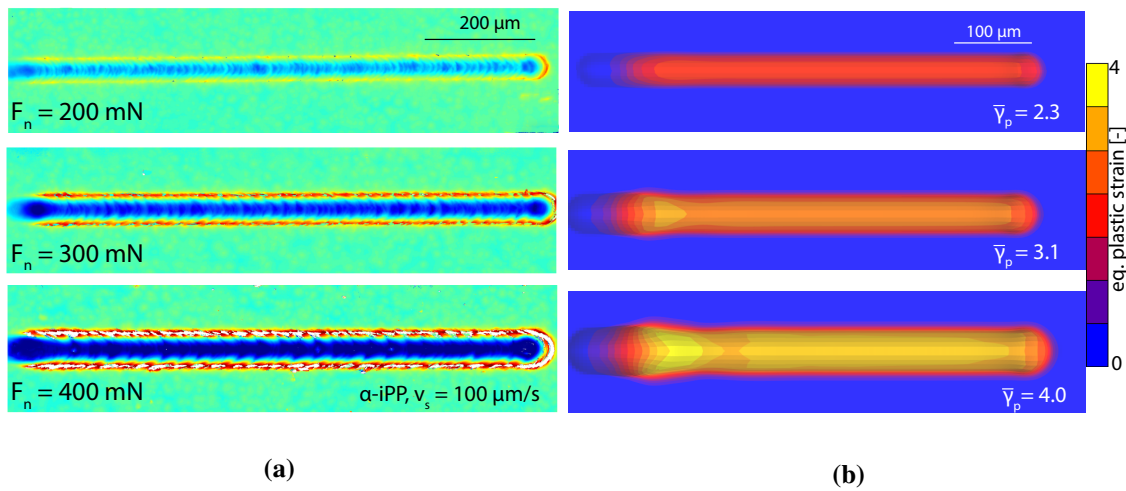


**Figure 3.13:** Polymer surface of  $\alpha$ -iPP after single-asperity scratch at various normal loads; (a) experimental, (b) simulations showing maximum value of  $\bar{\gamma}_p$ . Wider scratch profile appears at high normal loads. Higher equivalent plastic strain  $\bar{\gamma}_p$  in simulations at high normal loads resembles the appearance of fish-scale damage pattern in experiments at these loads.

Due to the crystalline nature of iPP and other semi-crystalline polymers, material orientation has an effect on its intrinsic response [67, 90]. During scratch, the material is oriented along the scratch direction. It is possible that the resulting material orientation has a critical role in damage formation. To test this hypothesis, the three principle strains of element 1 from Figure 3.1b are obtained during scratching at a speed of  $1 \mu\text{m/s}$  and  $100 \mu\text{m/s}$ , see Figure 3.16. Their values are comparable to the values of equivalent plastic strain  $\bar{\gamma}_p$  in Figure 3.14b. The equivalent plastic strain is only a summation of the magnitude of the plastic part of all principle strains. Scratching at  $1 \mu\text{m/s}$  results in a 10% increase in all three principle directions when compared to scratching at  $100 \mu\text{m/s}$ . Previous studies have shown that orientation, i.e. pre-stretch, results in less scratch depth and friction force and reduced damage [73, 91]. However, in our case,

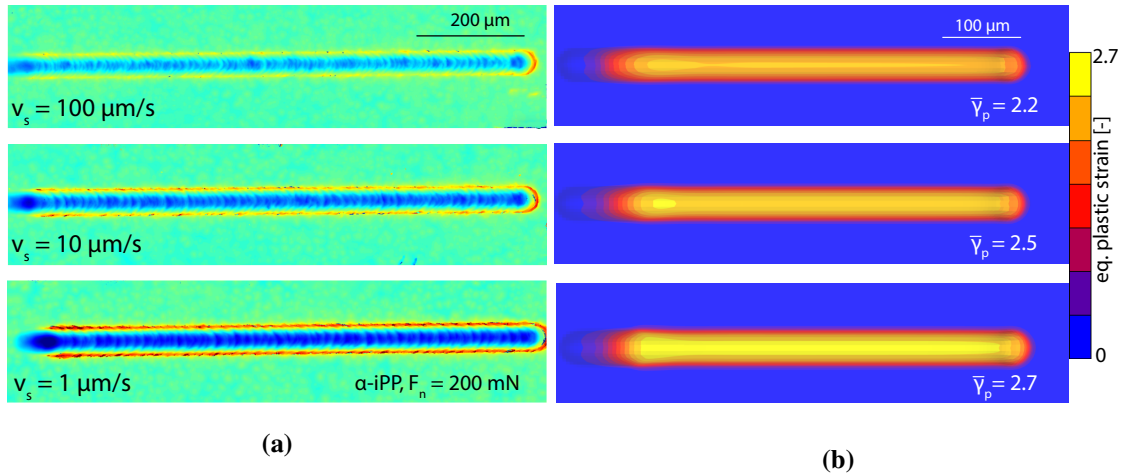


**Figure 3.14:** Polymer surface of  $\alpha$ -iPP after single-asperity scratch at various scratch speeds; (a) experimental, (b) simulations showing maximum value of  $\bar{\gamma}_p$ . Higher equivalent plastic strain  $\bar{\gamma}_p$  appears in simulations at lower speeds due to the rate dependency of polymers. This explains the formation of fish-scale damage pattern at these speeds in experiments.

the lowest scratch speed results in the highest penetration depth and friction force which leads to more apparent damage. This suggests that the viscoelasticity of the material, and not orientation, is the decisive factor in damage formation when comparing the scratch response at different scratch speeds. Similar observations hold when comparing different loads and phases. Although the current model does not account for material anisotropy, it is plausible for future work to include it in order to quantitatively investigate its effect on the scratch and frictional response. Senden et al. [90] used a 3D viscoelastic model based on Hill theory in order to predict the yield of drawn polypropylene tapes at various orientation angles with respect to the drawing direction. It is possible to simulate single-asperity scratch of an anisotropic polypropylene surface by implementing such a model in FEM.

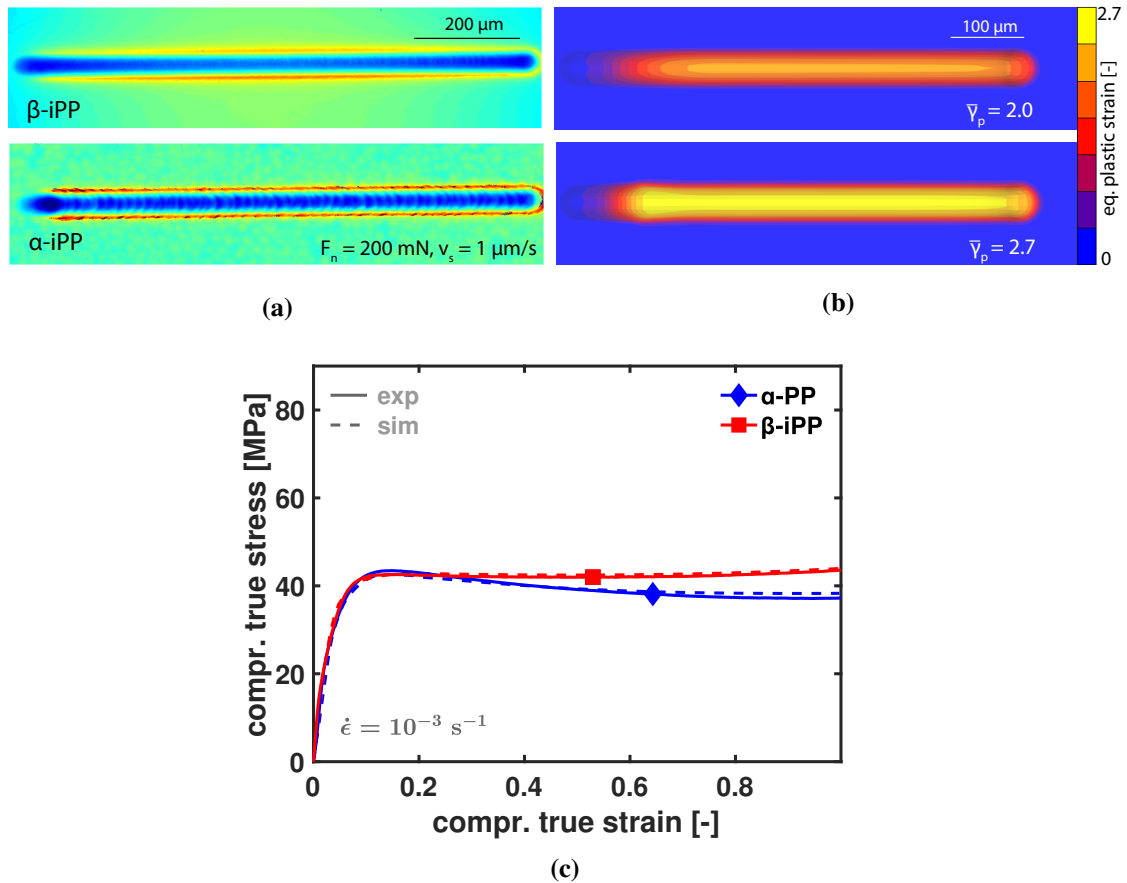


**Figure 3.15:** Polymer surface of  $\alpha$ -iPP and  $\beta$ -iPP after single-asperity scratch; (a) experimental, (b) simulations showing maximum value of  $\bar{\gamma}_p$ . Fish-scale damage pattern is clearly visible in case of  $\alpha$ -iPP, and simulation results show higher equivalent plastic strain  $\bar{\gamma}_p$  for  $\alpha$ -iPP. (c) Intrinsic response of  $\alpha$ -iPP and  $\beta$ -iPP show a significant difference in strain hardening, which is believed to be reason behind the damage formation differences between the two phases.

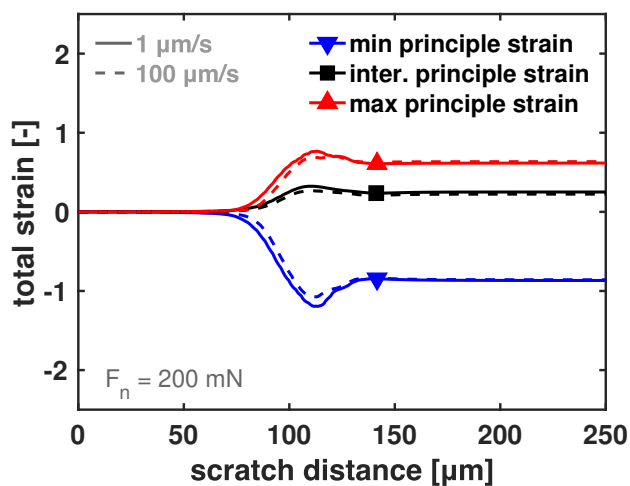


**Figure 3.16:** The three principle strains of element 1 during scratching at a speed of 1 μm/s and 100 μm/s. Small difference in element stretching suggests that material orientation is not a critical factor in damage formation.



### 3.5 Conclusions

A 3D elasto-viscoplastic constitutive model has been implemented in a FEM-framework to simulate a single-asperity scratch of two morphological structures;  $\alpha$ - and  $\beta$ -iPP at different normal loads and scratch velocities. The physics-based thermo-mechanical model along with the experimental work formed the base of a hybrid experimental-numerical approach that was used to investigate the polymer scratch and frictional response based on its intrinsic response. From this study we conclude that:

1. The thermo-mechanical model is necessary to quantitatively predict the intrinsic response of the material especially at higher strain rates where heat is produced due the plastic deformation.
2. At higher scratch velocities, the polymer becomes more resistant to deformation due to its strain-rate dependence. This results in a lower scratch depth and friction force.
3. The intrinsic response of  $\alpha$ - and  $\beta$ -iPP shows similar yield-stress levels. However,  $\beta$ -iPP exhibits a slightly higher strain-rate dependence. The comparable yield stress levels result in similar scratch and friction force values at lower scratch velocities. However, as the scratch velocities increase, the values of the penetration depths and friction force decrease in both cases but with a higher slope in case of  $\beta$ -iPP due to its higher sensitivity to deformation rates.  $\beta$ -iPP exhibits a slightly higher strain-rate dependence than  $\alpha$ -iPP. This leads to lower penetration depth and friction force at relatively high deformation rates. In this respect,  $\beta$ -iPP is a good choice for high-speed applications due to its more pronounced strain-rate dependence.
4. The stick-slip phenomenon is mainly responsible for the damage mechanism observed. During the sticking cycle the material is plastically drawn along the scratch direction creating the damage pattern. For this reason, the equivalent plastic strain  $\bar{\gamma}_p$  has been chosen as a physical criterion to qualitatively assess and predict the formation of the fish-scale damage pattern.
5. The stick-slip phenomenon becomes more pronounced when the tip penetrates deep into the polymer, which introduces additional material build-up in front of the tip. A high normal load and low scratch speed lead to more tip penetration, thus, stick-slip becomes more severe. The material is more plastically deformed along the scratch direction and the fish-scale damage pattern is clearly observed.
6. A significant intrinsic difference between  $\alpha$ -iPP and  $\beta$ -iPP is the strain hardening. In case of  $\beta$ -iPP the higher strain hardening resists the build-up of the bow wave in front of the tip resulting in less sticking and more slipping. Less material is plastically drawn along the scratch direction, preventing the formation of the fish-scale damage pattern. This makes  $\beta$ -iPP, again, a favourable choice over  $\alpha$ -iPP for applications that require wear resistance.
7. Material orientation, i.e. pre-stretch, results in less scratch depth and friction force and

---

reduces damage [73,91]. At the lowest scratch speed, material is stretched slightly higher than at the highest one. However, penetration depth and friction force are higher, and damage is more apparent, suggesting that the slight difference in stretch does not play a role in damage formation. Similarly, when comparing different loads and phases the same conclusion holds. The induced material orientation due to scratching is relatively low and does not have a significant role in damage formation.



# Chapter 4

## Uniaxial and biaxial response of anisotropic polypropylene

### Abstract

The response of uniaxial and biaxial anisotropic polypropylene is discussed. A 3D elasto-viscoplastic constitutive model is developed to account for material anisotropy. The famous Hill's anisotropic yield criterion is combined with the Eyring relation and implemented in a finite element framework to model the response of the polymer during uniaxial loading. An associated viscoplastic flow rule that describes the magnitude and the direction of the viscoplastic flow is incorporated in the model to simulate complex loading conditions. The model quantitatively captures the yield stresses for uniaxial deformation at a given anisotropic state and material orientation. In addition, the results of simulations demonstrate that the constitutive relations qualitatively describe the material deformation during biaxial loading for both isotropic and anisotropic cases.

## 4.1 Introduction

High-performance polymers are nowadays favoured over traditional materials because of their strength-to-weight ratio and excellent mechanical properties. The mechanical properties of polymers mainly depend on material-related parameters and processing-related conditions. Example of the former is molecular weight, and of the latter is flow and temperature. Semi-crystalline polymers such as polypropylene and polyethylene are highly affected by processing conditions due their crystalline structure. Upon forming processes, crystals are oriented towards the flow direction. This has been observed in many manufacturing processes such as drawing, extrusion, and rolling [92–95], resulting in significant mechanical anisotropy, i.e. yielding and failure behaviour are anisotropic. An implication of such behaviour is a significant change in the tensile stress of polymer samples cut at different angles with respect to their orientation direction [96–101].

The pioneering work of Tresca and Von Mises [102, 103] aimed to model the plastic yielding of isotropic materials. However, these classical theories did not account for rate, temperature, and pressure dependencies. Nevertheless, several 3D viscoelastic models have been developed based on the two pioneering yielding theories. These models were able to include rate, temperature, and pressure dependencies of a glassy polymer [37, 104]. Hill was the first to consider rate-independent anisotropic yielding [105, 106], his theory is the most commonly used yielding criterion for anisotropic materials. Van Erp et al. [67] used a 3D viscoelastic model based on Hill's theory in order to predict the yield of drawn polypropylene tapes at various orientation angles and draw ratios with respect to the drawing direction. Senden et al. [90] extended this model to capture the asymmetry between the tensile and compressive response of injection-moulded polyethylene. Hill's yielding criterion is sufficient to capture the yield values of anisotropic material during uniaxial deformation. However, the criterion is still necessary but not sufficient in case of biaxial loading. In this respect, an associated viscoplastic flow rule is needed to determine the direction and magnitude of plastic deformation at any given stress and anisotropic state [67, 90, 107, 108].

In the present work it is attempted to model the response of an anisotropic polymer during uniaxial and biaxial tensile loading. The model accounts for rate, temperature, and pressure dependencies of the polymer and is tested over a range of orientation angles and draw ratios. Polypropylene (PP), which has well-defined mechanical properties [42, 67, 69–71, 108], is selected as a material model since it is one of the most widely used semi-crystalline polymers. Depending on application, polypropylene exhibits an anisotropic response as a result of processing conditions [108]. The constitutive model

used is a 3D elasto-viscoplastic model based on the Eindhoven Glassy Polymer (EGP) model [38, 39, 43], in which non-linear viscoelasticity and thermo-rheological complex responses are taken into account [37, 40, 56]. In the current study, this model is extended to account for anisotropy by incorporating Hill's yielding criterion and an associated viscoplastic flow rule. The motivation for this work is the need for an elasto-viscoplastic model which can be used as a tool to simulate the response of anisotropic polymers during complex loading cases such as indentation or scratch testing. The model is implemented in FEM-framework and is used to simulate uniaxial and biaxial tensile tests at different orientation angles and stretch ratios.

## 4.2 Materials and Methods

Single-element uniaxial tensile simulations are performed using one linear quad4 axisymmetric element. Moreover, 3D uniaxial and biaxial tensile simulations are performed using linear hex8 3D elements. The 3D simulations model only one-eighth of an actual sample with the proper boundary conditions applied in order to save computational time. All simulations are performed using the finite element package MSC.Marc. The constitutive model is implemented via the user subroutine HYPELA2. The uniaxial tensile simulations are validated via experimental results obtained from Van Erp et al. [67]. The material used for the tensile tests is isotactic polypropylene. In these experiments, tapes were drawn at draw ratios of  $\lambda = 1, 4,$  and  $6$ . Tensile samples were then cut from these tapes at different orientation angles with respect to the drawing direction  $\theta$ , ranging from  $0^\circ$  till  $90^\circ$ , see Figure 4.1. Detailed information about material and sample preparation is found in [67].

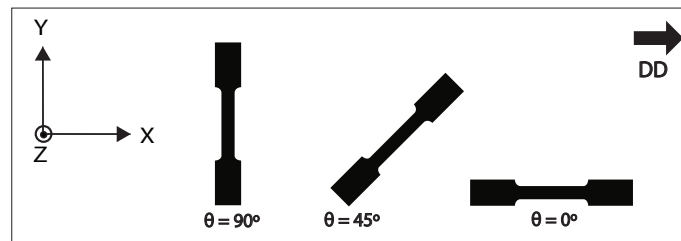


**Figure 4.1:** Tensile samples cut at different orientations with respect to the drawing direction.

### 4.3 Constitutive Modelling

This section explains the 3D elasto-viscoplastic constitutive model used and the incorporation of Hill yielding function. This is combination of similar models published elsewhere [40, 67, 90].

#### 4.3.1 Kinematics

The deformation gradient tensor  $\mathbf{F}$  is decomposed into elastic and plastic parts:

$$\mathbf{F} = \mathbf{F}_e \cdot \mathbf{F}_p. \quad (4.1)$$

The plastic velocity gradient tensor  $\mathbf{L}_p$  is defined as follow:

$$\mathbf{L}_p = \dot{\mathbf{F}}_p \cdot \mathbf{F}_p^{-1} = \mathbf{D}_p + \mathbf{\Omega}_p, \quad (4.2)$$

where,  $\mathbf{D}_p$  is the plastic deformation-rate tensor and  $\mathbf{\Omega}_p$  is the plastic-spin tensor. Plastic deformation is assumed to be spin free [109], which leads to:

$$\mathbf{L}_p = \dot{\mathbf{F}}_p \cdot \mathbf{F}_p^{-1} = \mathbf{D}_p. \quad (4.3)$$

The volume change ratio  $J$  is the determinant of the elastic deformation-gradient tensor, since plastic deformation is isochoric:

$$J = \det(\mathbf{F}) = \det(\mathbf{F}_e). \quad (4.4)$$

#### 4.3.2 Stress calculation

The total stress  $\boldsymbol{\sigma}$  is the sum of the driving  $\boldsymbol{\sigma}_s$  and the hardening stress  $\boldsymbol{\sigma}_r$ :

$$\boldsymbol{\sigma} = \boldsymbol{\sigma}_s + \boldsymbol{\sigma}_r. \quad (4.5)$$

The hardening stress represents the rubber elastic contribution of the entangled network. Mathematically, it is described with a simple neo-Hookean rubber-elastic model:

$$\boldsymbol{\sigma}_r = \frac{G_r}{J} \tilde{\mathbf{B}}^d, \quad (4.6)$$

herein,  $G_r$  denotes the hardening modulus,  $\tilde{\mathbf{B}}^d$  is the deviatoric part of the isochoric left Cauchy-Green strain tensor, and  $J$  is the volume change ratio. The driving stress

is represented by multiple Maxwell elements connected in parallel. It is split into a hydrostatic  $\sigma_s^h$  and a deviatoric part  $\sigma_s^d$ :

$$\sigma_s = \sigma_s^h + \sigma_s^d = \kappa(J - 1)\mathbf{I} + \sum_{i=1}^n G_i \tilde{\mathbf{B}}_{e,i}^d, \quad (4.7)$$

where,  $\kappa$  is the bulk modulus,  $G$  is the shear modulus,  $\tilde{\mathbf{B}}_e^d$  is the elastic deviatoric part of the isochoric left Cauchy-Green strain tensor, and subscript  $i$  refers to a specific mode.

### 4.3.3 Extension to thermo-rheologically complex behaviour

Polypropylene is proven to exhibit secondary molecular process as it has been tested over broad range of strain rates [56], i.e. thermo-rheologically complex behaviour. To capture this complex behaviour we use a straightforward extension of Equation 4.5 based on Ree-Eyring's theory [84]:

$$\sigma = \sigma_{s,1} + \sigma_{s,2} + \sigma_r, \quad (4.8)$$

where  $\sigma_{s,1}$  is the driving stress of the primary process ( $\sigma_s$  in Equation 4.7), and  $\sigma_{s,2}$  is the driving stress for the secondary process. Each process has its own characteristic values of the activation volume  $V^*$  and activation energy  $\Delta U$ .

### 4.3.4 Hill's yield function

The Hill function is the most commonly used yielding criterion for anisotropic materials. It provides the most accurate prediction of tensile yield stress of oriented polymers at various loading angles [67, 90, 97, 100, 110, 111]. Hill equivalent stress  $\bar{\sigma}_H$  is determined as follows:

$$\bar{\sigma}_H^2 = F(\sigma_{22} - \sigma_{33})^2 + G(\sigma_{33} - \sigma_{11})^2 + H(\sigma_{11} - \sigma_{22})^2 + \dots \\ 2L\sigma_{23}^2 + 2M\sigma_{13}^2 + 2N\sigma_{12}^2, \quad (4.9)$$

$$F = \frac{1}{2} \left( \frac{1}{R_{22}^2} + \frac{1}{R_{33}^2} - \frac{1}{R_{11}^2} \right); \quad L = \frac{3}{2R_{23}^2}; \quad (4.10)$$

$$G = \frac{1}{2} \left( \frac{1}{R_{11}^2} + \frac{1}{R_{33}^2} - \frac{1}{R_{22}^2} \right); \quad M = \frac{3}{2R_{13}^2}; \quad (4.11)$$



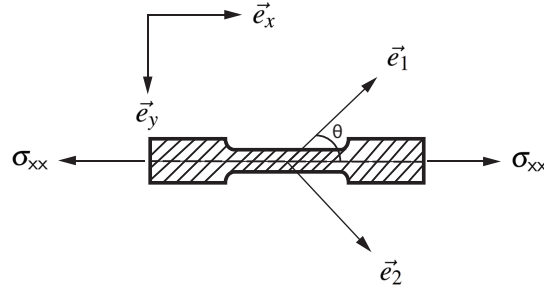


**Figure 4.2:** Material and global coordinate system of the tensile sample. The angle  $\theta$  represents the angle at which the sample is cut with respect to the drawing direction.

$$H = \frac{1}{2} \left( \frac{1}{R_{11}^2} + \frac{1}{R_{22}^2} - \frac{1}{R_{33}^2} \right); \quad N = \frac{3}{2R_{12}^2}, \quad (4.12)$$

where  $\sigma_{ij}$  are the stress components with respect to the material coordinate system, see Figure 4.2,  $R_{ij}$  represent the ratio of the yield stress in the corresponding material direction to the isotropic reference yield stress. Three normal parameters ( $R_{11}$ ,  $R_{22}$ ,  $R_{33}$ ) and three shear parameters ( $R_{12}$ ,  $R_{13}$ ,  $R_{23}$ ) are used to quantify the orthogonal anisotropic plasticity. One of the main aspects of this study is to investigate the effect of sample orientation with respect to drawing direction. If material coordinates do not coincide with global coordinates, Figure 4.2, an extended version of Hill function based on stress and orientation is used similar to [90]. To formulate the extended version, first, the vectors  $\vec{e}_1, \vec{e}_2, \vec{e}_3$  are defined as the orthogonal vectors which coincide with the material axes:

$$\vec{e}_1 = \begin{Bmatrix} \cos\theta \\ \sin\theta \\ 0 \end{Bmatrix}; \quad \vec{e}_2 = \begin{Bmatrix} -\sin\theta \\ \cos\theta \\ 0 \end{Bmatrix}, \quad (4.13)$$

vector  $\vec{e}_3$  is always perpendicular to the plane of the sample, so it can be ignored. Tensors  $\mathbf{R}_1$  and  $\mathbf{R}_2$  are orientation tensors that define the state of anisotropy:

$$\mathbf{R}_1 = \vec{e}_1 \vec{e}_1; \quad \mathbf{R}_2 = \vec{e}_2 \vec{e}_2. \quad (4.14)$$

Given the anisotropic parameters  $R_{ij}$ , and the orientation tensors  $\mathbf{R}_1$  and  $\mathbf{R}_2$ , the extended invariant form of Hill function is given by:

$$\begin{aligned} \bar{\sigma}_H = & \left[ (L + M - N)\text{tr}(\boldsymbol{\sigma}_s^d \cdot \boldsymbol{\sigma}_s^d) + (F + 4G + H - 2M)\text{tr}^2(\boldsymbol{\sigma}_s^d \cdot \mathbf{R}_1) + (-2L + 2N)\dots \right. \\ & \text{tr}(\boldsymbol{\sigma}_s^d \cdot \mathbf{R}_1 \cdot \boldsymbol{\sigma}_s^d) + (4F + G + H - 2L)\text{tr}^2(\boldsymbol{\sigma}_s^d \cdot \mathbf{R}_2) + (-2M + 2N)\text{tr}(\boldsymbol{\sigma}_s^d \cdot \mathbf{R}_2 \cdot \boldsymbol{\sigma}_s^d) + \dots \\ & \left. (4F + 4G - 2H - 2L - 2M + 2N)\text{tr}(\boldsymbol{\sigma}_s^d \cdot \mathbf{R}_1)\text{tr}(\boldsymbol{\sigma}_s^d \cdot \mathbf{R}_2) \right]^{1/2}. \quad (4.15) \end{aligned}$$

The same relation can be further simplified:

$$\bar{\sigma}_H = \sqrt{\boldsymbol{\sigma}_s^d : {}^4\mathbf{H} : \boldsymbol{\sigma}_s^d}, \quad (4.16)$$

where  ${}^4\mathbf{H}$  is Hill's fourth order anisotropy tensor. This tensor is a function of the anisotropic parameters  $R_{ij}$  and the orientation angle  $\theta$ . In the isotropic case, i.e.  $R_{ij} = 1$ , or when the sample is cut perpendicular to the drawing direction, i.e.  $\theta = 90^\circ$ , the Hill fourth order tensor reduces to  ${}^4\mathbf{H} = \frac{3}{2} {}^4\mathbf{I}$  leading to:

$$\bar{\sigma}_H = \sqrt{\frac{3}{2} \boldsymbol{\sigma}_s^d : \boldsymbol{\sigma}_s^d}, \quad (4.17)$$

which is how the equivalent stress is determined using a non-directional yielding criterion, i.e. Von Mises.

### 4.3.5 Viscoplastic flow

The equivalent plastic strain-rate  $\dot{\epsilon}_p$  is determined using the pressure-modified Eyring flow rule [82, 83, 112]:

$$\dot{\epsilon}_p = \dot{\epsilon}_0 \sinh \left[ \frac{\bar{\sigma}_H V^*}{k_b T} \right] \exp \left[ - \frac{\mu p V^*}{k_b T} \right] \exp \left[ \frac{\Delta U}{RT} \left( \frac{T - T_{\text{ref}}}{T_{\text{ref}}} \right) \right], \quad (4.18)$$

where  $\dot{\epsilon}_0$  is a rate constant,  $p$  is the hydrostatic pressure, the parameter  $\mu$  defines the pressure dependency,  $k_b$  is the Boltzmann's constant and  $V^*$  is the activation volume. The last pre-exponential factor is a temperature-dependent shift factor described by an Arrhenius relation, where  $\Delta U$  is the activation energy,  $R$  is the universal gas constant,  $T$  represents the absolute temperature, and  $T_{\text{ref}}$  is the reference temperature. Dividing stress by strain rate and taking the thermo-mechanical history into account similar to [39], the Eyring relation can be expressed in terms of viscosity  $\eta_i$  for each Maxwell element as

follows:

$$\eta_i = \eta_{0,\text{ref},i} \frac{\bar{\tau}_H/\tau_0}{\sinh(\bar{\tau}_H/\tau_0)} \exp\left[\frac{\mu p}{\tau_0}\right] \exp\left[-\frac{\Delta U}{RT} \left(\frac{T - T_{\text{ref}}}{T_{\text{ref}}}\right)\right] \exp[S_a R_x(\bar{\gamma}_p)], \quad (4.19)$$

with,

$$\tau_0 = \frac{k_b T}{V_*}, \quad (4.20)$$

where  $\tau_0$  defines the characteristic shear stress, the equivalent shear stress  $\bar{\tau}_H = \bar{\sigma}_H/\sqrt{3}$ , subscript  $i$  refers to specific element,  $\eta_{0,\text{ref},i}$  is the reference viscosity of the element. The thermo-mechanical history is contained in last pre-exponential factor. The physical ageing is described by the state parameter  $S_a$ , the softening function  $R_x(\bar{\gamma}_p)$  describes the strain-softening process, i.e. the erasure of thermal history upon the inception of plastic deformation. Klompen et al. [43] expressed  $R_x(\bar{\gamma}_p)$  as a function of  $\bar{\gamma}_p$  using a modified Carreau-Yasuda relation:

$$R_x(\bar{\gamma}_p) = \left[ \frac{1 + (r_0 \cdot \exp(\bar{\gamma}_p))^{r_1}}{1 + r_0^{r_1}} \right]^{(r_2-1)/r_1}, \quad (4.21)$$

where  $\bar{\gamma}_p$  is the equivalent plastic strain, and  $r_0$ ,  $r_1$ , and  $r_2$  are the fitting parameters. The plastic deformation-rate tensor is given by:

$$\mathbf{D}_p = \dot{\bar{\epsilon}}_p \mathbf{N}, \quad (4.22)$$

where  $\dot{\bar{\epsilon}}_p$  represents the magnitude of the plastic deformation-rate. The tensor  $\mathbf{N}$  determines the direction of viscoplastic flow, and is given by:

$$\mathbf{N} = \frac{1}{\bar{\sigma}_H} ({}^4\mathbf{H} : \boldsymbol{\sigma}_s^d). \quad (4.23)$$

### 4.3.6 Implementation

The right Cauchy-Green deformation tensor  $\mathbf{C}_p$  is defined as:

$$\mathbf{C}_p = \mathbf{F}_p^T \cdot \mathbf{F}_p, \quad (4.24)$$

By taking the derivative of  $\mathbf{C}_p$  and making use of Equations 4.1 and 4.3, the evolution of  $\mathbf{C}_p$  is given by:

$$\dot{\mathbf{C}}_p = 2\mathbf{F}^T \cdot \mathbf{F}_e^{-T} \cdot \mathbf{D}_p \cdot \mathbf{F}_e^{-1} \cdot \mathbf{F}. \quad (4.25)$$

An explicit Euler scheme is used for the numerical integration to solve the right Cauchy-Green deformation tensor  $C_p$ :

$$C_{p_{n+1}} = C_{p_n} + \delta t \dot{C}_{p_{n+1}}, \quad (4.26)$$

where the subscripts  $n$  and  $n+1$  refer to the current and the next increment. After  $C_p$  is solved using a forward Euler method, the left Cauchy-Green deformation tensor is determined as follows:

$$B_e = F \cdot C_p^{-1} \cdot F^T. \quad (4.27)$$

## 4.4 Simulations and model characterization

### 4.4.1 Uniaxial loading

Single-element FEM compression and tensile simulations are performed by implementing the constitutive model in the material subroutine HYPELA2 within the FEM package MSC.Marc. Compression simulations, representing the intrinsic material response, are performed at strain rates ranging from  $10^{-5}$  till  $10^{-2} \text{ s}^{-1}$ . The simulation results are then fitted to experimental data of PP obtained from [71], see Figure 4.3. The resulting reference spectrum of PP is shown in Table 4.1. The activation volume  $V^*$  is a measure of the strain-rate sensitivity. The pressure dependency parameter  $\mu$  is determined from the compressive and tensile data obtained from [70, 71]. The rest of the material parameters are obtained from [56] and tabulated along with  $V^*$  and  $\mu$  in Table 4.2 and 4.3.

After the model parameters are obtained, tensile simulations are performed at different stretch ratios  $\lambda$  and orientation angles  $\theta$ . The values of the anisotropic parameters are determined in a way similar to Van Erp et al. [67]. The anisotropic parameters  $R_{ij}$  defines the state of anisotropy at a specific stretch ratio. When material is isotropic, i.e.  $\lambda = 1$ , all the six anisotropic parameters  $R_{ij} = 1$ . However, at increasing drawing ratios these parameters increase as well. The anisotropic parameters represent the ratio of the actual yield strength of the anisotropic material to the reference yield strength, i.e. isotropic case. As shown in Figure 4.2 the material direction  $\vec{e}_1$  corresponds with the drawing direction and is perpendicular to  $\vec{e}_2$  while the third direction is out-of-plane. Two assumptions are made, transverse isotropy, i.e.  $R_{22} = R_{33}$ , and plane stress. This means only three parameters are needed;  $R_{11}$ ,  $R_{22}$ , and  $R_{12}$ . Normally  $R_{11}$ ,  $R_{22}$  are directly obtained from Equations 4.9-4.12. For  $\mu \neq 0$ , the anisotropic parameters values have to be adjusted. First, the equivalent stress  $\bar{\sigma}_H$  in the Eyring relation, Equation 4.18, is much higher than the characteristic stress at yield;  $\bar{\sigma}_H \gg kT/V^*$ , and if  $\mu = 0$ , this leads to the Eyring

**Table 4.1:** Reference spectrum of PP.

Process 1	Mode	$\eta_{0,i,\text{ref}}$ [MPa.s]	$G_i$ [MPa]
	1	$1.6 \times 10^8$	110
	2	$3.5 \times 10^7$	90
	3	$2.3 \times 10^6$	70
	4	$3.3 \times 10^5$	60
	5	$3.3 \times 10^4$	40
	6	$6.7 \times 10^3$	30
Process 2	Mode	$\eta_{0,i,\text{ref}}$ [MPa.s]	$G_i$ [MPa]
	1	$2.4 \times 10^{-2}$	80

**Table 4.2:** Material parameters of PP [56].

$G_r$ [MPa]	$\kappa$ [MPa]	$\mu$ [-]	$V_1^*$ [nm <sup>3</sup> ]	$V_2^*$ [nm <sup>3</sup> ]	$\Delta U_1$ [kJ/mole]	$\Delta U_2$ [kJ/mole]
1.6	1650	0.12	3.10	3.0	274	251

**Table 4.3:** Ageing and softening parameters of PP [56].

$S_a$ [-]	$r_0$ [-]	$r_1$ [-]	$r_2$ [-]
5.0	0.95	2.0	-0.5

equation being reduced to:

$$\bar{\sigma}_H = \frac{kT}{V^*} \ln \left( 2 \frac{\dot{\epsilon}_p}{\dot{\epsilon}_0} \right). \quad (4.28)$$

The equivalent stress for a uniaxial case is related to the applied stress by the following relation:

$$\bar{\sigma}_H^2 = g^2(R_{ij}, \theta) \sigma_{xx}^2, \quad (4.29)$$

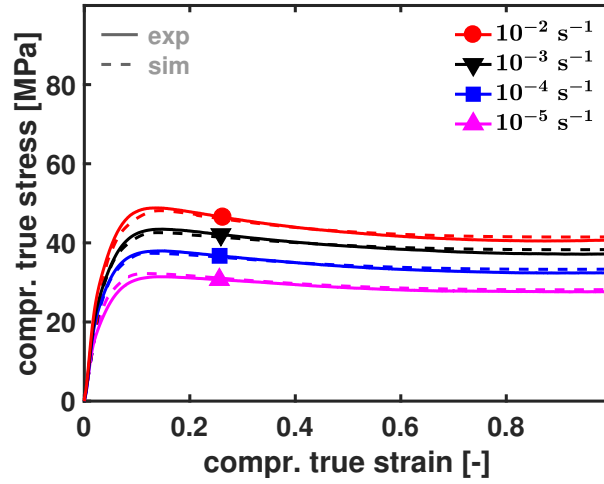


**Figure 4.3:** Fitting uniaxial single-element compression simulation results to experimental data [71]. Higher yield values obtained as the strain rate increases.

where the function  $g(R_{ij}, \theta)$  is a multiplier function of the yield stress. It is a function of anisotropy and orientation, for a uniaxial case it is given by:

$$g(R_{ij}, \theta) = \sqrt{(G + H)\cos^4(\theta) + (F + H)\sin^4(\theta) + 2(N - H)\cos^2(\theta)\sin^2(\theta)}, \quad (4.30)$$

substituting Equation 4.29 in Equation 4.28 yields:

$$\sigma_{xx} = \frac{kT}{V^*} \ln \left( 2 \frac{\dot{\epsilon}_p}{\dot{\epsilon}_0} \right) \frac{1}{g(R_{ij}, \theta)}, \quad (4.31)$$

when the angle  $\theta = 0^\circ$  in Equation 4.30, Equation 4.31 yields:

$$\sigma_{xx} = \frac{kT}{V^*} \ln \left( 2 \frac{\dot{\epsilon}_p}{\dot{\epsilon}_0} \right) R_{11}. \quad (4.32)$$

In case  $\mu \neq 0$ , the hydrostatic pressure has to be considered, and is given by:

$$p = -1/3(\sigma_{xx} + \sigma_{yy} + \sigma_{zz}), \quad (4.33)$$

which equals  $-1/3\sigma_{xx}$  in uniaxial tension. In this case the Equations 4.28 and 4.31 will be given by:

$$\bar{\sigma}_H - \mu p = \frac{kT}{V^*} \ln \left( 2 \frac{\dot{\epsilon}_p}{\dot{\epsilon}_0} \right), \quad (4.34)$$

$$\sigma_{xx} = \frac{kT}{V^*} \ln \left( 2 \frac{\dot{\epsilon}_p}{\dot{\epsilon}_0} \right) \frac{1}{g(R_{ij}, \theta) + (\mu/3)}, \quad (4.35)$$

in case of  $\theta = 0^\circ$  gives:

$$\sigma_{xx} = \frac{kT}{V^*} \ln \left( 2 \frac{\dot{\epsilon}_p}{\dot{\epsilon}_0} \right) \frac{R_{11}}{1 + (\mu R_{11}/3)}. \quad (4.36)$$

Equations 4.32 and 4.36 show the difference in determining the value of  $R_{11}$  in case when  $\mu = 0$  and  $\mu \neq 0$ . If  $\mu \neq 0$ , the value of  $R_{11}$  obtained from Equations 4.9-4.12 should be corrected for the value of  $\mu$  according to:

$$R_{11} = \frac{R'_{11}}{1 + (\mu R'_{11}/3)}, \quad (4.37)$$

where  $R'_{11}$  is the adjusted value of the anisotropic parameter. In a similar fashion the value of  $R_{22}$  is determined. Finally, the value of  $R_{12}$  is obtained using a least-squares minimization to fit the experimental data. The values of the anisotropic parameters are originally obtained from Van Erp et al. [67] in which the pressure dependency parameter  $\mu$  was assumed to equal 0. Therefore, the value of the anisotropic parameters were adjusted according to Equation 4.37. Their values are shown in Table 4.4.

**Table 4.4:** Adjusted anisotropic parameters of PP [67].

	$R_{11}$ [-]	$R_{12}$ [-]	$R_{22}$ [-]
$\lambda=1$	1.0	1.0	1.0
$\lambda=4$	6	1.6	1.0
$\lambda=6$	14	2.3	1.0

## 4.4.2 Biaxial loading

In order to test the associated flow rule qualitatively, tension-tension biaxial simulations are performed. The biaxial simulations are 3D and represent one quarter of a full problem biaxial test, see Figure 4.4a. The two sides are equal with a length of 10 mm and a thickness of 0.5 mm. Since the thickness is significantly smaller than the length of the two sides, a plane stress case is assumed. In addition, transverse anisotropy is also considered. Similar to tensile samples, at an orientation angle  $\theta = 0$ , the material is assumed to be oriented along x-axis in case of anisotropy. Therefore, the anisotropic parameters are identical to those of the tensile simulations for a given stretch ratio. The 3D mesh consists of 16 hexahedron linear elements. Displacement boundary conditions are used to apply symmetric conditions where the x- and y-axis are the lines of symmetry. The plane that coincides with the x-axis is constrained in y-direction and the plane that coincides with the y-axis is constrained in x-direction, see Figure 4.4b. Two types of biaxial simulations are used; displacement controlled and load controlled. The displacement-controlled simulations are performed by simultaneously applying a constant strain rate in x- and y-directions, a strain rate of  $10^{-2} \text{ s}^{-1}$  is applied. The load-controlled simulations are performed by simultaneously building up equal stresses on both sides for 100 s. A constant stress of 32 MPa is reached and applied for  $10^4$  s.

## 4.5 Results and Discussion

### 4.5.1 Uniaxial tension and simple shear

Uniaxial tensile simulation are carried out and compared with experimental data from Van Erp et al. [67]. At stretch ratios  $\lambda = 4$  and  $6$  at orientation angle  $\theta = 0^\circ$ , the samples fractured in a brittle manner and consequently the ultimate tensile strengths were taken as yield stress, Figure 4.5a. Simulations are stopped at the same strain where fracture occurred during the experiments in order for the results to be comparable, see Figure 4.5b. In Figure 4.5 the tensile response of PP at increasing draw ratios at a strain rate of  $10^{-3} \text{ s}^{-1}$  is shown. A higher yield stress is observed as draw ratios increase as a result of increased crystalline structure orientation. During simulations, the elastic response does not change at increasing stretch ratios, this is because anisotropic elasticity is not considered. In addition, post yield response is slightly different in the isotropic case in which more softening is observed during experiments. This can be related to the inhomogeneity of deformation after the yield point. Whereas during simulations, a single-element is used which ensure homogenous deformation. Anisotropic samples with a stretch ratio of  $\lambda = 6$  were cut at different orientation angles with respect to the drawing direction. Figure 4.6



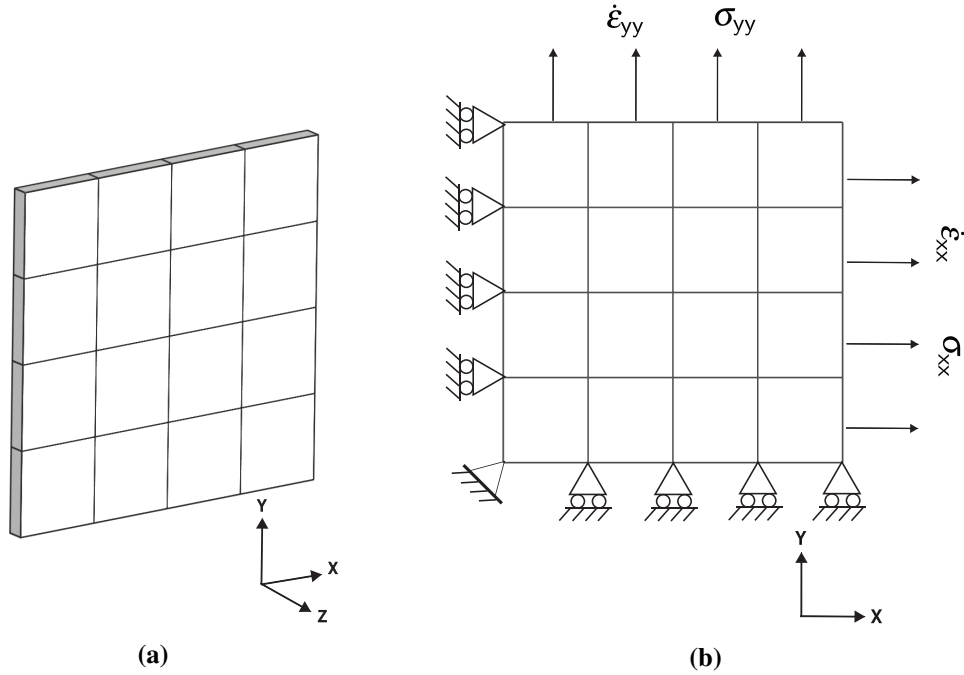


**Figure 4.4:** The biaxial FEM model representing one quarter of a full problem biaxial test, (a) 3D view of the biaxial FEM mesh, (b) side view showing the boundary conditions and the applied stresses and strain rates. Displacement boundary conditions are used to apply symmetric conditions.

shows the tensile response of these samples at a strain rate of  $10^{-3} \text{ s}^{-1}$ . Higher yield is observed at lower orientation angles since the crystalline structure is stretched along the loading direction. As the orientation angle increases the sample response approaches the isotropic behaviour. At  $\theta = 0^\circ$  the experimental response is similar to isotropic case, while the simulations show an identical response to the isotropic case. This is because in this case the Hill fourth order tensor  ${}^4\mathbf{H} = \frac{3}{2}{}^4\mathbf{I}$  and the isotropic Von Mises yield function  $\bar{\sigma}_{\text{VM}}$  is recovered:

$$\bar{\sigma}_{\text{H}} = \sqrt{\frac{3}{2} \boldsymbol{\sigma}_{\text{s}}^{\text{d}} : \boldsymbol{\sigma}_{\text{s}}^{\text{d}}} = \bar{\sigma}_{\text{VM}}. \quad (4.38)$$

Figure 4.7 shows a 3D uniaxial tensile simulation of PP at  $\lambda = 1$  and 4 and at a strain rate of  $10^{-3} \text{ s}^{-1}$ . One-eighth of an actual tensile sample is simulated with the proper boundary conditions applied in order to save computational time. Necking clearly appears at  $\lambda = 1$  after which inhomogeneous deformation takes place, whereas for  $\lambda = 4$  necking is delayed since yielding occurs at higher strain. The single-element and the 3D tensile simulations show similar response with necking appearing in the 3D simulations. Yield values are

plotted against strain rate at increasing stretch ratios and various orientation angles, see Figure 4.8. Interestingly when the results are plotted on a double logarithmic scale, the slopes are identical. This indicates that the strain-rate dependency on one hand and the stretch and orientation on the other hand are separated in a multiplicative way [67]:

$$\sigma_y = f(\dot{\epsilon})g(R_{ij}, \theta). \quad (4.39)$$

In Figure 4.9 yield values at increasing draw ratio at various orientation angles are shown. The fitting lines are obtained analytically using Equation 4.35 where  $\theta$  varied between  $0^\circ$ - $90^\circ$ . The rate constant  $\dot{\epsilon}_0$  is determined according to:

$$\dot{\epsilon}_0 = \frac{kT}{V^* \sum_{i=1}^n \eta_{0,\text{ref},i}}. \quad (4.40)$$

All FEM simulation points lie exactly on this line, which proves that the numerical implementation is done correctly. The model is validated in the shear direction via simple

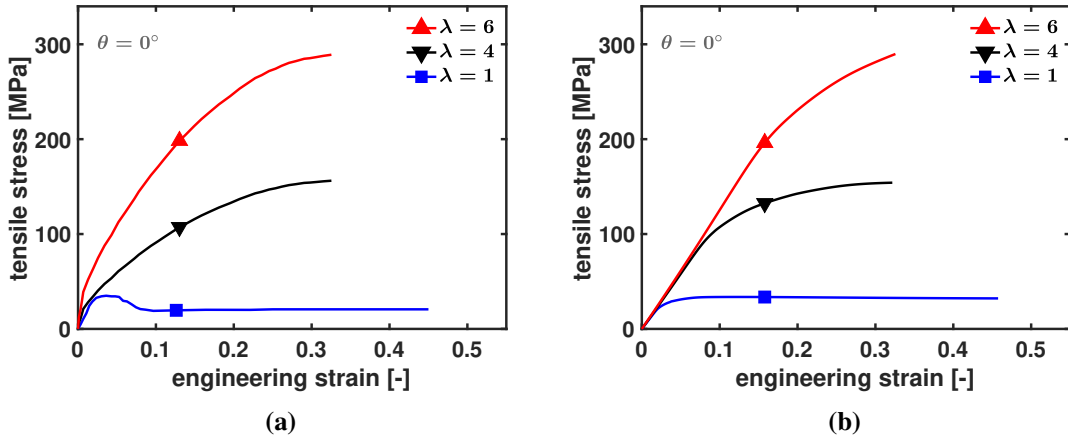


**Figure 4.5:** Uniaxial tensile response of PP at increasing draw ratios at strain rate of  $10^{-3} \text{ s}^{-1}$ ; (a) experiments [67], (b) FEM simulations using single element. Higher yield stress observed as draw ratio increases as a result of increased crystalline structure orientation.

shear simulations. A thin element is subdivided into 64 elements, see Figure 4.10a. The motion is fully restricted at the bottom face and a constant shear strain-rate  $\dot{\gamma}_{xy} = 10^{-3} \text{ s}^{-1}$  is applied on the top face. The simulations are performed at increasing draw ratios. It is observed from the results, Figure 4.10b, that a shear yield stress value of  $\tau_y = 21 \text{ MPa}$  is obtained for the isotropic case. The value of the normal yield stress at the same strain rate is  $\sigma_y = 34 \text{ MPa}$ , see Figure 4.9. Taking into account the difference between engineering and true stress, it can be noticed that the relation  $\tau_y = \sigma_y / \sqrt{3}$  is numerically verified. The

values of the shear stress at  $\lambda = 4$  and 6 are equal to the shear stress value for the isotropic case multiplied by the anisotropic parameter  $R_{12}$ . As mentioned earlier, the anisotropic parameters represent the ratio of the actual yield strength of the anisotropic material to the yield strength of the isotropic case. This proves the validity of the model in the shear direction.

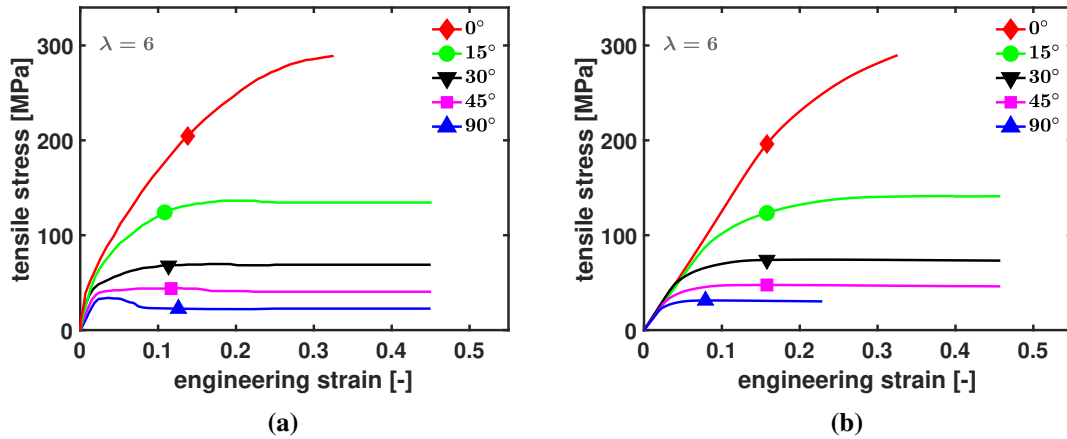


**Figure 4.6:** Uniaxial tensile response of PP samples cut at different angles with respect to the drawing directions at strain rate of  $10^{-3} \text{ s}^{-1}$ ; (a) experiments [67], (b) FEM simulations using single element. A higher yield stress is observed when samples are cut in the drawing direction due to increased anisotropy in that direction.

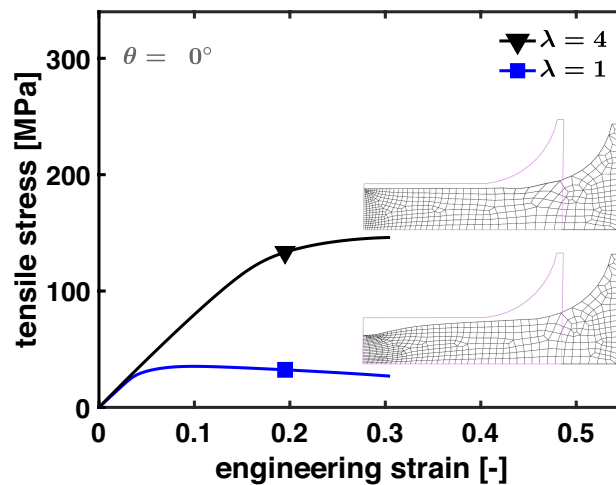


**Figure 4.7:** A 3D uniaxial tensile simulation of PP at  $\lambda = 1$  and 4 and at a strain rate of  $10^{-3} \text{ s}^{-1}$ . Necking clearly appears at  $\lambda = 1$  after which inhomogeneous deformation takes place.

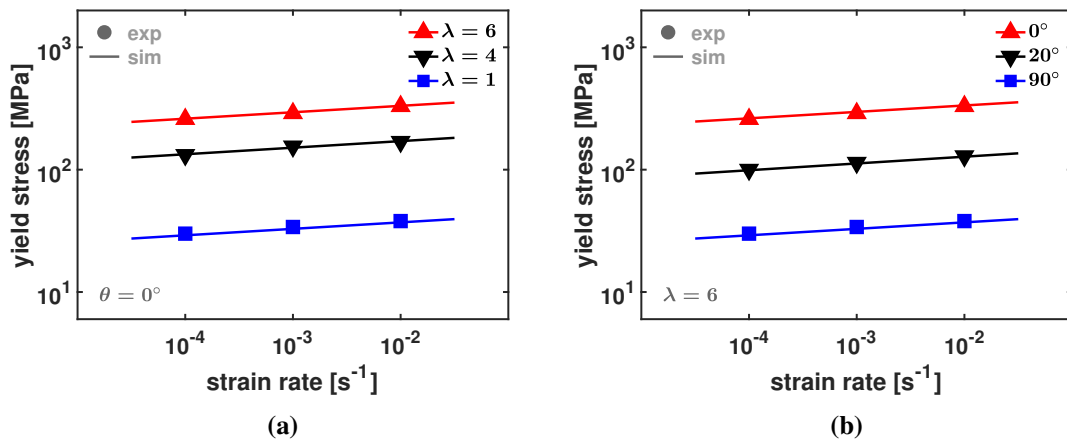


**Figure 4.8:** Uniaxial tensile yield stress values of PP at various strain rates; (a) at different stretch ratios, (b) at different orientation angles with respect to the drawing directions. Markers are experimental data points [67], lines are fitting of simulation data points. At  $90^\circ$  yield values converge to  $\lambda = 1$ , i.e. isotropic case.

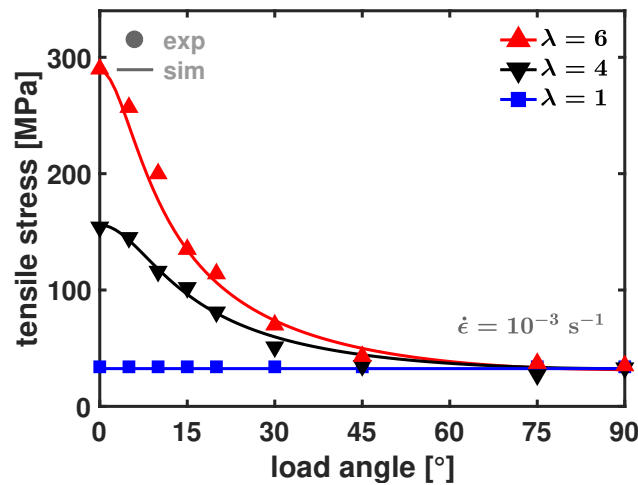


**Figure 4.9:** Tensile yield stress values of PP tapes at increasing draw ratio and various orientation angles at strain rate of  $10^{-3}$ . Markers are experimental data points [67], lines are analytical solution and fitting of simulation data points.

## 4.5.2 Biaxial simulations

In order to validate the model, uniaxial tests are necessary but not sufficient. Implementing the Hill yielding criterion can be validated via uniaxial simulations, however, in order to test the associated viscoplastic flow rule it is necessary to perform biaxial simulations. Two types of simulations are performed; displacement or stress controlled.

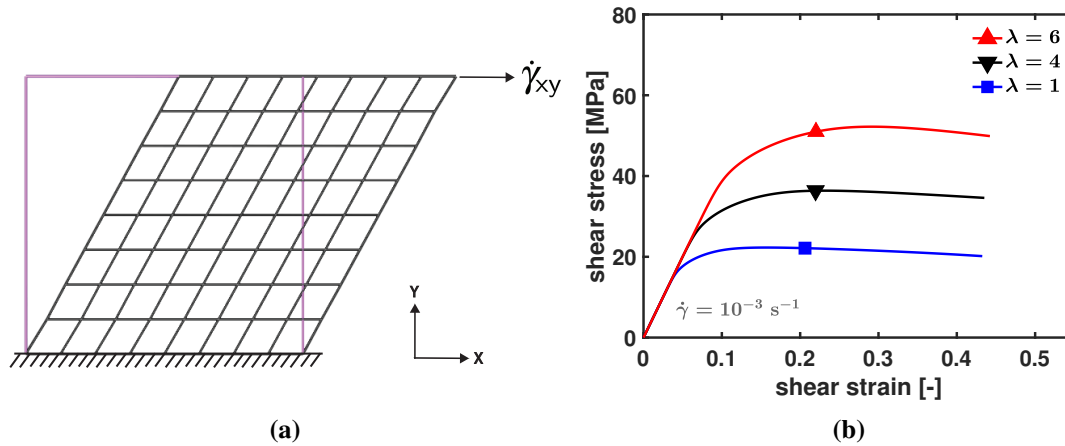


**Figure 4.10:** (a) Simple shear FEM simulation showing the original shape and the deformed mesh, (b) simple shear simulation results show the response of PP at increasing draw ratios and an applied shear strain rate of  $10^{-3}$ . Higher shear yield stress values are obtained as the draw ratios increase.

For the displacement-controlled simulations, a constant strain rate of  $10^{-2} \text{ s}^{-1}$  is applied on both sides of the FEM mesh, see Figure 4.4b. Figure 4.11 shows the response of the displacement-controlled biaxial simulations. For the isotropic case, i.e.  $\lambda = 1$ , the resulting stresses  $\sigma_{11}$  and  $\sigma_{22}$  are identical. Whereas the anisotropic case, i.e.  $\lambda = 4$  and 6, the stress values in the two directions are significantly different. A considerably higher stress is obtained along the direction of anisotropy  $\sigma_{11}$  due to the resistance of the material to deformation in that direction. The values of the yield stress in that direction are similar to the yield stress values obtained from the uniaxial loading at the same stretch ratio and strain rate, see Figure 4.8a. Perpendicular to the pre-stretch direction yield stress values comparable to the isotropic case are obtained. A significant yield drop is observed in that direction since the stress is mostly concentrated in the pre-stretch direction. The stress-controlled simulations are creep simulations where a stress of value of 32 MPa is applied on both sides. The stress is gradually built up till it reaches its maximum value in 100 s, then the stress is kept constant for  $10^4$  s. Figure 4.12a shows the resulting strain in both directions for the isotropic case. The primary, secondary and tertiary stages of the creep test can be observed in the results. The material flows with the same rate in both directions through all stages of the creep simulation. The final deformed shape of the mesh preserves the same ratio between the two sides of the mesh. The same stress is applied again on an anisotropic material of a stretch ratio of  $\lambda = 4$ . In this case it is easier for the material to flow perpendicular to the direction of the pre-stretch, see Figure 4.12b. Substantially higher strain  $\epsilon_{22}$  is obtained in that direction leaving only little deformation  $\epsilon_{11}$  along the direction of anisotropy. The final shape of the mesh clearly shows the direction of

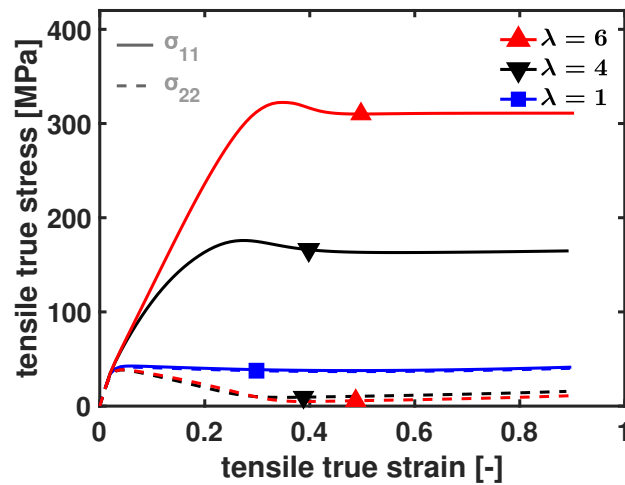


**Figure 4.11:** Simulation results of the displacement-controlled biaxial simulations at a strain rate of  $10^{-2} \text{ s}^{-1}$ . The resulting stresses are identical for the isotropic case. As the stretch ratio increases, stress values deviate with higher stresses obtained along the direction of anisotropy, i.e. pre-stretch direction.

deformation of the material. These results confirm that the associated viscoplastic flow rule is implemented successfully and determines the direction of the plastic flow of the material based on its given anisotropic state.

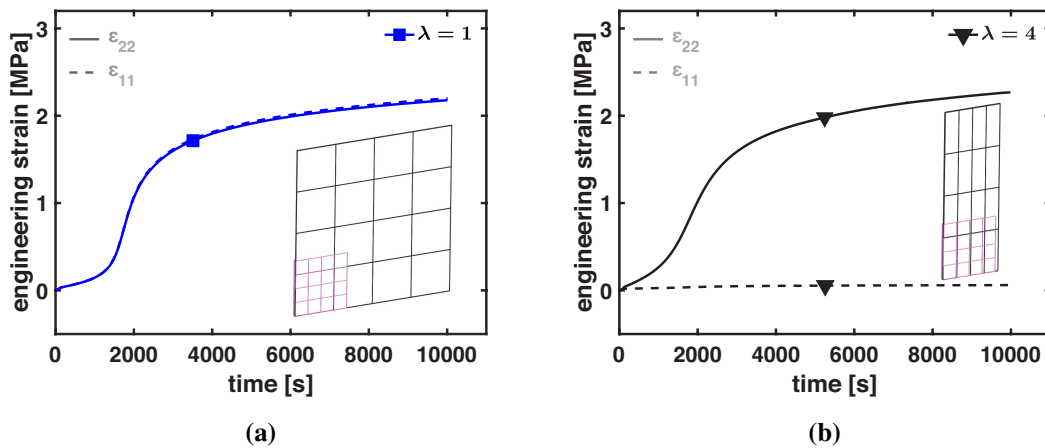


**Figure 4.12:** Simulation results of the stress-controlled biaxial simulations at a stress of 32 MPa, (a) isotropic case showing identical displacement in both directions, (b) anisotropic case with a stretch ratio of  $\lambda = 4$ , the material almost only flows in the direction perpendicular to the pre-stretch direction.

## 4.6 Conclusions

A 3D elasto-viscoplastic model based on Hill's yielding function is introduced. The model is implemented in finite element framework to model the response of the polymer during both uniaxial and biaxial loading. In order to determine the anisotropic parameters  $R_{ij}$  the pressure dependency parameter  $\mu$  should be considered. The values of the anisotropic parameters should be adjusted based on the value of  $\mu$  in order to correctly capture the experimental response of the polymer at various stretch ratios  $\lambda$  and orientation angles  $\theta$ . The model is able to quantitatively predict the yield values of the material at a given stretch ratio and orientation angle while taking strain-rate dependence into account. An associated viscoplastic flow rule is included in the model to simulate complex loading conditions like indentation or scratching. The flow rule gives the direction and the magnitude of the viscoplastic flow based on the anisotropy. The associated flow rule has been tested via biaxial simulations. A tension-tension displacement-controlled and load-controlled simulations are performed. The model qualitatively shows that the associated flow rule is indeed able to dictate the deformation direction for isotropic and anisotropic cases.

The presented model has its limitations. First, anisotropic elasticity is not considered since the model is developed to mainly simulate large plastic deformations. Another limitation is not taking the orientation-dependent strain-hardening into account. Looijmans et al. [73] showed that polypropylene displays a significant increase in strain hardening upon pre-stretching even at relatively small draw ratios, e.g.  $\lambda = 2$ . Finally, if an initially anisotropic polymer is subjected to large plastic deformations, the orientation tensors that define the state of anisotropy will change and the anisotropy directions will rotate with respect to their initial configuration. Since we are interested in large deformations, it may be plausible to include the evolution of anisotropy in future modelling efforts.

## Chapter 5

# Finite element modelling of a single-asperity scratch on an anisotropic polypropylene surface

### Abstract

Semi-crystalline polymers perform well in applications involving wear, bearings and structural loads thanks to their molecular structure. Semi-crystalline polymers products are usually anisotropic as a result of processing-induced crystalline orientation. Contact mechanics of anisotropic surfaces is investigated via a numerical approach to model the single-asperity scratch test. A 3D elasto-viscoplastic model, based on the Eindhoven Glassy Polymer (EGP) model, is developed to account for anisotropy and is implemented in a finite element framework. Isotactic polypropylene (iPP) is selected as a material model. Isotropic and anisotropic surfaces are scratched along and perpendicular to the direction of anisotropy. Scratch simulations provide qualitative measures on the effect of anisotropy on the scratch and frictional response of oriented polymers. It is shown that anisotropy reduces surface penetration as a result of increased yield stress. Results reveal that scratching a polymer surface along the orientation direction results in the lowest frictional resistance and permanent deformations. Moreover, strain hardening plays a crucial role in stabilizing the deformation zones along the scratched surface. On the other hand, sliding in the transverse direction results in the formation of a huge bow wave in front of the indenter as sideways deformation of the material is obstructed. This leads

---

Reproduced from: Tarek Kershah, Patrick D. Anderson, Lambert C.A. van Breemen. Finite element modelling of a single-asperity scratch on an anisotropic polypropylene surface. Submitted to *Tribology International*, (2020)



to a frictional resistance and plastic deformation magnitudes comparable to those of the isotropic scratched surfaces, however with a different residual scratch geometry. The model provides great insights on contact mechanics of oriented polymers and shows a clear qualitative agreement with previous experimental work in our group.

## 5.1 Introduction

Polymers are increasingly used in various applications due to their outstanding strength to weight ratio in addition to a variety of other favourable mechanical properties. Today, semi-crystalline polymers such as polyolefins are one of the most widely used materials in many industrial and medical applications [61–65]. Generally, applications where high wear resistance and/or good frictional properties are required, semi-crystalline polymers are the obvious choice. Physical insights on why these materials possess such advantageous tribological properties is of an utmost importance. Many studies aimed to address the topic of surface contact and the complexity it encounters [14–17]. Simplification of such complexity, i.e. multiple-asperity contact, was made via various statistical methods in order to achieve less complexity, i.e. single-asperity contact, and yet a well-defined case that can be used to study surface mechanics [9, 10]. In this respect, the single-asperity scratch test is considered.

Recently, several studies made use of the single-asperity scratch test to investigate various tribological properties. There are experimental studies [73, 80, 91], while others are merely numerical [29, 30], and some combined experimental/numerical techniques [1, 2, 53, 113]. Moreover, the numerical studies can be split into qualitative [29, 30, 32], and quantitative ones [1, 2, 113]. Jiang et al. [80] experimentally studied the effect of stick-slip on the scratch performance of polypropylene and the appearance of the so-called “fish-scale” damage pattern. A combined experimental/numerical approach was performed by Van Breemen et al. [1] to couple the intrinsic material properties to the observed frictional response of polycarbonate. His work was based on the Eindhoven Glassy Polymer (EGP) constitutive model, which is a 3D elasto-viscoplastic model developed to describe the intrinsic mechanical response of polymers glasses and considers the non-linear visco-elastic response and the thermo-rheological complex behaviour of polymers [23, 37–39, 43, 47, 56]. In continuation to this work, Krop et al. [2] quantitatively described the intrinsic material response of isotropic particle-filled polycarbonate using representative volume element (RVE) [114].

For semi-crystalline polymers, the influence of processing-induced orientation is significantly large, and as a result, their mechanical response is highly anisotropic [92–95]. For this reason, Van Erp et al. [67] and Senden et al. [90] made use of the existing EGP model and the rate-independent anisotropic yielding function first introduced by Hill [105, 106] to predict the effect of anisotropy and orientation on the resulting yield response of polypropylene and polyethylene tensile tapes. As a continuation, we implemented the extended EGP model in FEM to simulate uniaxial and biaxial tensile tests, see Chapter 4.

Looijmans et al. [73, 91] studied the contact mechanics of semi-crystalline polymers and the effect of pre-stretch on the frictional and wear response. A clear difference in scratch and frictional response was observed between isotropic and oriented polymers on both polypropylene and polyethylene surfaces. Moreover, a significant difference appeared when the scratch was performed along the pre-stretch direction, i.e. machine direction (MD), as opposed to scratching in the perpendicular direction, i.e. transverse direction (TD).

Recently, Kershah et al. [113] implemented the EGP model in Finite Element Method (FEM)-framework to investigate the scratch and frictional response of polypropylene in a combined numerical/experimental approach. However, anisotropy was not accounted for, and as mentioned earlier, semi-crystalline polymers are highly anisotropic. This is due to the combination of their microstructure and processing conditions. It has been proven that anisotropy plays a great role in altering the scratch and frictional response of polyolefins upon pre-stretching [73, 91].

In this work a qualitative numerical study is performed. The model is based on the EGP constitutive model and the incorporation of Hill's yielding criterion and an associated viscoplastic flow rule to account for anisotropy. Isotactic polypropylene (iPP) is chosen as a material model since it has been well characterized in our group [56, 67–71, 113]. The aim is to give insights on the deformation mechanics associated with scratching anisotropic polypropylene surfaces and identify how anisotropy alters its response when scratched. Moreover, our approach explains the clear differences observed experimentally by Looijmans et al. [73] upon scratching isotropic and anisotropic polypropylene surfaces in both MD and TD as a result of intrinsic deformation mechanisms.

## 5.2 Constitutive Modelling

This section explains the EGP constitutive model similar to [113], and the incorporation of Hill's yielding function similar to [90].

### 5.2.1 Stress calculation

The total stress  $\sigma$  is split into driving  $\sigma_s$  and the hardening stress  $\sigma_r$ :

$$\sigma = \sigma_s + \sigma_r. \quad (5.1)$$

The hardening stress is described with a simple neo-Hookean rubber-elastic model:

$$\boldsymbol{\sigma}_r = \frac{G_r}{J} \tilde{\mathbf{B}}^d, \quad (5.2)$$

herein,  $G_r$  denotes the hardening modulus,  $\tilde{\mathbf{B}}^d$  is the deviatoric part of the isochoric left Cauchy-Green strain tensor, and  $J$  is the volume change ratio. The driving stress consists of multiple Maxwell elements connected in parallel and is split into a hydrostatic  $\boldsymbol{\sigma}_s^h$  and a deviatoric parts  $\boldsymbol{\sigma}_s^d$ :

$$\boldsymbol{\sigma}_s = \boldsymbol{\sigma}_s^h + \boldsymbol{\sigma}_s^d = \kappa(J - 1)\mathbf{I} + \sum_{i=1}^n G_i \tilde{\mathbf{B}}_{e,i}^d, \quad (5.3)$$

where,  $\kappa$  is the bulk modulus,  $G$  is the shear modulus,  $\tilde{\mathbf{B}}_e^d$  is the elastic deviatoric part of the isochoric left Cauchy-Green strain tensor, and subscript  $i$  refers to a specific mode, and  $n$  denotes the number of modes [40]. A non-Newtonian flow rule controls the relation between the plastic deformation-rate tensor  $\mathbf{D}_p$  and the deviatoric stress  $\boldsymbol{\sigma}_s^d$ :

$$\mathbf{D}_{p,i} = \frac{\boldsymbol{\sigma}_{s,i}^d}{2\eta_i}, \quad (5.4)$$

where  $\eta_i$  are the viscosities of each Maxwell element. It should be noted that this flow rule is non-directional, this means that it can only be employed in isotropic cases. Viscosities are determined via extended Eyring flow rule [39, 81–83]:

$$\eta_i = \eta_{0,\text{ref},i} \frac{\bar{\tau}/\tau_0}{\sinh(\bar{\tau}/\tau_0)} \exp\left[\frac{\mu p}{\tau_0}\right] \exp[S_a R_x(\bar{\gamma}_p)] \exp\left[-\frac{\Delta U}{RT} \left(\frac{T - T_{\text{ref}}}{T_{\text{ref}}}\right)\right], \quad (5.5)$$

where  $\eta_{0,\text{ref},i}$  are the reference viscosities of each Maxwell element,  $\bar{\tau}$  is the total equivalent stress,  $\tau_0$  is the characteristic shear stress,  $p$  is the hydrostatic pressure. The pressure dependency determines the contribution of the hydrostatic pressure on viscosity and is governed by the parameter  $\mu$ . The thermo-mechanical history of the material is contained in the state parameter  $S_a$ .  $\Delta U$  is the activation energy,  $R$  is the universal gas constant,  $T$  represents the temperature, and  $T_{\text{ref}}$  is the room temperature. The softening function  $R_x(\bar{\gamma}_p)$  describes the strain-softening process similar to Klompen et al. [43] using a modified Carreau-Yasuda relation:

$$R_x(\bar{\gamma}_p) = \left[ \frac{1 + (r_0 \cdot \exp(\bar{\gamma}_p))^{r_1}}{1 + r_0^{r_1}} \right]^{(r_2 - 1)/r_1}, \quad (5.6)$$

where  $\bar{\gamma}_p$  is the equivalent plastic strain, and  $r_0$ ,  $r_1$ , and  $r_2$  are the fitting parameters. Moreover,  $\tau_0$  is determined using the following equation:

$$\tau_0 = \frac{k_b T}{V^*}, \quad (5.7)$$

where  $k_b$  is the Boltzmann's constant and  $V^*$  is the activation volume.

## 5.2.2 Extension to thermo-rheologically complex behaviour

Polypropylene is proven to exhibit thermo-rheologically complex behaviour [56]. To capture this complex behaviour we use an extension of Equation 5.1 based on Ree-Eyring theory [84]:

$$\sigma = \sigma_{s,1} + \sigma_{s,2} + \sigma_r, \quad (5.8)$$

where  $\sigma_{s,1}$  is the driving stress of the primary process ( $\sigma_s$  in Equation 5.3), and  $\sigma_{s,2}$  is the driving stress for the secondary process. Figure 5.1 shows the upper- and lower-yield stress of polypropylene at various strain rates obtained from [71]. The upper-yield stress displays a higher strain-rate dependence than the lower-yield stress which implies the existence of a secondary molecular process, in addition to the primary one, controlling the upper-yield stress.

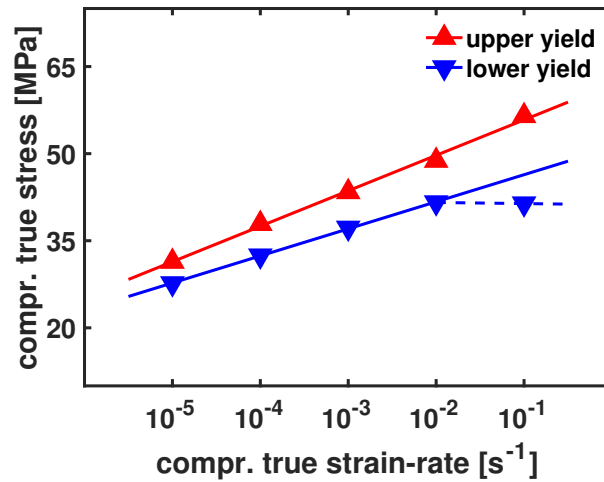


**Figure 5.1:** Upper- and lower-yield stress values of iPP at increasing strain rates, data obtained from [71] and formerly shown in our previous work [113].

### 5.2.3 Extension to thermo-mechanically coupled model

The decrease in slope of the lower-yield stress at the highest strain rate shown by dotted line in Figure 5.1 comes from heat generation resulting from plastic deformation. Plastic deformation converts mechanical work into heat through an irreversible process. The thermo-mechanically coupled model formulated is analogous to Boyce et al. [75] and is explained in full detail in our previous work [113]. The final equation of temperature evolution  $\dot{T}$  is given by:

$$\dot{T} = \frac{1}{\rho c_p} \left[ \Gamma(\boldsymbol{\sigma}_s : \mathbf{D}_{p,i}) - k(T - T_{\text{ref}}) \right], \quad (5.9)$$

herein,  $\rho$  being the material density and  $c_p$  the specific heat capacity,  $\Gamma$  is the percentage of mechanical work dissipated into heat. The boundary condition parameter  $k$  describes the heat loss through conduction/convection. It is formulated similar to [43, 113], and is determined by fitting the simulation results to the experimental compression data. The evolution equation is then solved using the forward Euler method:

$$T_c = T_b + \Delta t \dot{T}, \quad (5.10)$$

where  $T_c$  is the nodal temperature of the current increment,  $T_b$  is the temperature of the previous increment, and  $\Delta t$  is the incremental time step. To obtain the model parameters, single-element FEM compression simulations are performed and fitted to experimental data, obtained from [71], see Figure 5.2. The material parameters are shown in Tables 5.1, 5.2 and 5.3. The Material parameters are equivalent to the material parameters of  $\alpha$ -iPP in our previous work [113]. In the scratch simulations, the value of the thermo-mechanical history parameter  $S_a$  is set to 0 instead of  $S_a = 5$  used during compression and tensile simulations. The reason is to introduce more indentation into the polymer so that the effect of anisotropy on deformation, i.e. the size of the bow wave for instance, is more visible. In addition, the pressure dependency parameter  $\mu$  is also set to 0 instead of  $\mu = 0.12$  used here. The reason will be explained in Section 5.2.4.

### 5.2.4 Extension to an anisotropic yield function

The main objective of this work is studying the effect of anisotropy on the scratch and frictional response. Therefore, it is necessary to extend the model to account for anisotropy. First, we need an anisotropic yielding function. Hill function is the most commonly used yielding criterion for anisotropic materials [105, 106], it has been used by many researchers [67, 90, 97, 100, 110, 111]. In Chapter 4 this function has been incorporated in the EGP model and implemented in FEM to simulate uniaxial and biaxial

**Table 5.1:** Reference spectrum of iPP.

Process 1	Mode	$\eta_{0,i,ref}$ [MPa.s]	$G_i$ [MPa]
	1	$1.6 \times 10^8$	110
	2	$3.5 \times 10^7$	90
	3	$2.3 \times 10^6$	70
	4	$3.3 \times 10^5$	60
	5	$3.3 \times 10^4$	40
	6	$6.7 \times 10^3$	30
Process 2	Mode	$\eta_{0,i,ref}$ [MPa.s]	$G_i$ [MPa]
	1	$2.4 \times 10^{-2}$	80

**Table 5.2:** Material parameters of iPP, adopted from [56].

$G_r$ [MPa]	$\kappa$ [MPa]	$S_a$ [-]	$\mu$ [-]	$V_1^*$ [nm <sup>3</sup> ]
1.6	1650	5.0	0.12	3.10
$V_2^*$ [nm <sup>3</sup> ]	$\rho$ [gm/cm <sup>3</sup> ]	$r_0$ [-]	$r_1$ [-]	$r_2$ [-]
3.0	0.90	0.95	2.0	-0.5

**Table 5.3:** Thermal parameters of iPP, activation energy and specific heat capacity obtained from [76].

$\Gamma$ [-]	$k$ [MPa/K s]	$\Delta U_1$ [kJ/mole]	$\Delta U_2$ [kJ/mole]	$c_p$ (kJ/kg K)
0.6	0.10	274	251	1.92

tensile tests. In that study full details of the implementation and validation of the model is shown. Hill equivalent stress  $\bar{\sigma}_H$  is determined as follows:

$$\bar{\sigma}_H^2 = F(\sigma_{22} - \sigma_{33})^2 + G(\sigma_{33} - \sigma_{11})^2 + H(\sigma_{11} - \sigma_{22})^2 + \dots$$

$$2L\sigma_{23}^2 + 2M\sigma_{13}^2 + 2N\sigma_{12}^2, \quad (5.11)$$

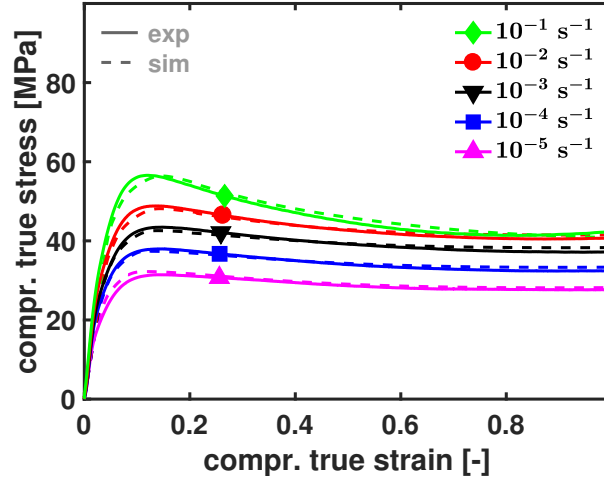


**Figure 5.2:** Fitting uniaxial single-element compression simulation results to experimental data obtained from [71], results adopted from our previous work [113].

$$F = \frac{1}{2} \left( \frac{1}{R_{22}^2} + \frac{1}{R_{33}^2} - \frac{1}{R_{11}^2} \right); \quad L = \frac{3}{2R_{23}^2}; \quad (5.12)$$

$$G = \frac{1}{2} \left( \frac{1}{R_{11}^2} + \frac{1}{R_{33}^2} - \frac{1}{R_{22}^2} \right); \quad M = \frac{3}{2R_{13}^2}; \quad (5.13)$$

$$H = \frac{1}{2} \left( \frac{1}{R_{11}^2} + \frac{1}{R_{22}^2} - \frac{1}{R_{33}^2} \right); \quad N = \frac{3}{2R_{12}^2}; \quad (5.14)$$

where  $\sigma_{ij}$  are the stress components with respect to the material coordinate system,  $R_{ij}$  are the anisotropic parameters, they represent the ratio of the actual yield strength of the anisotropic material to that of the isotropic at a specific normal or shear direction. We have three normal parameters ( $R_{11}$ ,  $R_{22}$ ,  $R_{33}$ ) and three shear parameters ( $R_{12}$ ,  $R_{13}$ ,  $R_{23}$ ). To account for material orientation, the vectors  $\vec{e}_1$ ,  $\vec{e}_2$  are defined as the orthogonal vectors which coincides with the material axes:

$$\vec{e}_1 = \begin{Bmatrix} \cos\theta \\ \sin\theta \\ 0 \end{Bmatrix}; \quad \vec{e}_2 = \begin{Bmatrix} -\sin\theta \\ \cos\theta \\ 0 \end{Bmatrix}, \quad (5.15)$$

vector  $\vec{e}_3$  is always perpendicular to the plane of the tensile/scratch sample, so it can be ignored. The angle  $\theta$  represents the angle between the material axes and the global coordinate systems, i.e. the angle at which the sample is cut with respect to the drawing



or extrusion directions. The orientation tensors  $\mathbf{R}_1$  and  $\mathbf{R}_2$  are given by:

$$\mathbf{R}_1 = \vec{e}_1\vec{e}_1; \quad \mathbf{R}_2 = \vec{e}_2\vec{e}_2. \quad (5.16)$$

An extended invariant form of Hill's function similar to [90] is given by:

$$\begin{aligned} \bar{\sigma}_H = & \left[ (L + M - N)\text{tr}(\boldsymbol{\sigma}_s^d \cdot \boldsymbol{\sigma}_s^d) + (F + 4G + H - 2M)\text{tr}^2(\boldsymbol{\sigma}_s^d \cdot \mathbf{R}_1) + (-2L + 2N)\dots \right. \\ & \text{tr}(\boldsymbol{\sigma}_s^d \cdot \mathbf{R}_1 \cdot \boldsymbol{\sigma}_s^d) + (4F + G + H - 2L)\text{tr}^2(\boldsymbol{\sigma}_s^d \cdot \mathbf{R}_2) + (-2M + 2N)\text{tr}(\boldsymbol{\sigma}_s^d \cdot \mathbf{R}_2 \cdot \boldsymbol{\sigma}_s^d) + \dots \\ & \left. (4F + 4G - 2H - 2L - 2M + 2N)\text{tr}(\boldsymbol{\sigma}_s^d \cdot \mathbf{R}_1)\text{tr}(\boldsymbol{\sigma}_s^d \cdot \mathbf{R}_2) \right]^{1/2}. \quad (5.17) \end{aligned}$$

The same relation can also be written as follows:

$$\bar{\sigma}_H = \sqrt{\boldsymbol{\sigma}_s^d : {}^4\mathbf{H} : \boldsymbol{\sigma}_s^d}, \quad (5.18)$$

where  ${}^4\mathbf{H}$  is Hill fourth order anisotropy tensor. This tensor is function of  $R_{ij}$  and  $\theta$ . In the isotropic case, i.e.  $R_{ij} = 1$ , or when  $\theta = 90^\circ$ , i.e. loading perpendicular to the anisotropy direction, the Hill fourth order tensor  ${}^4\mathbf{H} = \frac{3}{2} {}^4\mathbf{I}$ . This leads to a non-directional yielding criterion relation:

$$\bar{\sigma}_H = \sqrt{\frac{3}{2} \boldsymbol{\sigma}_s^d : \boldsymbol{\sigma}_s^d}. \quad (5.19)$$

To validate our model, single-element tensile simulations are performed and compared to experimental data from Van Erp et al. [67]. The polypropylene grade used in the tensile tests possess almost identical response to the grade used by Caelers et al. [71] for the compression tests data used earlier. The tapes were drawn at draw ratios of  $\lambda = 1, 4$ , and  $6$ . As the material is being drawn in one direction, the crystalline structure is oriented along that direction inducing anisotropy. Tensile samples were then cut from these tapes at different orientation angles with respect to the drawing direction  $\theta$ , ranging from  $0^\circ$  till  $90^\circ$ . The values of the anisotropic parameters are taken from Van Erp et al. [67]. The anisotropic parameters represent the ratio of the actual yield strength of the anisotropic material to the reference yield strength, i.e. isotropic case. Two assumptions are made, transverse isotropy, i.e.  $R_{22} = R_{33}$ , and plane stress. This means only three parameters are needed;  $R_{11}$ ,  $R_{22}$ , and  $R_{12}$ . Finding the values of  $R_{11}$ ,  $R_{22}$  is straightforward given the value of the yield stress at a given stretch ratio. The value of  $R_{12}$  is obtained using a least-squares minimization to fit the experimental data. The assumption of transverse isotropy holds for the scratch simulations. However, the plane stress assumption does not hold, see Section 5.3. As a result, during scratching the other shear parameters  $R_{13}$  and

$R_{23}$  are assumed to have the same value of  $R_{12}$ . The values of the anisotropic parameters are shown in Table 5.4. Looking at the results of Figure 5.3, higher yield is observed at increasing draw ratios, i.e. anisotropy, and at lower orientation angles  $\theta$  since the crystalline structure is stretched along the loading direction. As the orientation angle increases the sample response approaches the isotropic behaviour. Although the flow rule used so far is a non-directional one, it is valid to only use the non-directional yielding function, i.e. Hill's function, to determine the yield value in the uniaxial loading cases. However, if multiaxial loading is applied the Hill yield function will not be sufficient to describe the correct response. The non-directional flow rule previously used will have to be replaced by a directional anisotropic flow rule in order to capture the actual response. It should be noted that if the pressure dependence parameter  $\mu > 0$  the anisotropic parameters will have to be adjusted according to:

$$R_{11} = \frac{R'_{11}}{1 \pm (\mu R'_{11}/3)}, \quad (5.20)$$

where  $R'_{11}$  is the adjusted value of the anisotropic parameter. The proof of Equation 5.20 is explained in full detail in Chapter 4. The positive and negative signs depend on the direction of the loading, i.e. compressive or tensile. Scratching is a complex loading case where an element can be subjected to cyclic compressive-tensile loading, it would be challenging to use the abovementioned formula in the constitutive model and assigning a positive or a negative value depending on the loading direction at each element within the mesh. For simplicity the value of  $\mu$  is set to 0 during the scratch simulations, and therefore, the values of the anisotropic parameters  $R_{ij}$  are constants throughout the simulation for all elements regardless of the direction of the load acting on an element.

**Table 5.4:** Anisotropic parameters of iPP, adopted from [67].

	$R_{11}$ [-]	$R_{12}$ [-]	$R_{22}$ [-]
$\lambda=1$	1.0	1.0	1.0
$\lambda=4$	4.85	1.6	1.0
$\lambda=6$	9.0	2.3	1.0

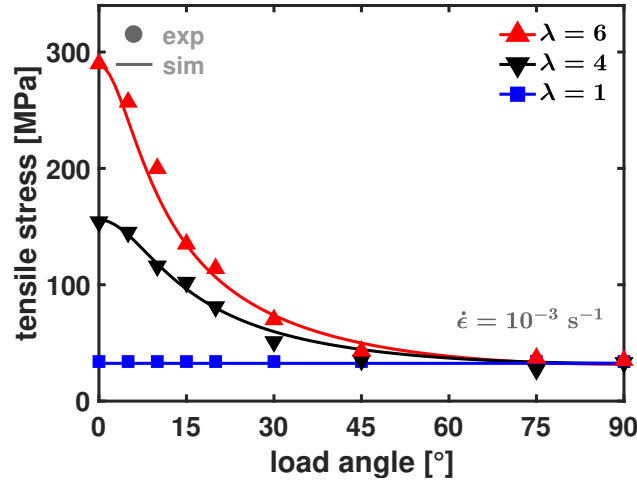


**Figure 5.3:** Tensile yield stress values of PP tapes at increasing draw ratio and various orientation angles at strain rate of  $10^{-3}$ . Markers are experimental data points [67], lines are fitting of simulation data points.

### 5.2.5 Extension to an anisotropic viscoplastic flow rule

The anisotropic viscoplastic flow rule determines the rate of deformation of the material at any given stress state. Similar to [67, 90], the anisotropic flow rule is given by:

$$D_p = \dot{\epsilon}_p N, \quad (5.21)$$

where  $\dot{\epsilon}_p$  represents the magnitude of the plastic deformation-rate, i.e. equivalent plastic strain-rate, and can simply be obtained by dividing viscosity by equivalent stress, while the tensor  $N$  determines the direction of viscoplastic flow and is given by:

$$N = \frac{1}{\bar{\sigma}_H} ({}^4H : \sigma_s^d). \quad (5.22)$$

### 5.2.6 FEM mesh friction modelling

The EGP constitutive model is implemented in the MSC.Marc FEM package. Figure 5.4a shows a 3D view of the scratch simulation. The single-asperity scratch simulation is a symmetric one, only half of the actual volume is meshed. The meshed volume is  $0.2 \times 0.2 \times 0.8 \text{ mm}^3$ . Linear elements are used since they are preferred in contact analysis according to MSC.Marc documentation [49]. A local automatic mesh adaptivity criterion is used and applied to the surface which has the greatest interest. The symmetry plane is the x-z plane; therefore, the displacement is restrained in y-direction. Moreover, during

indentation all edges are restrained in x- and z-directions except the surface and the symmetry plane. During scratching all x-direction restrains is deactivated, and instead, the mesh moves in the negative x-direction. An indenter with a tip radius 50  $\mu\text{m}$  is used, and is modelled as a rigid body. The simulation is split into two parts. First, indentation to a normal load  $F_n = 300$  mN for 25 s. This is followed by sliding with a constant velocity of 1, 10 or 100  $\mu\text{m/s}$  for 600, 60 or 6 s respectively in order to scratch the same distance at each scratch speed. Scratching is performed on isotropic surfaces, i.e.  $R_{ij} = 1$ , and anisotropic surfaces in MD and TD. MD means scratch is performed in the direction along which material is pre-stretched, i.e.  $\theta = 0^\circ$ , TD is the perpendicular direction, i.e.  $\theta = 90^\circ$ . Local friction is modelled with a simple built-in model in MSC.Marc called the arctangent model. It represents an approximation of Coulomb's friction model and it is used to smoothen the stick-slip transition, similar to [1, 2, 113]. The model is given by:

$$\mathbf{f}_t = -\mu_f f_n \frac{2}{\pi} \arctan \left[ \frac{\|\mathbf{v}_r\|}{\delta} \right] \mathbf{t}, \quad (5.23)$$

where  $\mathbf{f}_t$  and  $f_n$  are the friction and normal forces respectively,  $\mu_f$  the local friction coefficient,  $\mathbf{v}_r$  is the relative sliding velocity, and  $\mathbf{t}$  is the tangential vector. The parameter  $\delta$  is the smoothening parameter which determines the value of the relative velocity below which sticking occurs. An abrupt or sharp stick-slip is not desired in numerical simulations. On the other hand, a too smooth transition will only result in an underestimation of the lateral force. In this respect, the value of  $\delta$  should be carefully chosen so that neither convergence or accuracy is compromised. In our previous work [113] a local friction coefficient value of  $\mu_f = 0.28$  is found to give the best description of the experimental scratching data of iPP. However, the introduction of anisotropy to our model results in more numerical problems and convergence becomes more difficult. Reducing friction coefficient value from  $\mu_f = 0.28$  to 0.20 reduced the numerical problems by lowering the severe mesh distortions and the bow wave. For this reason and the fact that our work is only qualitative, a lower friction coefficient value of  $\mu_f = 0.20$  is used in all simulations. The local friction coefficient is independent of sliding speed and is assumed to be independent of anisotropy as well. Figure 5.4b and 5.4c show the side and top views of the mesh.

### 5.3 Results and Discussion

The contact mechanics of isotropic and oriented iPP surfaces are studied by means of FEM scratch simulations. A rigid indenter tip penetrates into the surface at an applied normal load of  $F_n = 200$  mN being built up gradually for 25 s. After indentation, the indenter starts sliding with a velocity  $v_s = 1, 10$  or 100  $\mu\text{m/s}$ . As the indenter starts

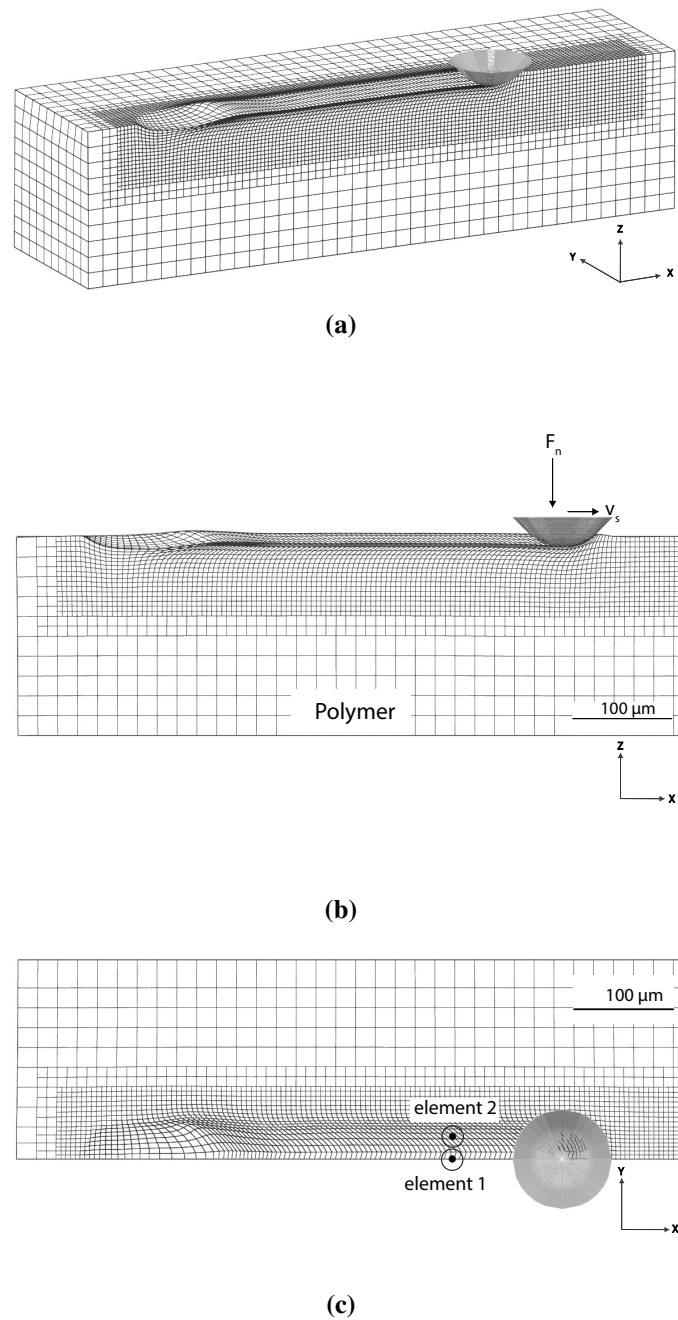


**Figure 5.4:** FEM mesh of single-asperity scratch simulation; (a) 3D view during scratching, (b) side view showing directions of applied normal force  $F_n$  and scratch velocity  $v_s$  on polymer surface, (c) top view showing the location of the two elements considered to be used in our analysis.

scratching, the material in front of the tip is compressed forming a bow wave, whereas the material behind the tip is being stretched along the scratch direction creating a tensile

stress field. The transition zone between tensile and compressive stresses is the area subjected to the largest shear stresses which results from the frictional contact. The large shear stress pushes the tip upwards till the area of contact is stabilized. From the point where the area of contact is stabilized the measured depth reached by the indenter is the steady-state value of the penetration depth. More penetration leads to more contact by creating more contact between the material and the indenter which induces more frictional resistance. The measured resistive force after the area of contact is stabilized is the steady-state friction force. Figure 5.5 shows the three principle components of true stress during a single-asperity scratch simulation on an isotropic surface at 100  $\mu\text{m/s}$  acting on element 1 and element 2 previously shown in Figure 5.4c. Element 1, which lies along the centre of the scratched cross section, is first subject to compressive stresses in all three directions as it takes part in forming the bow wave followed by being compressed beneath the indenter, see Figure 5.5a. After it passes by the transition zone it is immediately subjected to a tensile stress in all directions induced by the motion of the indenter as it continues sliding. The highest compressive stress acting on element 1 is in z-direction because this is the direction of the normal load which compresses the element as it moves beneath the indenter. After it passes the transition zone, element 1 starts to get stretched in x-direction creating the largest component of tensile stress in that direction. Element 2 experiences similar compressive stress field forming the bow wave and compressing beneath the indenter, see Figure 5.5b. However, it experiences almost no stretching after it passes the transition zone since most of the stretching occurs to the elements along or close to the centre of the scratch. The final shape of the elements that lie behind the indenter in Figure 5.4c confirms this analysis. A non-zero value of true stress in all three principle directions indicates that a plane stress assumption previously mentioned in Section 5.2.4 is not valid. Therefore, all anisotropic parameters need to be determined unless other assumptions, i.e. transverse isotropy, are made.

The values of the steady-state penetration depth at increasing pre-stretch ratios  $\lambda$  and sliding speeds  $v_s$  are displayed in Figure 5.6a. At lower sliding speeds, the tip penetrates more into the polymer surface due to its viscoelastic nature. This leads to more indenter-polymer contact, and thus, more resistance to the motion of the indenter and thus the friction force increases, see Figure 5.6b. A significant decrease in the steady-state penetration depth is observed on anisotropic surfaces when the scratch is performed in TD. This is due the increased yield stress of the polymer which leads to less penetration during the indentation phase. As the indenter starts to slide, the bow wave starts to form in front of the tip. The accumulated material is then pushed towards the MD, however, the sideways deformation is obstructed since it is the direction of the pre-stretch, i.e. orientation. This leads to more material accumulation in front of the tip creating a huge bow wave. This leads to more indenter-polymer contact and more friction force pushing the tip upwards. On the other hand, scratching in MD results in larger steady-

state penetration depth than the isotropic case, although the yield stress is higher and the tip penetrates less than the isotropic case during indentation. This is due to the fact that bow wave formation in MD is entirely absent since deformation is obstructed along the scratch direction, and material is mainly deformed sideways preventing the material accumulation in front of the tip. In this respect, a lower indenter-polymer contact is achieved leading to less friction force to push the indenter upwards as in the isotropic and the TD cases. Experimental data from Looijmans et al. [73] agrees with our simulation results for TD. However, penetration depths obtained experimentally in MD and TD are almost equivalent. Upon pre-stretching polymers, significant strain hardening develops in MD as a result of the extended molecular chains and crystals in case of semi-crystalline polymers. This has been proven by tensile tests of oriented polymers [73, 108, 115]. Our model does not account for orientation-dependent strain-hardening. Strain hardening is the main cause of the lowered penetration depth observed experimentally [73]. To test

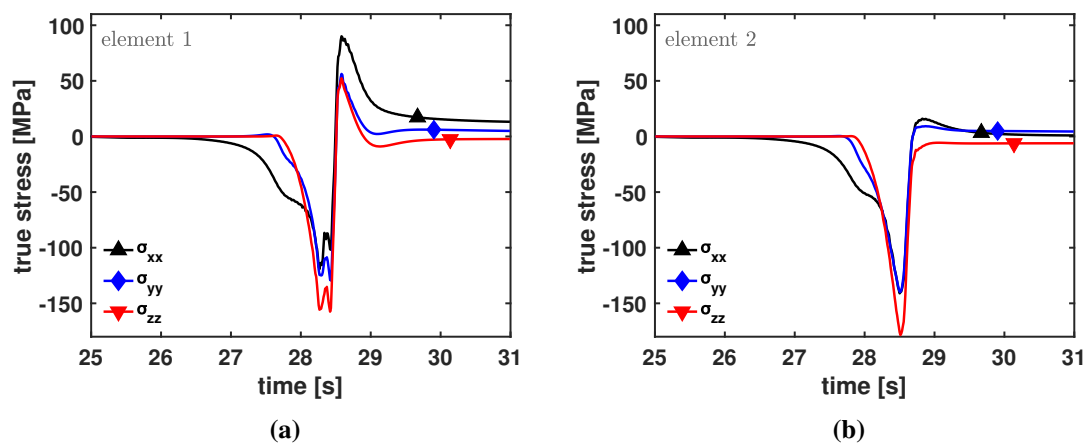


**Figure 5.5:** The three principle components of true stress during single-asperity scratch simulation on isotropic surface at 100  $\mu\text{m/s}$  acting on (a) element 1 and (b) element 2. A non-zero value of true stress in all principle directions indicates that a plane stress assumption is not valid.

this numerically, we use a randomly high value for strain hardening in MD. The result is a significant drop in penetration depth accompanied by an expected drop in friction force, see Figures 5.6c and 5.6d. These results are qualitatively in good agreement with the experimental data obtained from [73]. This proves that the significant rise in strain hardening upon stretching indeed lowers the steady-state penetration depth in MD. High strain hardening resists surface penetration by stabilizing the deformation zones and resisting the formation of localized plastic deformation zones. Previous work from our group shows how strain hardening plays a major role in enhancing scratch resistance by resisting strain localization [53, 113].

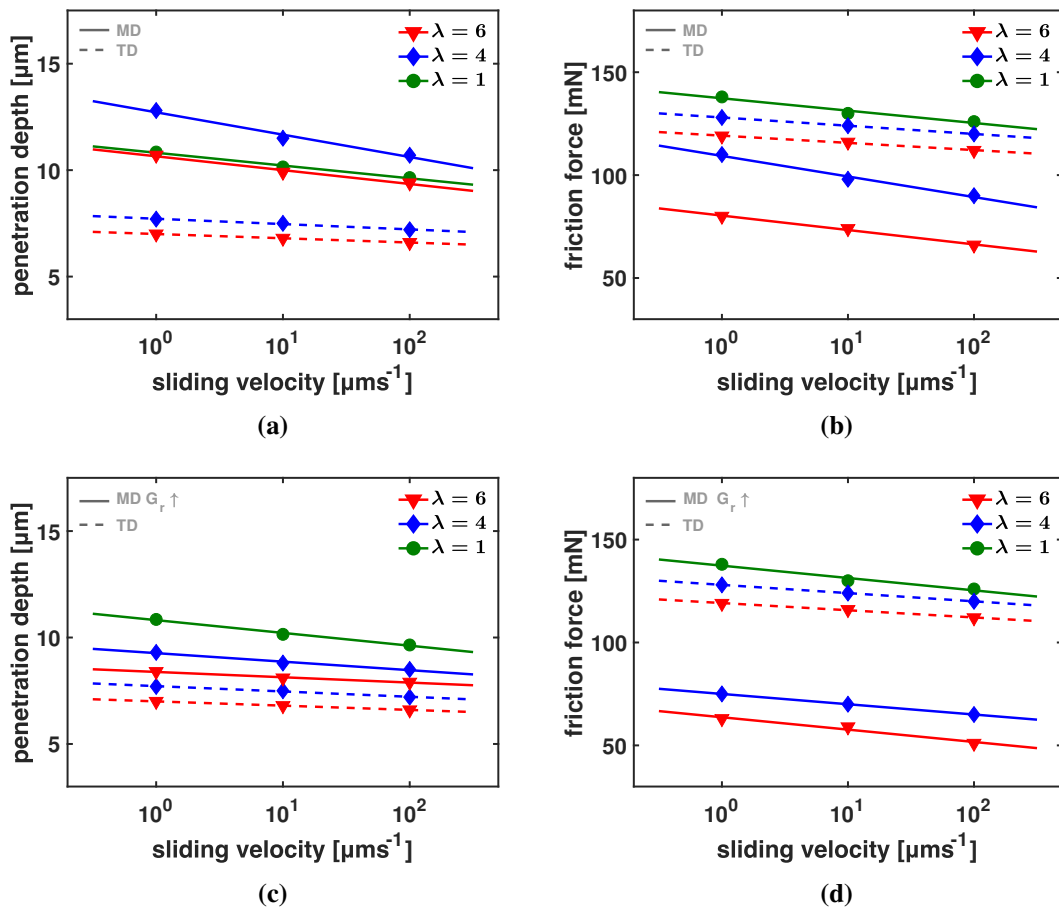


**Figure 5.6:** Scratch results using a  $50 \mu\text{m}$  tip and scratch velocities;  $1 \mu\text{m/s}$ ,  $10 \mu\text{m/s}$ , and  $100 \mu\text{m/s}$ ; (a) and (c) steady-state penetration depth values at various pre-stretch ratios, (b) and (d) steady-state friction force values at various pre-stretch ratios. A large value of strain hardening is used in MD simulations (c) and (d).

In order to visualize this analysis, a side and a top view of the scratch simulations are shown for different cases. Figure 5.7 shows the difference between the isotropic case and the anisotropic case at  $\lambda = 4$  in MD and TD. The images confirm the previous analysis; a large bow wave is formed in the TD due to the accumulation of the material in front of the tip and the obstruction of the sideways deformation, see Figure 5.7b. A bigger bow wave is observed in TD compared to the isotropic case in Figure 5.7a, moreover, less material is deformed sideways, this can be observed when looking at both the side and the top views. On the other hand, the bow wave is completely absent in MD with more material deforming on the sideways than TD and slightly less as compared to the isotropic case since no bow wave is formed, Figure 5.7c. Comparing the top views of Figures 5.7b and 5.7c shows that deformed elements in TD are more concentrated along



the centre of the scratch, whereas in MD the elements are more deformed to the sides. Figure 5.7d shows the displacement in z-direction of element 1 indicating the formation of bow wave, penetration depth and residual depth for all three cases. The percentage of elastic recovery for oriented surfaces is larger than that of the isotropic one. The area under the elastic portion of the stress–strain curve, i.e. resilience, is larger for oriented materials. This means material is able to absorb and store more elastic energy and release

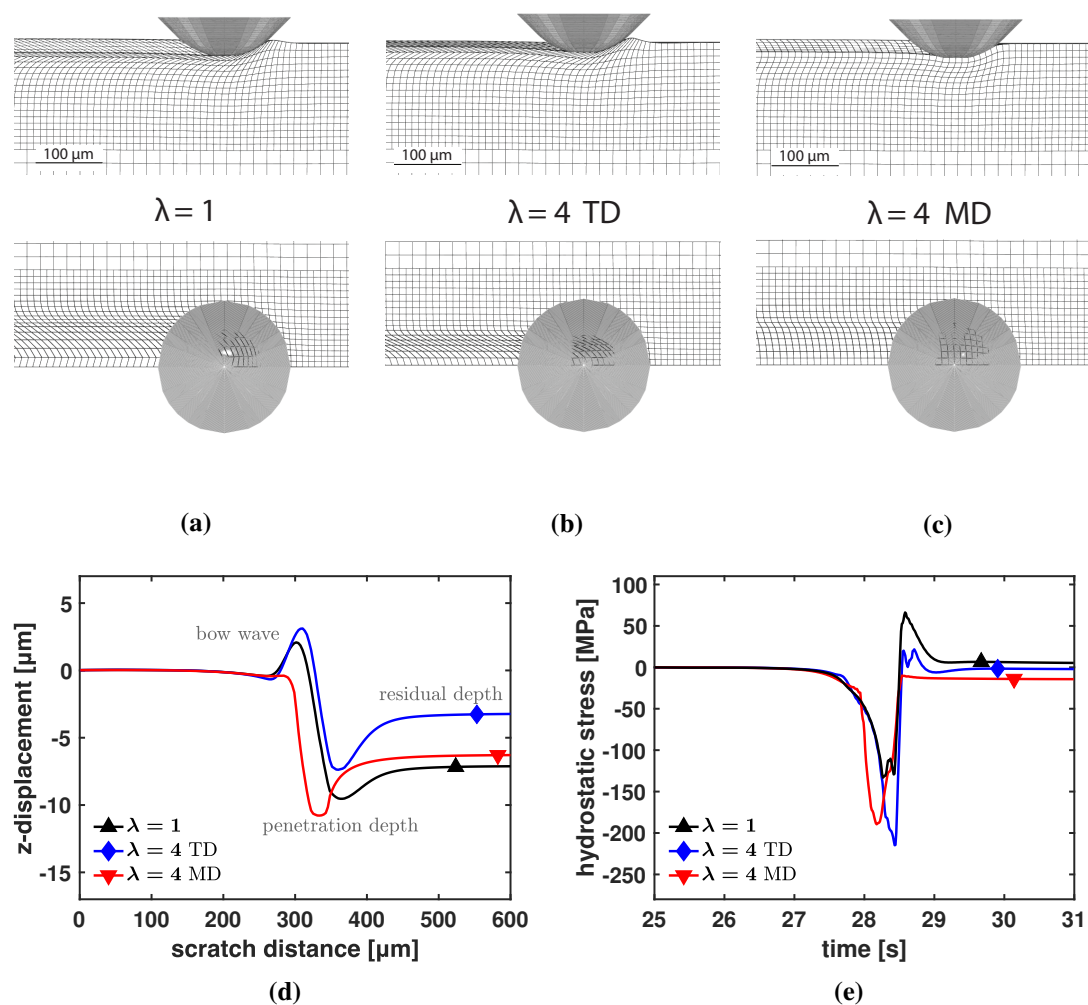


**Figure 5.7:** A top and a side view of single-asperity scratch simulations at 100  $\mu\text{m}/\text{s}$  on an (a) isotropic surface, (b) anisotropic surface with a pre-stretch of  $\lambda = 4$  in TD, (c) anisotropic surface with a pre-stretch of  $\lambda = 4$  in MD. (d) The displacement in z-direction of element 1 showing the formation of bow wave, penetration depth, and residual depth for the three cases. (e) The hydrostatic stress acting on element 1 during the scratch simulation, a higher negative hydrostatic stress is reached when scratching oriented surfaces in both MD and TD.

it upon unloading. This can also be explained via the hydrostatic stress acting on element 1 for all three cases. Hydrostatic stress is the mean normal stress acting on a body and is responsible for the volume change without taking a part in the permanent deformation. Figure 5.7e shows the value of the hydrostatic stress acting on element 1 in the isotropic, MD and TD cases. A larger value of negative hydrostatic stress is obtained in MD and TD since more energy is needed to compress the element in all directions. Once the compressed element passes the transition zone, i.e. unloading, this stress is released and elastic recovery takes place. In this respect, the difference between the steady-state penetration depth and the residual depth, i.e. recovery, is always higher for oriented surfaces. The same is observed experimentally [73]. Higher pre-stretch leads to a bigger bow wave in TD, see Figures 5.8a, 5.8b and 5.8d. As the anisotropy increases in MD, sideways deformation becomes harder when scratching in TD. This forces the material to accumulate more in front of the tip creating a bigger bow wave. To test the influence of the anisotropic shear parameters, all three shear parameters  $R_{12}$ ,  $R_{13}$  and  $R_{23}$  are set to 1, and scratch is performed in TD at  $\lambda = 4$ . This only leads to a larger bow wave since elements are easily sheared, compare the top views of Figures 5.8b and 5.8c. In Figure 5.9 the effect of pre-stretch in MD is displayed. The bow wave is completely absent for  $\lambda = 4$  and 6 and penetration is lowered as  $\lambda$  increases, see Figure 5.9a, 5.9b and 5.9d. As discussed earlier, pre-stretching increases strain hardening in MD. We manually increase the value of the strain hardening when scratching anisotropic surfaces in MD. The result is a significant decrease in penetration depth and less plastically deformed elements as show in Figure 5.9c.

The equivalent plastic strain  $\bar{\gamma}_p$  is selected as a physical criterion to assess the effect of orientation on surface damage. This criterion has been previously used by many researchers to assess damage formation on polymer and metal surfaces [31,89]. It has also been used in our previous work on iPP [113] and gave an accurate indication on damage formation on iPP surfaces at various normal loads, scratch speeds and iPP phases, i.e.  $\alpha$ -iPP and  $\beta$ -iPP. Figure 5.10 shows scratched isotropic and anisotropic surfaces with a pre-stretch of  $\lambda = 4$  and 6 in TD. Significantly more plastic deformation is observed on the anisotropic surfaces when scratched in TD. The obstruction of sideways deformation enhances the formation a large bow which in turn promotes more plastic deformation. Although higher magnitude of plastic deformation develops in TD compared to the isotropic surface, a larger scratch width is obtained in the isotropic case since the material is not obstructed to deform sideways. A small difference in plastic deformation is observed on the scratched surfaces in TD at  $\lambda = 4$  and 6. Although higher  $\lambda$  enhances larger bow wave, this is probably counteracted by less penetration into the surface due to higher yield and larger bow wave pushing the tip upwards. The magnitude of plastic deformation is delocalized on the isotropic surface since the material is free to deform equally in all direction. On the other hand, plastic deformation is concentrated along the

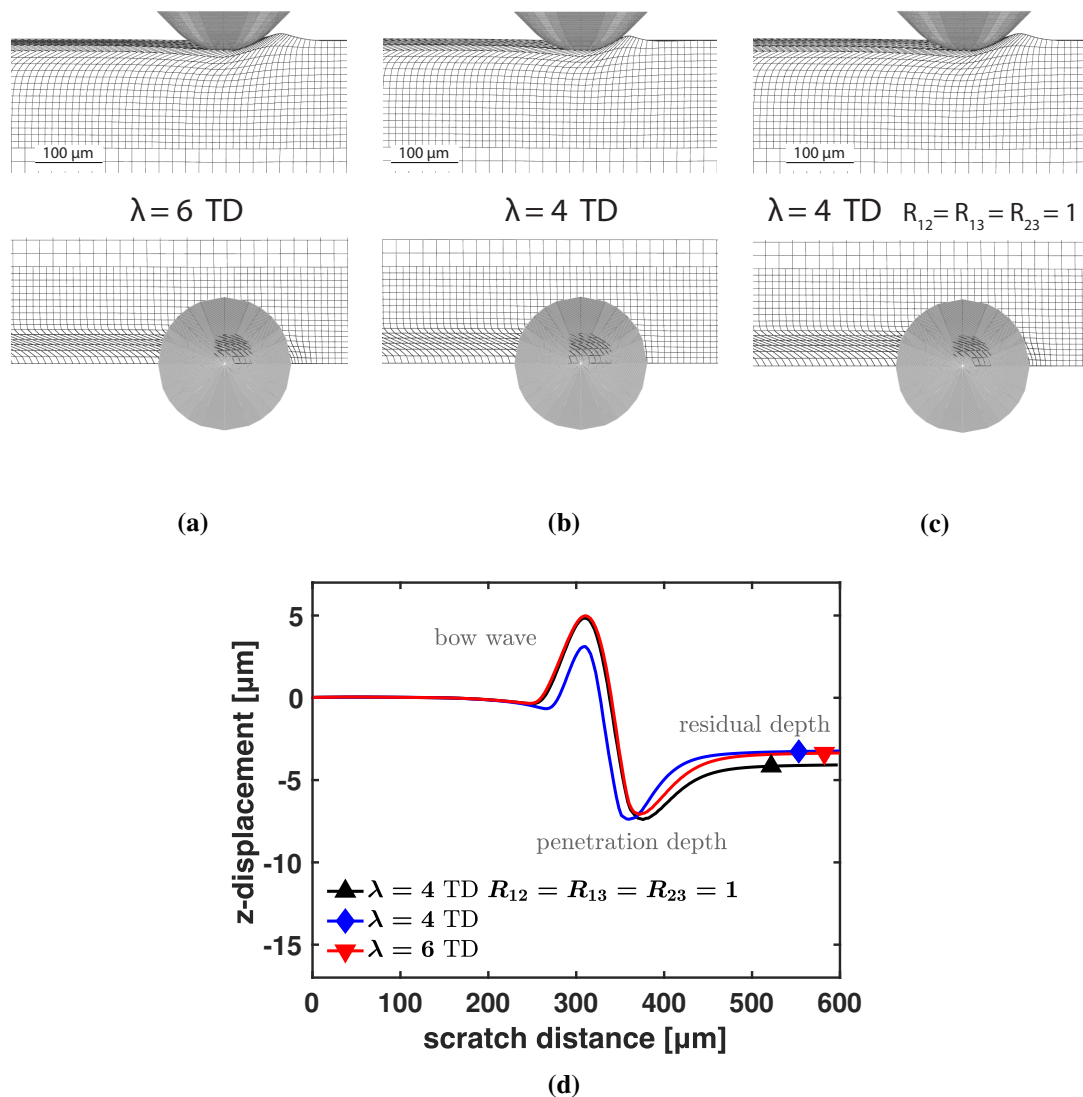


**Figure 5.8:** A top and a side view of single-asperity scratch simulations at 100 μm/s on an (a) anisotropic surface with a pre-stretch of  $\lambda = 6$  in TD, (b) anisotropic surface with a pre-stretch of  $\lambda = 4$  in TD, (c) anisotropic surface with a pre-stretch of  $\lambda = 4$  and  $R_{12} = 1$  in TD. (d) The displacement in z-direction of element 1 showing the formation of bow wave, penetration depth, and residual depth for the three cases.

centre of the scratched surface in TD since material is not constrained to deform along the scratch direction and obstructed sideways. Scratched surfaces in MD show a significantly lower magnitude of plastic deformation as opposed to TD, see Figure 5.11. At a given  $\lambda$ , a drop of 80 % in plastic deformation is achieved in MD compared to TD. The large drop is due to the complete absence of the bow wave in MD. The top image in Figure 5.11 shows the delocalization of plastic deformation from the centre of the scratch with slightly

more deformation observed on the sides. Higher anisotropy reduces plastic deformation by resisting surface penetration and bow wave formation. Strain hardening also plays a role in lowering permanent damage by resisting strain localization and stabilizing the deformation zones. This indicates that higher anisotropy and strain hardening in MD result in the least frictional resistance and an improved scratch-resistant surfaces.

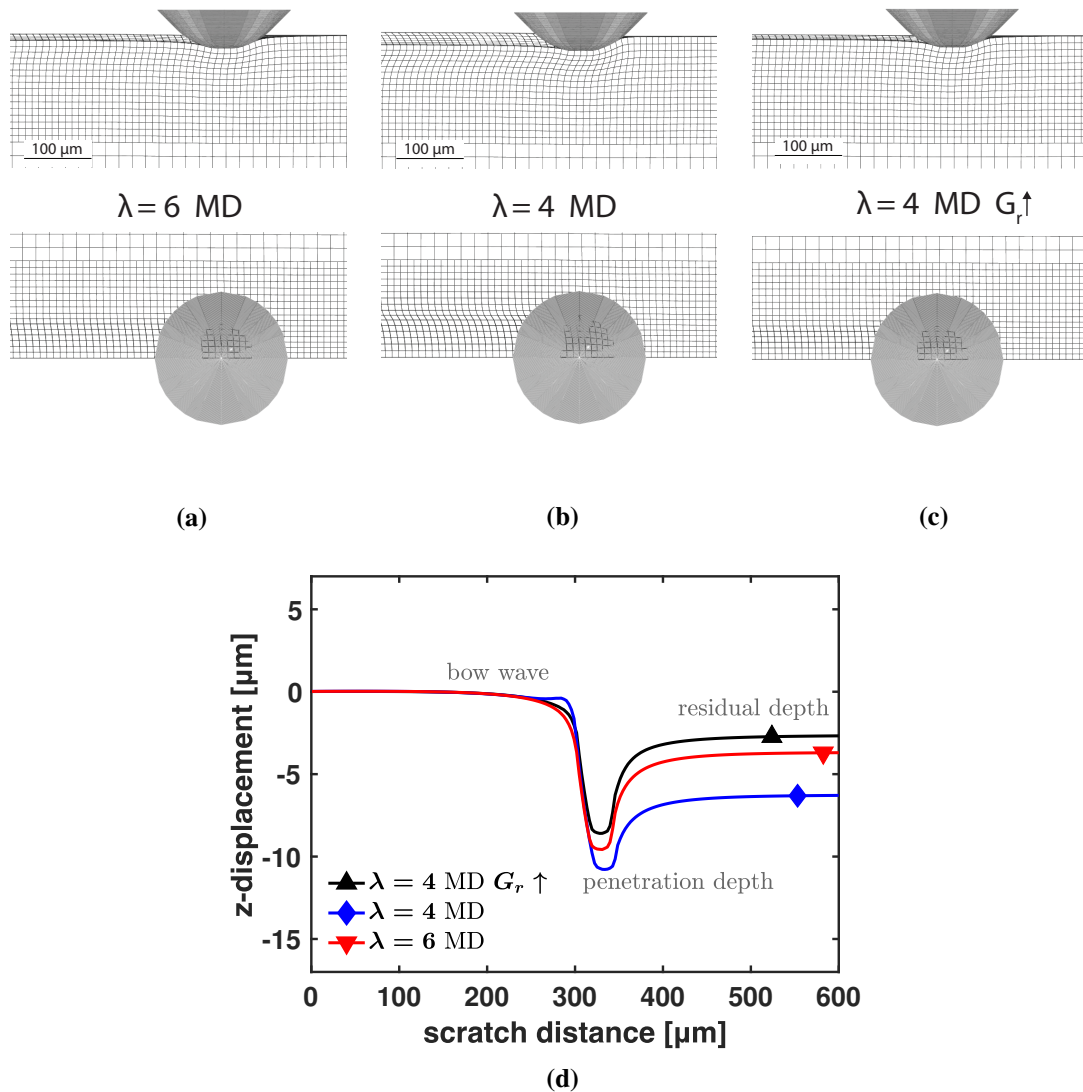


**Figure 5.9:** A top and a side view of single-asperity scratch simulations at 100 μm/s on an (a) anisotropic surface with a pre-stretch of  $\lambda = 6$  in MD, (b) anisotropic surface with a pre-stretch of  $\lambda = 4$  in MD, (c) anisotropic surface with a pre-stretch of  $\lambda = 4$  and a large value of strain hardening in MD. (d) The displacement in z-direction of element 1 showing the formation of bow wave, penetration depth, and residual depth for the three cases.

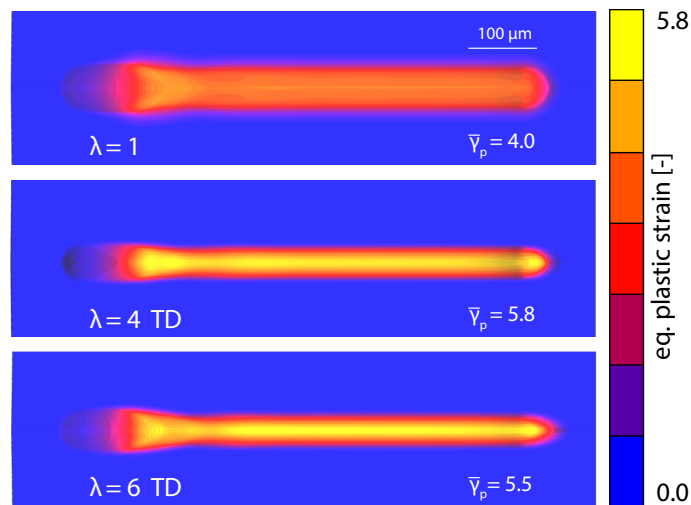


**Figure 5.10:** Scratched surfaces showing the resulting permanent deformation described by the equivalent plastic strain  $\bar{\gamma}_p$  on an isotropic and anisotropic surfaces with a pre-stretch of  $\lambda = 4$  and  $6$  in TD. Significantly more deformation is observed on the anisotropic surfaces when scratched in TD.

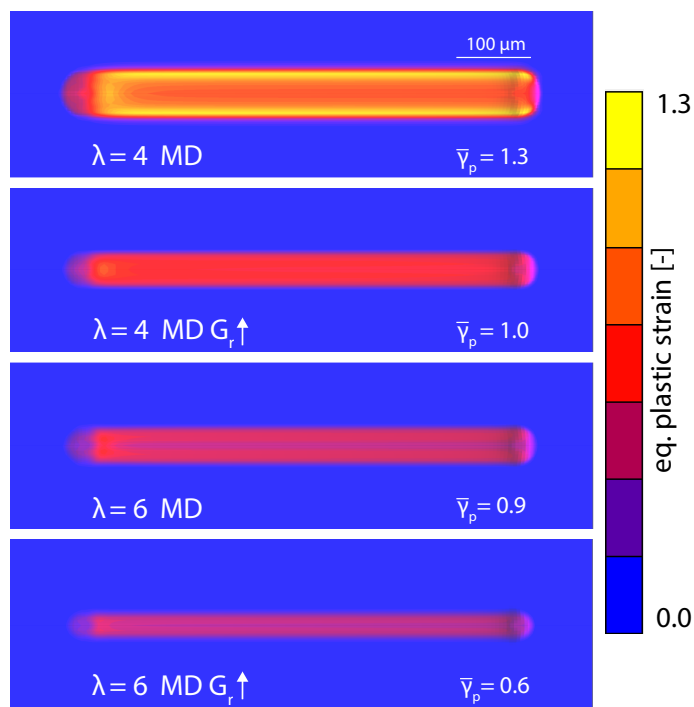


**Figure 5.11:** Scratched surfaces showing the resulting permanent deformation described by the equivalent plastic strain  $\bar{\gamma}_p$  on anisotropic surfaces with a pre-stretch of  $\lambda = 4$  and  $6$  in MD using different value of strain hardening. Significantly less deformation is observed on scratched surfaces in MD when the pre-stretch ratio or strain hardening increase.

## 5.4 Conclusions

Contact mechanics of anisotropic polypropylene surfaces is investigated via a developed 3D viscoelastic model implemented in FEM to simulate single asperity scratch tests. Anisotropy plays a major role in altering the scratch and frictional response of a scratched polymer surface.

At higher pre-stretch ratios  $\lambda$ , yield stress increases leading to lower penetration depth during indentation. Sliding in TD results in accumulation of material in front of the tip as a result of the obstruction of sideways deformations. This leads to an increase in frictional shear stress pushing the indenter upwards even more. However, the large bow wave developed in TD promotes plastic deformation to be more localized along the centre of the scratch. The frictional resistance and plastic deformation magnitudes in TD are comparable to those obtained when scratching an isotropic surface. The width of the scratch however is larger and delocalized on the isotropic surface since the material is free to deform sideways.

On the other hand, sliding in MD results in significantly lower frictional resistance since the formation of a bow wave is entirely absent as deformation along the scratch direction is obstructed. The absence of the bow wave leads to a low friction force. The tip is pushed upwards leaving the tip almost at the same penetration depth obtained after indentation. Significant rise in strain hardening takes place upon pre-stretching semi-crystalline polymers in MD, this is tested numerically via manually increasing the value of strain hardening in MD. The increased strain hardening leads to a lower penetration depth than the isotropic case by resisting strain localization.

Elastic recovery is enhanced on oriented surfaces due to their higher resilience, i.e. ability to store more elastic energy when loaded and release it upon unloading. This leads to a lower residual depth for oriented surfaces even when neglecting the effect of increased strain hardening in MD. A drop of 80 % in plastic deformation is achieved in MD compared to TD at a given  $\lambda$  thanks to the absence of the bow wave in MD. Scratching an oriented polymer surface in MD results in the least frictional resistance and the best scratch-resistant response.

The model provides qualitative measures of the effect of anisotropy on the scratch and frictional response of oriented polymers. It can be used as a tool to qualitatively assess surface damage while taking anisotropy into account. Orientation-dependent strain-hardening is not considered in our model and it is proven to play a major role in the scratch response of polymers in MD. It should be implemented in future work, however, proper characterization is very time consuming and goes beyond the scope of this study.



# Chapter 6

## Conclusions and Recommendations

### 6.1 Conclusions

This thesis discusses the thermo-mechanical and anisotropic aspects of polymers in contact. This is done via developing and implementing a 3D viscoelastic model in a Finite Element Modelling (FEM)-framework and use it as a tool to investigate such aspects and their influences. First, the effects of temperature on the tribological properties of polycarbonate is studied. Then, contact mechanics of isotropic polypropylene surfaces is investigated using a thermo-mechanical model. Finally, an indication on how anisotropy can alter the frictional response of these surfaces upon scratching is provided.

The main conclusions of this work are:

*Temperature dependent two-body abrasive wear of polycarbonate surfaces (Chapter 2)*

- Higher temperatures lower the yield stress of polycarbonate and alter the post-yield response, i.e. less strain softening and strain hardening. This behaviour leads to the formation of localized plastic deformation zones which enhances the formation of cracks. Moreover, the increased adhesion at high temperatures facilitates the formation of a bow wave in front of the sliding tip and leads to a less smooth stick-slip transition which in turn enhances crack formation.
- The FEM model implemented is able to separately quantify the effects of the altered intrinsic response and the increased adhesion on crack formation. This is done via selecting a critical positive hydrostatic stress value as a criterion for crack initiation on polycarbonate surfaces. It has been shown that at elevated temperatures 75%



of the increase in the maximum positive hydrostatic stress results solely from the altered intrinsic response, and 25% results from the change in the polymer-tip interaction, i.e. increased adhesion.

#### *Modelling of scratching on an isotropic polypropylene surface (Chapter 3)*

- A thermo-mechanical model is necessary to quantitatively predict the intrinsic response of iPP, especially at higher strain rates, where heat is produced due the plastic deformation. The difference in the intrinsic response of  $\alpha$ -iPP and  $\beta$ -iPP plays a major role in the resulting scratch and frictional response. In this respect,  $\beta$ -iPP exhibits a slightly higher strain-rate dependence than  $\alpha$ -iPP. This leads to lower penetration depth and friction force at relatively high deformation rates. This makes  $\beta$ -iPP a favourable choice for applications which involves high-speed sliding and rolling such as bearings. Moreover, the significantly higher strain hardening of  $\beta$ -iPP compared to  $\alpha$ -iPP resists the localized plastic deformation zones and the build-up of material in front of the tip leading to less plastically deformed material along the scratch direction. This makes  $\beta$ -iPP, again, a generally favourable choice over  $\alpha$ -iPP for applications that require enhanced wear resistance.
- The stick-slip phenomenon is mainly responsible for the damage mechanism observed on iPP surfaces. This phenomenon becomes more pronounced when the tip penetrates deep into the polymer, which introduces additional material build-up in front of the tip. Increased normal loads and lowered scratch speeds lead to more tip penetration, thus, stick-slip becomes more severe. As a result, the material is more plastically deformed along the scratch direction and the fish-scale damage pattern is clearly observed. The FEM model is able to indicate the magnitude of the damage by using the equivalent plastic strain,  $\bar{\gamma}_p$ , as a physical criterion to assess this damage at a given normal load and scratch speed applied on a given iPP surface, i.e.  $\alpha$ -iPP or  $\beta$ -iPP.

#### *Uniaxial and biaxial response of anisotropic polypropylene (Chapter 4)*

- The developed EGP model accounts for anisotropy by incorporating Hill's yield function and an associated anisotropic viscoplastic flow rule. The model is able to quantitatively predict the yield values of iPP at a given stretch ratio and orientation angle while taking strain-rate dependency into account. Moreover, the associated flow rule is able to indicate the directional magnitude of deformation rates for isotropic and anisotropic cases upon biaxial stretching.

*Modelling of scratching on an anisotropic polypropylene surface (Chapter 5)*

- Upon scratching iPP surfaces, anisotropy plays a major role in altering the scratch and frictional response. At higher pre-stretch ratios  $\lambda$ , the yield stress of semi-crystalline polymers increases leading to lower penetration depth during indentation. The direction of scratching with respect to the pre-stretch direction has a significant influence of the deformation mechanics. Upon sliding on an iPP surface perpendicular to the pre-stretch direction, i.e. transverse direction (TD), the obstruction of sideways deformations enhances the formation of bow wave in front of the tip pushing the indenter upwards. Although frictional resistance and plastic deformation magnitudes in TD are comparable to those obtained when scratching an isotropic surface, the width of the scratch is smaller and localized in TD since the material deformation is obstructed sideways.
- Sliding on an iPP surface along the pre-stretch direction, i.e. machine direction (MD), results in a significantly lower frictional resistance since the formation of a bow wave is entirely absent as deformation along the scratch direction is obstructed. The absence of the bow wave leads to low friction force to push the tip upwards leaving the tip almost at the same penetration depth obtained after indentation. Experimentally, a significant rise in strain hardening in MD takes place upon pre-stretching semi-crystalline polymers, this is tested numerically via manually increasing the value of strain hardening in MD. The additional introduced strain hardening leads to lower penetration depth than the isotropic case by resisting strain localization, however, higher depth than TD due to the complete absence of the bow wave in case of MD. A drop of 80 % in plastic deformation is achieved in MD compared to TD at a given  $\lambda$  thanks to the absence of the bow wave in MD. Scratching an oriented polymer surface in MD results in the most enhanced scratch-resistance.
- Elastic recovery of iPP is enhanced on oriented surfaces due to their higher resilience, i.e. ability to store more elastic energy when loaded and release it upon unloading. This leads to lower residual depth for oriented surfaces even when neglecting the effect of increased strain hardening in MD.
- As a general conclusion, increased strain hardening, higher strain-rate dependence, and pre-stretching surfaces in MD enhance the tribological response of polymers as far as scratch and/or wear-resistance are concerned.

## 6.2 Recommendations

The developed model in this study provides a solid basis for predicting the scratch and frictional response of polymers upon scratching while accounting for temperature, thermo-mechanical behaviour and mechanical anisotropy. There are some subjects worth studying and a number of points to be resolved.

- In the first chapter, a critical positive hydrostatic stress value is selected as a criterion for crack initiation on polycarbonate surfaces. We assumed that this value is independent of temperature, however, it is plausible that this value changes as temperature increases due to the increase in molecular mobility.
- The effect of increasing temperature on the scratch and frictional response of polycarbonate is not substantial thanks to its high strain hardening even at relatively high temperatures. It is suggested to study the effect of increasing temperature on the scratch and frictional response of polymers which exhibit low strain hardening such as polystyrene. It is expected, due to the lack of strain hardening, that temperature has a more pronounced effect.
- In order to quantify the temperature rise due to plastic deformation and compare it with simulations, measuring the temperature of iPP surfaces during scratching is an interesting idea. The temperature can be measured via infrared thermal imaging. It should be noted however that thermal imaging has a spatial resolution of around  $5\ \mu\text{m}$ , which is slightly larger than some features of the scratch experiment, e.g. the bow wave. In order to obtain accurate data, it would be more practical to use infrared thermal imaging when using an indenter of  $100+\ \mu\text{m}$  tip radius. In that respect, downscaling can then be used to make predictions at smaller scales.
- A thermo-mechanically coupled model has been developed based on the heat produced due to the plastic deformation which alters the post-yield response. However, the model does not account for the friction-induced heat. The friction-induced heat is the thermal energy generated due to the work done by the frictional force, in other words, the work done to overcome friction. A frictionless case would produce no heat due to friction but can still produce heat due to plastic deformation. The amount of heat generated due to friction depends on the friction coefficient between the two surfaces in contact which in case of scratching depends on the material of the indenter and the polymer. As mentioned in the introduction, friction and associated phenomena can be further investigated via molecular dynamic simulations.

- Orientation-dependent strain-hardening plays a major role in the scratch response of oriented polymers in MD [73]. Unlike metals where strain hardening is associated with an increase in the density of dislocations, in polymers this phenomenon is provided by stretching the amorphous network and the crystalline structure. It is necessary to include the orientation-dependent strain-hardening in our model in order to obtain quantitative measures on the effect of anisotropy on the scratch and frictional response of oriented polymers.
- The evolution of anisotropy is a great addition if one needs to model the response of polymers at relatively large plastic deformations. Upon plastically deforming anisotropic polymers, the state of orientation changes and the anisotropy directions rotate with respect to their initial configuration. Such an addition might need input from a micro-mechanical model in order to quantify this change.
- The model faced some numerical errors as its complexity increased. An explicit Euler scheme was used for the numerical integration of the evolution equation. This often resulted in numerical errors especially during scratch simulations. A higher-order method, i.e. Runge–Kutta, was used in some cases. In addition, adaptive time-stepping was employed to control the abrupt changes in certain model variables upon deformation. Adding more complexity to the model may lead to more numerical problems. Therefore, it is recommended to carefully develop the model and to consider more advanced numerical techniques, if necessary, to avoid errors.



# References

- [1] L. C. A. van Breemen, L. E. Govaert, and H. E. H. Meijer. Scratching polycarbonate: A quantitative model. *Wear*, 274-275:238–247, 2012.
- [2] S. Krop, H. E. H. Meijer, and L. C. A. van Breemen. Finite element modeling and experimental validation of single-asperity sliding friction of diamond against reinforced and non-filled polycarbonate. *Wear*, 356-357:77–85, 2016.
- [3] K. Holmberg. Reliability aspects of tribology. *Tribology International*, 34(12):801–808, 2001.
- [4] D. Dowson. *History of tribology*. Addison-Wesley Longman Limited, 1979.
- [5] G. Amontons. *De la resistance causée dans des machines, tant par les frottements des parties que les composent, que par la roideur des cordes qu'on y employe, et la maniere de calculer l'un e l'autre*. Paris, 1699.
- [6] C. A. Coulomb. *Théorie des machines simples en ayant égard au frottement de leurs parties et à la roideur des cordages*. Bachelier, 1821.
- [7] J. F. Archard. Elastic deformation and the laws of friction. *Proceedings of the Royal Society of London. Series A. Mathematical and Physical Sciences*, 243(1233):190–205, 1957.
- [8] F. P. Bowden, A. J. W. Moore, and D. Tabor. The ploughing and adhesion of sliding metals. *Journal of Applied Physics*, 14(2):80–91, 1943.
- [9] J. A. Greenwood and J. B. P. Williamson. Contact of nominally flat surfaces. *Proceedings of the royal society of London. Series A. Mathematical and physical sciences*, 295(1442):300–319, 1966.
- [10] J. A. Greenwood and J. J. Wu. Surface roughness and contact: an apology. *Meccanica*, 36(6):617–630, 2001.
- [11] B. Bhushan. Nanoscale tribophysics and tribomechanics. *Wear*, 225:465–492, 1999.
- [12] L. Zhang and H. Tanaka. Towards a deeper understanding of wear and friction on the atomic scale—a molecular dynamics analysis. *Wear*, 211(1):44–53, 1997.
- [13] A. Matthews, S. Franklin, and K. Holmberg. Tribological coatings: contact mechanisms and selection. *Journal of Physics D: Applied Physics*, 40(18):5463, 2007.
- [14] B. J. Briscoe, P. D. Evans, S. K. Biswas, and S. K. Sinha. The hardnesses of poly(methylmethacrylate). *Tribology International*, 29(2):93–104, 1996.
- [15] B. J. Briscoe, E. Pelillo, and S. K. Sinha. Scratch hardness and deformation maps for polycarbonate and polyethylene. *Polymer Engineering and Science*, 36(24):2996–3005, 1996.
- [16] B. J. Briscoe. Isolated contact stress deformations of polymers: The basis for interpreting polymer tribology. *Tribology International*, 31(1-3):121–126, 1998.
- [17] B. J. Briscoe and S. K. Sinha. Wear of polymers. *Proceedings of the Institution of Mechanical Engineers, Part J: Journal of Engineering Tribology*, 216(6):401–413, 2002.
- [18] F. P. Bowden and D. Tabor. Friction, lubrication and wear: A survey of work during the last decade. *British Journal of Applied Physics*, 17(12):1521–1544, 1966.

- [19] M. C. Boyce, D. M. Parks, and A. S. Argon. Large inelastic deformation of glassy polymers. part i: rate dependent constitutive model. *Mechanics of Materials*, 7(1):15–33, 1988.
- [20] A. E. Giannakopoulos, P.-L. Larsson, and R. Vestergaard. Analysis of vickers indentation. *International Journal of Solids and Structures*, 31(19):2679–2708, 1994.
- [21] P.-L. Larsson, A. E. Giannakopoulos, E. Söderlund, D. J. Rowcliffe, and R. Vestergaard. Analysis of berkovich indentation. *International Journal of Solids and Structures*, 33(2):221–248, 1996.
- [22] L. Anand and N. M. Ames. On modeling the micro-indentation response of an amorphous polymer. *International Journal of Plasticity*, 22(6):1123–1170, 2006.
- [23] L. C. A. van Breemen, T. A. P. Engels, C. G. N. Pelletier, L. E. Govaert, and J. M. J. den Toonder. Numerical simulation of flat-tip micro-indentation of glassy polymers: Influence of loading speed and thermodynamic state. *Philosophical Magazine*, 89(8):677–696, 2009.
- [24] S. Leroch, M. Varga, S. J. Eder, A. Vernes, M. R. Ripoll, and G. Ganzenmüller. Smooth particle hydrodynamics simulation of damage induced by a spherical indenter scratching a viscoplastic material. *International Journal of Solids and Structures*, 81:188–202, 2016.
- [25] M. Varga, S. Leroch, S. J. Eder, H. Rojacz, and M. R. Ripoll. Influence of velocity on high-temperature fundamental abrasive contact: A numerical and experimental approach. *Wear*, 426:370–377, 2019.
- [26] J. H. Lee, G. H. Xu, and H. Liang. Experimental and numerical analysis of friction and wear behavior of polycarbonate. *Wear*, 250-251(2):1541–1556, 2001.
- [27] C. Gauthier, S. Lafaye, and R. Schirrer. Elastic recovery of a scratch in a polymeric surface: Experiments and analysis. *Tribology International*, 34(7):469–479, 2001.
- [28] J.L. Bucaille, C. Gauthier, E. Felder, and R. Schirrer. The influence of strain hardening of polymers on the piling-up phenomenon in scratch tests: Experiments and numerical modelling. *Wear*, 260(7-8):803–814, 2006.
- [29] H. Jiang, G. T. Lim, J. N. Reddy, J. D. Whitcomb, and H.-J. Sue. Finite element method parametric study on scratch behavior of polymers. *Journal of Polymer Science, Part B: Polymer Physics*, 45(12):1435–1447, 2007.
- [30] N. Aleksy, G. Kermouche, A. Vautrin, and J. M. Bergheau. Numerical study of scratch velocity effect on recovery of viscoelastic-viscoplastic solids. *International Journal of Mechanical Sciences*, 52(3):455–463, 2010.
- [31] H. Pelletier, C. Gauthier, and R. Schirrer. Influence of the friction coefficient on the contact geometry during scratch onto amorphous polymers. *Wear*, 268(9-10):1157–1169, 2010.
- [32] Z. Wang, P. Gu, H. Zhang, Z. Zhang, and X. Wu. Finite element modeling of the indentation and scratch response of epoxy/silica nanocomposites. *Mechanics of Advanced Materials and Structures*, 21(10):802–809, 2014.
- [33] M. M. Hossain, R. Minkwitz, P. Charoensirisomboon, and H.-J. Sue. Quantitative modeling of scratch-induced deformation in amorphous polymers. *Polymer*, 55(23):6152–6166, 2014.
- [34] B. Feng and Z. Chen. Tribology behavior during indentation and scratch of thin films on substrates: Effects of plastic friction. *AIP Advances*, 5(5):057152, 2015.
- [35] J. Zhang, H. Jiang, C. Jiang, G. Kang, Q. Kan, and Y. Li. Experimental and numerical investigations of evaluation criteria and material parameters’ coupling effect on polypropylene scratch. *Polymer Engineering & Science*, 58(1):118–122, 2018.
- [36] R. N. Haward and G. Thacray. Use of a mathematical model to describe isothermal stress-strain curves in glassy thermoplastics. *Proceedings of the Royal Society of London Series*, 302(1471):453–472, 1968.

- [37] T. A. Tervoort, E. T. J. Klompen, and L. E. Govaert. A multi-mode approach to finite, three-dimensional, nonlinear viscoelastic behavior of polymer glasses. *Journal of Rheology*, 40(5):779–797, 1996.
- [38] T. A. Tervoort, R. J. M. Smit, W. A. M. Brekelmans, and L. E. Govaert. A constitutive equation for the elasto-viscoplastic deformation of glassy polymers. *Mechanics Time-Dependent Materials*, 1(3):269–291, 1997.
- [39] L. E. Govaert, P. H. M. Timmermans, and W. A. M. Brekelmans. The influence of intrinsic strain softening on strain localization in polycarbonate: Modeling and experimental validation. *Journal of Engineering Materials and Technology, Transactions of the ASME*, 122(2):177–185, 2000.
- [40] L. C. A. van Breemen, E. T. J. Klompen, L. E. Govaert, and H. E. H. Meijer. Extending the EGP constitutive model for polymer glasses to multiple relaxation times. *Journal of the Mechanics and Physics of Solids*, 59(10):2191–2207, 2011.
- [41] T. A. P. Engels, L. E. Govaert, and H. E. H. Meijer. The influence of molecular orientation on the yield and post-yield response of injection-molded polycarbonate. *Macromolecular Materials and Engineering*, 294(12):821–828, 2009.
- [42] L. C. A. van Breemen, T. A. P. Engels, E. T. J. Klompen, D. J. A. Senden, and L. E. Govaert. Rate- and temperature-dependent strain softening in solid polymers. *Journal of Polymer Science Part B: Polymer Physics*, 50(24):1757–1771, 2012.
- [43] E. T. J. Klompen, T. A. P. Engels, L. E. Govaert, and H. E. H. Meijer. Modeling of the postyield response of glassy polymers: Influence of thermomechanical history. *Macromolecules*, 38(16):6997–7008, 2005.
- [44] T. A. P. Engels, B. A. G. Schrauwen, L. E. Govaert, and H. E. H. Meijer. Improvement of the long-term performance of impact-modified polycarbonate by selected heat treatments. *Macromolecular Materials and Engineering*, 294(2):114–121, 2009.
- [45] H. G. H. van Melick, L. E. Govaert, and H. E. H. Meijer. Localisation phenomena in glassy polymers: Influence of thermal and mechanical history. *Polymer*, 44(12):3579–3591, 2003.
- [46] H. E. H. Meijer and L. E. Govaert. Mechanical performance of polymer systems: The relation between structure and properties. *Progress in Polymer Science*, 30(8-9):915–938, 2005.
- [47] D. J. A. Senden, S. Krop, J. A. W. van Dommelen, and L. E. Govaert. Rate- and temperature-dependent strain hardening of polycarbonate. *Journal of Polymer Science, Part B: Polymer Physics*, 50(24):1680–1693, 2012.
- [48] C. Bauwens-Crowet, J.-C. Bauwens, and G. Homès. The temperature dependence of yield of polycarbonate in uniaxial compression and tensile tests. *Journal of Materials Science*, 7(2):176–183, 1972.
- [49] *MSC Software MSC Marc: Element Library Volume B*, MSC Software GmbH, 2014.
- [50] G. Wróbel and M. Szymiczek. Influence of temperature on friction coefficient of low density polyethylene. *Journal of Achievements in Materials and Manufacturing Engineering*, 28(1):31–34, 2008.
- [51] T. A. P. Engels, L. C. A. van Breemen, L. E. Govaert, and H. E. H. Meijer. Criteria to predict the embrittlement of polycarbonate. *Polymer*, 52(8):1811–1819, 2011.
- [52] R. P. Nimmer and J. T. Woods. Investigation of brittle failure in ductile, notch-sensitive thermoplastics. *American Society of Mechanical Engineers, Materials Division*, 29:129–148, 1991.
- [53] S. F. S. P. Looijmans, V. G. de Bie, P. D. Anderson, and L. C. A. van Breemen. Hydrostatic stress as indicator for wear initiation in polymer tribology. *Wear*, 426-427:1026–1032, 2019.
- [54] K.-H. Zum Gahr. *Microstructure and wear of materials*, volume 10. Elsevier, 1987.



- [55] M. Varga, S. Leroch, S. J. Eder, and M. Rodríguez Ripoll. Meshless microscale simulation of wear mechanisms in scratch testing. *Wear*, 376:1122–1129, 2017.
- [56] L. C. A. van Breemen, T. A. P. Engels, E. T. J. Klompen, D. J. A. Senden, and L. E. Govaert. Rate- and temperature-dependent strain softening in solid polymers. *Journal of Polymer Science, Part B: Polymer Physics*, 50(24):1757–1771, 2012.
- [57] E. M. Arruda and M. C. Boyce. Evolution of plastic anisotropy in amorphous polymers during finite straining. *International Journal of Plasticity*, 9(6):697–720, 1993.
- [58] C. P. Buckley and D. C. Jones. Glass-rubber constitutive model for amorphous polymers near the glass transition. *Polymer*, 36(17):3301–3312, 1995.
- [59] C. P. Buckley, P. J. Dooling, J. Harding, and C. Ruiz. Deformation of thermosetting resins at impact rates of strain. part 2: Constitutive model with rejuvenation. *Journal of the Mechanics and Physics of Solids*, 52(10):2355–2377, 2004.
- [60] D. S. A. De Focatiis, J. Embery, and C. P. Buckley. Large deformations in oriented polymer glasses: Experimental study and a new glass-melt constitutive model. *Journal of Polymer Science, Part B: Polymer Physics*, 48(13):1449–1463, 2010.
- [61] E. Oral, K. K. Wannomae, N. Hawkins, W. H. Harris, and O. K. Muratoglu.  $\alpha$ -tocopherol-doped irradiated UHMWPE for high fatigue resistance and low wear. *Biomaterials*, 25(24):5515–5522, 2004.
- [62] O. K. Muratoglu, C. R. Bragdon, D. O. O’Connor, M. Jasty, W. H. Harris, G. Rizwan, and F. McGarry. Unified wear model for highly crosslinked ultra-high molecular weight polyethylenes (UHMWPE). *Biomaterials*, 20(16):1463–1470, 1999.
- [63] F. Renò and M. Cannas. UHMWPE and vitamin E bioactivity: An emerging perspective. *Biomaterials*, 27(16):3039–3043, 2006.
- [64] S. A. Atwood, D. W. van Citters, E. W. Patten, J. Furmanski, M. D. Ries, and L. A. Pruitt. Tradeoffs amongst fatigue, wear, and oxidation resistance of cross-linked ultra-high molecular weight polyethylene. *Journal of the Mechanical Behavior of Biomedical Materials*, 4(7):1033–1045, 2011.
- [65] J. Fu, B. W. Ghali, A. J. Lozynsky, E. Oral, and O. K. Muratoglu. Wear resistant UHMWPE with high toughness by high temperature melting and subsequent radiation cross-linking. *Polymer*, 52(4):1155–1162, 2011.
- [66] A. Keller and M. J. Machin. Oriented crystallization in polymers. *Journal of Macromolecular Science, Part B*, 1(1):41–91, 1967.
- [67] T. B. van Erp, C. T. Reynolds, T. Peijs, J. A. W. van Dommelen, and L. E. Govaert. Prediction of yield and long-term failure of oriented polypropylene: Kinetics and anisotropy. *Journal of Polymer Science, Part B: Polymer Physics*, 47(20):2026–2035, 2009.
- [68] T. B. van Erp, D. Cavallo, G. W. M. Peters, and L. E. Govaert. Rate-, temperature-, and structure-dependent yield kinetics of isotactic polypropylene. *Journal of Polymer Science, Part B: Polymer Physics*, 50(20):1438–1451, 2012.
- [69] H. J. M. Caelers, L. E. Govaert, and G. W. M. Peters. The prediction of mechanical performance of isotactic polypropylene on the basis of processing conditions. *Polymer*, 83:116–128, 2016.
- [70] H. J. M. Caelers, E. M. Troisi, L. E. Govaert, and G. W. M. Peters. Deformation-induced phase transitions in iPP polymorphs. *Polymers*, 9(10):547, 2017.
- [71] H. J. M. Caelers, E. Parodi, D. Cavallo, G. W. M. Peters, and L. E. Govaert. Deformation and failure kinetics of iPP polymorphs. *Journal of Polymer Science, Part B: Polymer Physics*, 55(9):729–747, 2017.

- [72] W. M. Gao, L. Wang, J. K. Coffey, and F. Daver. Finite element simulation of scratch on polypropylene panels. *Materials & Design*, 140:400–408, 2018.
- [73] S. F. S. P. Looijmans, P. D. Anderson, and L. C. A. van Breemen. Contact mechanics of isotactic polypropylene: Effect of pre-stretch on the frictional response. *Wear*, 398:183–190, 2018.
- [74] G. W. Adams and R. J. Farris. Latent energy of deformation of bisphenol a polycarbonate. *Journal of Polymer Science Part B: Polymer Physics*, 26(2):433–445, 1988.
- [75] M. C. Boyce, E. L. Montagut, and A. S. Argon. The effects of thermomechanical coupling on the cold drawing process of glassy polymers. *Polymer Engineering & Science*, 32(16):1073–1085, 1992.
- [76] E. T. J. Klompen. *Mechanical properties of solid polymers : constitutive modelling of long and short term behaviour*. PhD thesis, Eindhoven University of Technology, 2005.
- [77] H. Jiang, R. Browning, and H.-J. Sue. Understanding of scratch-induced damage mechanisms in polymers. *polymer*, 50(16):4056–4065, 2009.
- [78] C. Xiang, H.-J. Sue, J. Chu, and B. Coleman. Scratch behavior and material property relationship in polymers. *Journal of Polymer Science Part B: Polymer Physics*, 39(1):47–59, 2001.
- [79] M. Wong, G. T. Lim, A. Moyse, J. N. Reddy, and H.-J. Sue. A new test methodology for evaluating scratch resistance of polymers. *Wear*, 256(11-12):1214–1227, 2004.
- [80] H. Jiang, Q. Cheng, C. Jiang, J. Zhang, and L. Yonghua. Effect of stick-slip on the scratch performance of polypropylene. *Tribology International*, 91:1–5, 2015.
- [81] R. A. Duckett, S. Rabinowitz, and I. M. Ward. The strain-rate, temperature and pressure dependence of yield of isotropic poly (methylmethacrylate) and poly (ethylene terephthalate). *Journal of Materials Science*, 5(10):909–915, 1970.
- [82] S. Rabinowitz, I. M. Ward, and J. S. C. Parry. The effect of hydrostatic pressure on the shear yield behaviour of polymers. *Journal of Materials science*, 5(1):29–39, 1970.
- [83] R. A. Duckett, B. C. Goswami, L. S. A. Smith, and A. M. Ward, I. M. and Zihlif. The yielding and crazing behaviour of polycarbonate in torsion under superposed hydrostatic pressure. *British Polymer Journal*, 10(1):11–16, 1978.
- [84] T. Ree and H. Eyring. Theory of non-Newtonian flow. i. solid plastic system. *Journal of Applied Physics*, 26(7):793–800, 1955.
- [85] J. A. Roetling. Yield stress behaviour of isotactic polypropylene. *Polymer*, 7(7):303 – 306, 1966.
- [86] E. H. Lee. Elastic-plastic deformation at finite strains. *Journal of applied mechanics*, 36(1):1–6, 1969.
- [87] J.F. Besseling and E. van der Giessen. *Mathematical modeling of inelastic deformation*, volume 5. CRC Press, 1994.
- [88] H. Ziegler. *An introduction to thermomechanics*, volume 21. Elsevier, 2012.
- [89] S. C. Bellemare, M. Dao, and S. Suresh. Effects of mechanical properties and surface friction on elasto-plastic sliding contact. *Mechanics of Materials*, 40(4-5):206–219, 2008.
- [90] D. J. A. Senden, G. W. M. Peters, L. E. Govaert, and J. A. W. van Dommelen. Anisotropic yielding of injection molded polyethylene: Experiments and modeling. *Polymer*, 54(21):5899–5908, 2013.
- [91] S. F. S. P. Looijmans, P. D. Anderson, and L. C. A. van Breemen. Contact mechanics of high-density polyethylene: Effect of pre-stretch on the frictional response and the onset of wear. *Wear*, 410:142–148, 2018.
- [92] J. M. Andrews and I. M. Ward. The cold-drawing of high density polyethylene. *Journal of materials science*, 5(5):411–417, 1970.
- [93] A. G. Gibson, I. M. Ward, B. N. Cole, and B. Parsons. Hydrostatic extrusion of linear polyethylene. *Journal of Materials Science*, 9(7):1193–1196, 1974.

- [94] K. Nakayama and H. Kanetsuna. Hydrostatic extrusion of solid polymers. *Journal of Materials Science*, 10(7):1105–1118, 1975.
- [95] Z. Bartczak, J. Morawiec, and A. Galeski. Deformation of high-density polyethylene produced by rolling with side constraints. ii. mechanical properties of oriented bars. *Journal of applied polymer science*, 86(6):1405–1412, 2002.
- [96] A. Keller and J. G. Rider. On the tensile behaviour of oriented polyethylene. *Journal of Materials Science*, 1(4):389–398, 1966.
- [97] N. Brown, R. A. Duckett, and I. M. Ward. The yield behaviour of oriented polyethylene terephthalate. *Philosophical Magazine*, 18(153):483–502, 1968.
- [98] C. Bridle, A. Buckley, and J. Scanlan. Mechanical anisotropy of oriented polymers. *Journal of Materials Science*, 3:622–628, 1968.
- [99] J. G. Rider and E. Hargreaves. Yielding of oriented poly (vinyl chloride). *Journal of Polymer Science Part A-2: Polymer Physics*, 7(5):829–844, 1969.
- [100] D. Shinozaki and G. W. Groves. The plastic deformation of oriented polypropylene: tensile and compressive yield criteria. *Journal of Materials Science*, 8(1):71–78, 1973.
- [101] F. F. Rawson and J. G. Rider. A correlation of Young’s modulus with yield stress in oriented poly (vinyl chloride). *Polymer*, 15(2):107–110, 1974.
- [102] H. Tresca. Memoir on the flow of solid bodies under strong pressure. *Comptes-rendus de l’académie des sciences*, 59:754–758, 1864.
- [103] R. von Mises. Mechanics of plastic deformation of crystals. *Z. Angew. Math. Mech.*, 8(3):161–85, 1928.
- [104] E. T. J. Klompen and L. E. Govaert. Nonlinear viscoelastic behaviour of thermorheologically complex materials. *Mechanics of Time-Dependent Materials*, 3(1):49–69, 1999.
- [105] R. Hill. A theory of the yielding and plastic flow of anisotropic metals. *Proceedings of the Royal Society of London. Series A. Mathematical and Physical Sciences*, 193(1033):281–297, 1948.
- [106] R. Hill. The mathematical theory of plasticity. *Oxford*, 613:614, 1950.
- [107] B. Eidel and F. Gruttmann. Finite element analysis of anisotropic structures at large inelastic deformations. *Lecture Notes in Applied and Computational Mechanics*, 10:51–76, 2002.
- [108] T. B. van Erp, L. E. Govaert, and G. W. M. Peters. Mechanical performance of injection-molded poly (propylene): Characterization and modeling. *Macromolecular Materials and Engineering*, 298(3):348–358, 2013.
- [109] M. C. Boyce, G. G. Weber, and D. M. Parks. On the kinematics of finite strain plasticity. *Journal of the Mechanics and Physics of Solids*, 37(5):647–665, 1989.
- [110] F. F. Rawson and J. G. Rider. Effects of internal stress on the yielding of oriented poly (vinyl chloride). In *Journal of Polymer Science Part C: Polymer Symposia*, volume 33, pages 87–99. Wiley Online Library, 1971.
- [111] R. M. Caddell, R. S. Raghava, and A. G. Atkins. A yield criterion for anisotropic and pressure dependent solids such as oriented polymers. *Journal of Materials Science*, 8(11):1641–1646, 1973.
- [112] H. Eyring. Viscosity, plasticity, and diffusion as examples of absolute reaction rates. *The Journal of chemical physics*, 4(4):283–291, 1936.
- [113] T. Kershah, S. F. S. P. Looijmans, P. D. Anderson, and L. C. A. van Breemen. Thermo-mechanically coupled modelling of a single-asperity scratch on an isotropic isotactic polypropylene surface. *Tribology International*, 141:105946, 2020.
- [114] S. Krop, H. E. H. Meijer, and L. C. A. van Breemen. Global and local large-deformation response of sub-micron, soft-and hard-particle filled polycarbonate. *Journal of the Mechanics and Physics of Solids*, 87:51–64, 2016.

- 
- [115] D. J. A. Senden, J. A. W. van Dommelen, and L. E. Govaert. Strain hardening and its relation to bauschinger effects in oriented polymers. *Journal of Polymer Science Part B: Polymer Physics*, 48(13):1483–1494, 2010.



# Acknowledgments

I would like to express my gratitude to many people who I met in my PhD journey. First, I would like to thank my daily supervisor, Lambèrt, for offering me the opportunity of working with him. Thanks for the valuable meetings and discussions that guided me through the tough PhD road. I would also like to thank my promoter, Patrick, for the supportive suggestions and guidelines that helped me unravelling many obstacles. I have learned a lot from both of you.

I would like to acknowledge the Dutch Polymer Institute (DPI) for the funding of this project. Special thanks to Stan for his efforts and the collaboration we had which resulted in two publications.

I had the opportunity to meet a lot of new amazing people from all around the globe who made the PhD life such a nice experience. I would particularly like to thank the famous 4.22 colleagues in which many of them became friends, the one and only Enrico the fantastic Italian guy with who we started the famous men association “GSM” upon my arrival, the very smart Russian tavaresh Leonid, Fabio, Coen, Prakhyat, Emanuele, Harm, and finally the new addition to the office Hernan to who I wish the best in his PhD journey.

I would like to thank all the Polymer Technology Group and especially my friends, Donna Rosaria, Konstantinos (happy to work with you), Kalouda, Monica, Georgios, Wing-Hin and Jessica. Special thanks to Ans for helping with administrative tasks. I would like to thank many friends who I met at the TU/e and had great time with, Javier, Franz, Michael, Maxime, Rudie, Teresa, Sophia, Matilde, Giulia, Andre, Dina, and Ahmed.

Finally and most importantly, I would like to thank my Mother and I will always be grateful to my late Father who without I wouldn't have gone that far.

Tarek Kershah  
Eindhoven, June 2020



# Curriculum Vitae

Tarek Kershah was born on the 10th of October 1986 in Darmstadt, Germany. He studied Mechanical Engineering at Alexandria University in Egypt, where he received his bachelor's degree in July 2009. In 2010 he joined Ezz Steel, the largest steel company in Egypt and the Middle East and North Africa region, as a Mechanical Engineer. He continued his studies at McMaster University in Canada after he received a full scholarship, where he got his master's degree in Mechanical Engineering in June 2013. His Master thesis was entitled " Prediction Of Cutting Coefficients During Orthogonal Metal Cutting Process Using FEA Approach". In May 2015 he started his PhD in the Polymer Technology group at the TU/e, under supervision of dr.ir. L.C.A. van Breemen and prof.dr.ir. P.D. Anderson. In October 2019 he joined Wärtsilä Netherlands B.V. as a Mechanical Expert in the Waterjets department.





# List of publications

This thesis has resulted in the following publications:

- Tarek Kershah, Stan F.S.P. Looijmans, Patrick D. Anderson, Lambèrt C.A. van Breemen. Temperature dependent two-body abrasive wear of polycarbonate surfaces. *Wear*, 440–441, 203089 (2019)
- Tarek Kershah, Stan F.S.P. Looijmans, Patrick D. Anderson, Lambèrt C.A. van Breemen. Thermo-mechanically coupled modelling of a single-asperity scratch on an isotropic isotactic polypropylene surface. *Tribology International*, 141, 105946 (2020)
- Tarek Kershah, Patrick D. Anderson, Lambèrt C.A. van Breemen. Uniaxial and biaxial response of anisotropic polypropylene. Accepted *Macromolecular Theory and Simulations*, (2020)
- Tarek Kershah, Patrick D. Anderson, Lambèrt C.A. van Breemen. Finite element modelling of a single-asperity scratch on an anisotropic polypropylene surface. Submitted to *Tribology International*, (2020)

